Theoretical investigations of solid solutions and hydrogenation of Ti-V based compounds

(Ti-V 系化合物の固溶状態及び水素化特性の理論解析)

Noriko Otani

大谷　紀子

2017

Contents

Chapter 1

General Introduction

1.1. Hydrogen storage materials for fuel cell vehicles

Hydrogen fuel has been attracting great interest as a CO_2 emission-free energy source because of environmental problems such as global warming and exhaustion of fossil fuels [1]. In general, fuel cells produce electricity and water by electrochemically combining atmospheric oxygen with hydrogen fuel. A major application of fuel cell technologies is fuel cell vehicles (FCVs) being developed as new generation environmentally friendly vehicles [2]. 70 MPa high-pressure hydrogen tanks are mounted on recent commercial FCVs as a hydrogen source to achieve comparable mileage to gasoline automobiles [3]. There are still difficulties in producing, handling and transporting high-pressure hydrogen gas, being obstacles for developing FCVs. Storaging hydrogen within solid-state materials is regarded as one of the key alternatives to the use of high-pressure hydrogen tanks, because most hydrogen storage materials absorb hydrogen gas at lower hydrogen pressures [4].

Many researchers have investigated hydrogen storage materials for use in FCVs. Although there are a wide variety in the types of hydrogen storage materials, they are mainly classified into two categories by the mechanisms of hydrogen storage: physical and chemical storage [5,6]. Compressed hydrogen gas or carbon-based materials, such as carbon nanotubes, graphene and fullerenes, are examples of constituents of the former group. In most cases, such materials show little storage capacities, instead of fast kinetics or complete hydrogen absorption-desorption cyclic reversibility. On the other hand, in the materials belong to the latter group, chemical bonds with hydrogen atoms are formed, which result in relatively high storage capacities. Materials such as

metal hydrides [7], borohydrides, alanates, amide-imide systems, and ammonia-borane compounds are examples of the materials in latter group and have been investigated for the next generation FCVs [8]. Hydrogen storage materials for FCVs have to satisfy many requirements: at least 3 mass% hydrogen storage capacity under near-standard conditions, favorable initial kinetics, cyclic stabilities of absorption and desorption, and economical production costs. Because of these severe requirements, commercially applicable materials for FCVs have not been obtained yet.

1.2. Ti-V-based hydrogen storage alloys

Pure vanadium metal has an affinity for hydrogen and has a bcc structure, while the dihydrides, VH_2, a CaF_2-type structure. Between these end members are some intermediate phases [9], with at least two plateaus appearing in the pressure-composition-temperature (PCT) curve [10,11]. Figure 1.1 shows the structure of metal V and VH_2. V has been considered to be promising hydrogen storage materials, because its storage capacity can reach up to 4 mass% and it shows good cyclic stability [12,13]. In spite of these good properties, there are basically two obstacles in application of V to FCVs. One problem appears in extremely low equilibrium hydrogen pressures, $P_{\mathrm{H_2}}^{\mathrm{eq}}$, of dehydrogenation from monohydride to metal [10,14]. Griffiths *et al.* reported the value of the first plateau at 300 K was about 0.1 Pa. The other is the high cost of pure V which hinders the practical use of V in FCVs. Because V is alloyed with various metals, hydrogenation of V-based alloys has also been investigated. Among them, titanium-vanadium (Ti-V) based alloys have been investigated to lower the production costs owing to inclusion of cheaper Ti ingredients and to improve the storage capacities.

Ti and V form bcc solid solution alloys in a broad range of V content, which can absorb up to 4 mass% H_2 via a two-step hydrogenation process, namely (1) from bcc alloys to monohydrides

and (2) from monohydrides to CaF_2-type dihydrides [15–18]. For instance, $Ti_{1.0}V_{1.1}Mn_{0.9}$ alloy, whose structures have been investigated by experimental measurements by Nakamura *et al.*, is known to form disordered bcc solid solution [19–26]. As hydrogenation proceeds, bcc crystal lattice of metal atoms expands along the *c* axis, and changes into CaF_2-type dihydride, $Ti_{1.0}V_{1.1}Mn_{0.9}H_6$, via interstitial face-centered-tetragonal (fct) monohydride, $Ti_{1.0}V_{1.1}Mn_{0.9}H_3$. Moreover, many types of multi-element Ti-V-based alloys, such as Ti-V-Cr [27–29], Ti-V-Fe [30], and Ti-V-Cr-Al [31], have bcc structures and form hydrides.

Because properties such as $P_{H_2}^{eq}$ and hydrogenation temperature strongly depend on the compositions and additional elements [16,17,27–29,32,33], it should be possible to identify compositions with suitable ranges of $P_{H_2}^{eq}$ for practical applications. Although many experimental studies have been devoted to elucidating the relation between pressure and composition, how $P_{H_2}^{eq}$ depends on the compositions remains unclear. Theoretical evaluation of $P_{H_2}^{eq}$ of those hydrogen storage alloys is of help in understanding and controlling the behavior of $P_{H_2}^{eq}$.

In this study, we investigate properties of Ti-V-based compounds using first-principles calculations which require well-defined structural models of the compounds in question. In majority of Ti-V-based compounds, precise lattice symmetry and the atomic-level distribution of Ti and V atoms on the metal sublattices remains experimentally unclear. One of the reasons for this is that Ti and V are hard to be distinguished by X-ray diffraction spectroscopy, because, as neighboring elements of the periodic table, their diffraction patterns are very similar. Even when neutron diffraction is used, V positions are difficult to be determined because of the small coherent scattering length. Furthermore, configurations of H atoms in monohydrides have been undetermined in experiments. Recently, transmission electron microscopy (TEM) has enabled direct observation of hydrogen atoms in metal hydrides [34], but this is limited to the case of fully hydrogenated

crystalline samples. Due to significant isotope effects in V-based hydrides, measurements involving deuterium provide little information on H sites within a cell [13,35]. Figure 1.2 shows the typical occupation sites of interstitial H atoms in bcc and fcc host lattices. These sites are classified into two categories by the number of coordinating metal atoms around H atoms: tetrahedral (T) and octahedral (O) interstitial sites. We investigated $P_{\mathrm{H_2}}^{\mathrm{eq}}$ based on the structural search of possible T- and O-site configurations of hydrogen atoms using first-principles calculations. This procedure will be discussed in Chapter 3.

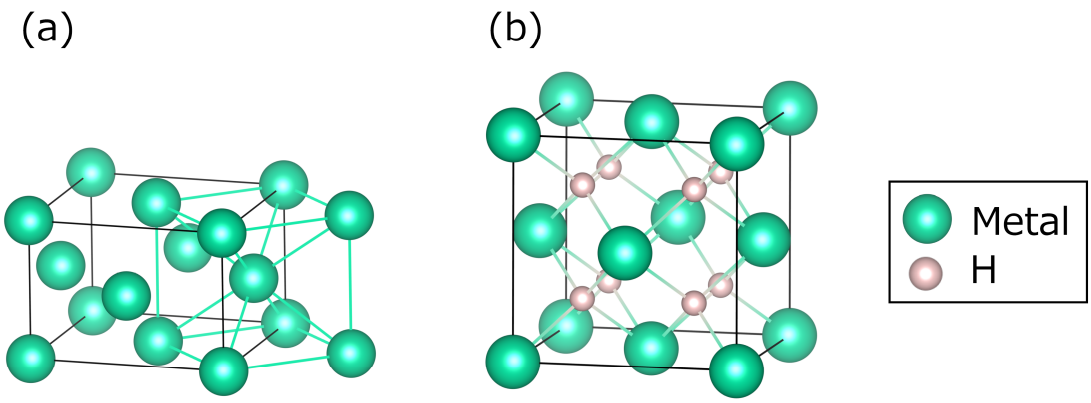

Fig. 1.1. Crystal structures and H sites of (a) bcc vanadium and (b) CaF_2-type (fluorite) VH_2.

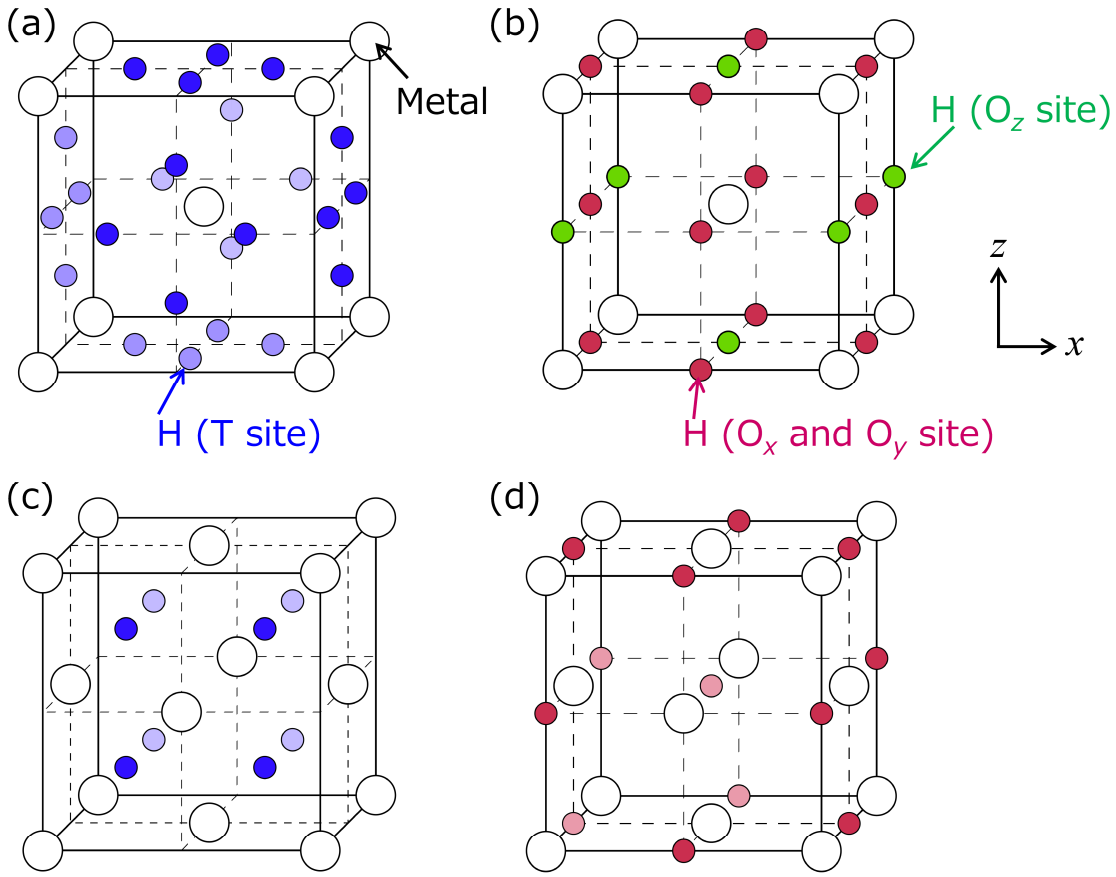

Fig. 1.2. (a) Tetrahedral (T) and (b) octahedral (O) interstitial hydrogen sites in a conventional bcc lattice of host metal atoms. O sites in (b) are classified as O_z (green filled circles), and O_x and O_y (red filled circles). (c) T and (d) O sites in a conventional fcc lattice.

1.3. Overview

This thesis contains five chapters, and the overview of each chapter is as follows.

In Chapter 2, the solution states of metal atoms in $Ti_{1-x}V_xH_2$, stability of found ordered ground-state structures, and an effect of metal configurations on the bonding strength of H atoms are investigated using a combination of the cluster expansion method and first-principles calculations. Formation energies of all possible configurations of metal atoms in CaF_2-type structures with up to sixteen metal atoms are calculated using the optimized set of clusters. Nine ground-state structures are identified with different compositions, most of which are found to have layered structures containing V bilayers. Analysis of the component clusters suggests that, while pair clusters contribute to formation of the layered structures, the higher-body clusters contribute more to stabilization of V bilayers than Ti bilayers. From calculations of short-range order parameters for all configurations of composition x = 1/2, low-energy structures including the layered structures have a phase-separation tendency on the atomic level. Order-disorder transition temperatures of the ground-state structures are estimated from Monte Carlo simulations to be less than about 460 K. The transition temperatures and comparison of lattice parameters with experimental values indicate that disordered solutions are predominantly formed under typical synthesis conditions. In addition, we examine the stability of H atoms in different coordination environments, indicating that the long-range metal-atom ordering does not greatly affect the local bonding between H and surrounding metal atoms.

In Chapter 3, $P_{H_2}^{eq}$ for hydrogenation reactions of the two plateau regions in the PCT curves of the V-H system are estimated using first-principles calculations. We assumed reaction V-$VH_{0.5}$ for the lower plateau and VH-VH_2 for the higher plateau. In the intermediate phases, H atoms can distribute over interstitial T and O sites in a bcc lattice. To determine the ground-state structures of $VH_{0.5}$ and VH necessary to estimate $P_{H_2}^{eq}$, the energetical stabilities of a large number

of configurations constructed from a bcc unit cell were calculated without including vibrational contributions. Phonon calculations were then carried out for the lowest-energy structures to quantify the vibrational contributions to the energy. Treatment of vibrational energies was simplified by establishing the linear relationship between hydrogen content and zero-point energy, which depends only on the type of sites occupied by H atoms, i.e., T or O. When vibrational energies are included, H atoms are found to occupy O sites in both compounds, whereas, when not included, H atoms are distributed over T sites. Predicted $P_{\mathrm{H_2}}^{\mathrm{eq}}$ reproduce the experimental behavior well. Our results indicate that vibrational energies, especially zero-point energies, cannot be neglected when establishing the stability of H atoms in metal lattices and estimating $P_{\mathrm{H_2}}^{\mathrm{eq}}$. The method outlined is based on an exhaustive configuration search and should be useful for the systematic investigation of a wide variety of V-based alloys.

In Chapter 4, $P_{\mathrm{H_2}}^{\mathrm{eq}}$ in the Ti-V-Mn-based alloys are estimated by employing the procedures introduced in Chapter 3. We mainly focus on $Ti_{1.0}V_{1.1}Mn_{0.9}$ hydrides, whose metal sublattice and H sites are determined from experimental measurements. Since the difference of zero-point energies between $Ti_{1.0}V_{1.1}Mn_{0.9}H_6$ and VH_2 is small, contributions of vibrational effects in the Ti-V-Mn-H system are assumed to be the same as those in the V-H system. The predicted $P_{\mathrm{H_2}}^{\mathrm{eq}}$ reproduce the tendencies observed in experiments. Moreover, we examined $P_{\mathrm{H_2}}^{\mathrm{eq}}$ in the Ga-doped Ti-V-Mn alloys in order to assess the doping effect of the non-transition metal. The considerable changes of $P_{\mathrm{H_2}}^{\mathrm{eq}}$ by Ga-doping seems to be originated from the longer bond length between Ga and H atoms than those between transition metal and hydrogen atoms.

Conclusions of this thesis are summarized in Chapter 5.

References

[1] S. Sharma, S.K. Ghoshal, Hydrogen the future transportation fuel: From production to applications, Renew. Sustain. Energy Rev. 43 (2015) 1151–1158.

[2] S. Singh, S. Jain, V. PS, A.K. Tiwari, M.R. Nouni, J.K. Pandey, S. Goel, Hydrogen: A sustainable fuel for future of the transport sector, Renew. Sustain. Energy Rev. 51 (2015) 623–633.

[3] N. de Miguel, R. Ortiz Cebolla, B. Acosta, P. Moretto, F. Harskamp, C. Bonato, Compressed hydrogen tanks for on-board application: Thermal behaviour during cycling, Int. J. Hydrogen Energy 40 (2015) 6449–6458.

[4] D. Mori, K. Hirose, Recent challenges of hydrogen storage technologies for fuel cell vehicles, Int. J. Hydrogen Energy 34 (2009) 4569–4574.

[5] A.F. Dalebrook, W. Gan, M. Grasemann, S. Moret, G. Laurenczy, Hydrogen storage: beyond conventional methods, Chem. Commun. 49 (2013) 8735–8751.

[6] A. Züttel, Materials for hydrogen storage, Mater. Today 6 (2003) 24–33.

[7] B. Sakintuna, F. Lamari-Darkrim, M. Hirscher, Metal hydride materials for solid hydrogen storage: A review, Int. J. Hydrogen Energy 32 (2007) 1121–1140.

[8] D.K. Ross, Hydrogen storage: The major technological barrier to the development of hydrogen fuel cell cars, Vacuum 80 (2006) 1084–1089.

[9] T.B. Massalski, Binary Alloy Phase Diagrams, 2nd ed., ASM International, Ohio, 1990.

[10] R. Griffiths, J.A. Pryde, A. Righini-Brand, Phase diagram and thermodynamic data for the hydrogen/vanadium system, J. Chem. Soc., Faraday Trans. 1 68 (1972) 2344–2349.

[11] J.J. Reilly, R.H. Wiswall, The higher hydrides of vanadium and niobium, Inorg. Chem. 9 (1970) 1678–1682.

[12] H. Kim, K. Sakaki, H. Ogawa, Y. Nakamura, J. Nakamura, E. Akiba, A. Machida, T. Watanuki, T. Proffen, Origin of degradation in the reversible hydrogen storage capacity of $V_{1-x}Ti_x$ alloys from the atomic pair distribution function analysis, J. Phys. Chem. C 117 (2013) 26543–26550.

[13] Y. Fukai, The Metal-Hydrogen System, Springer-Verlag, Berlin/Heidelberg, 2005.

[14] H. Yukawa, D. Yamashita, S. Ito, M. Morinaga, S. Yamaguchi, Alloying effects on the phase stability of hydrides formed in vanadium alloys, Mater. Trans. 43 (2002) 2757–2762.

[15] T. Hagi, Y. Sato, M. Yasuda, K. Tanaka, Structure and phase diagram of Ti–V–H system at room temperature, Trans. Jpn. Inst. Met. 28 (1987) 198–204.

[16] S. Ono, K. Nomura, Y. Ikeda, The reaction of hydrogen with alloys of vanadium and titanium, J. Less-Common Met. 72 (1980) 159–165.

[17] H. Kim, K. Sakaki, I. Saita, H. Enoki, K. Noguchi, A. Machida, T. Watanuki, Y. Nakamura, Reduction and unusual recovery in the reversible hydrogen storage capacity of $V_{1-x}Ti_x$ during hydrogen cycling, Int. J. Hydrogen Energy 39 (2014) 10546–10551.

[18] S. Suwarno, J.K. Solberg, J.P. Mæhlen, R.V. Denys, B. Krogh, E. Ochoa-Fernández, B.T. Børresen, E. Rytter, I.E. Gabis, V.A. Yartys, Non-isothermal kinetics and in situ SR XRD studies of hydrogen desorption from dihydrides of binary Ti–V alloys, Int. J. Hydrogen Energy 38 (2013) 14704–14714.

[19] Y. Nakamura, E. Akiba, New hydride phase with a deformed FCC structure in the Ti–V–Mn solid solution–hydrogen system, J. Alloys Compd. 311 (2000) 317–321.

[20] Y. Nakamura, K. Oikawa, T. Kamiyama, E. Akiba, Crystal structure of two hydrides formed from a Ti–V–Mn BCC solid solution alloy studied by time-of-flight neutron powder diffraction — a NaCl structure and a CaF_2 structure, J. Alloys Compd. 316 (2001) 284–289.

[21] Y. Nakamura, E. Akiba, Hydriding properties and crystal structure of NaCl-type mono-hydrides formed from Ti–V–Mn BCC solid solutions, J. Alloys Compd. 345 (2002) 175–182.

[22] Y. Nakamura, J. Nakamura, K. Sakaki, K. Asano, E. Akiba, Hydrogenation properties of Ti–V–Mn alloys with a BCC structure containing high and low oxygen concentrations, J. Alloys Compd. 509 (2011) 1841–1847.

[23] S. Yamazaki, J. Nakamura, K. Sakaki, Y. Nakamura, E. Akiba, Phase transformation and lattice-strain formation in $Ti_{1.0}V_{1.1}Mn_{0.9}$ during first absorption and desorption, Mater. Trans. 52 (2011) 586–590.

[24] S.-W. Cho, E. Akiba, Y. Nakamura, H. Enoki, Hydrogen isotope effects in $Ti_{1.0}Mn_{0.9}V_{1.1}$ and $Ti_{1.0}Cr_{1.5}V_{1.7}$ alloys, J. Alloys Compd. 297 (2000) 253–260.

[25] S.-W. Cho, H. Enoki, T. Kabutomori, C.-N. Park, E. Akiba, Isotope effect on structural transitions of $Ti_{1.0}Mn_{0.9}V_{1.1}H_X(D_X)$ and $Ti_{1.0}Cr_{1.5}V_{1.7}H_X(D_X)$ with hydrogenation, J. Alloys Compd. 319 (2001) 196–203.

[26] J. Matsuda, Y. Nakamura, E. Akiba, Microstructure of Ti–V–Mn BCC alloys before and after hydrogen absorption–desorption, J. Alloys Compd. 509 (2011) 4352–4356.

[27] J.-H. Kim, H. Lee, P.S. Lee, C.-Y. Seo, J.-Y. Lee, A study on the improvement of the cyclic durability by Cr substitution in V–Ti alloy and surface modification by the ball-milling process, J. Alloys Compd. 348 (2003) 293–300.

[28] S.-W. Cho, C.-S. Han, C.-N. Park, E. Akiba, The hydrogen storage characteristics of Ti–Cr–V alloys, J. Alloys Compd. 288 (1999) 294–298.

[29] S.-W. Cho, C.-N. Park, J.-H. Yoo, J. Choi, J.-S. Park, C.-Y. Suh, G. Shim, Hydrogen absorption–desorption characteristics of $Ti_{(0.22+X)}Cr_{(0.28+1.5X)}V_{(0.5-2.5X)}$ ($0 \leq X \leq 0.12$) alloys, J. Alloys Compd. 403 (2005) 262–266.

[30] S. Basak, K. Shashikala, P. Sengupta, S.K. Kulshreshtha, Hydrogen absorption properties of Ti–V–Fe alloys: Effect of Cr substitution, Int. J. Hydrogen Energy 32 (2007) 4973–4977.

[31] J. Hangjun, Z. Jinlong, M. Xianghai, L. Genwen, G. Jianshen, Hydrogen storage properties and structure of $TiV_{0.8-x}Cr_{1.2}Al_x$ alloys, Rare Met. Mater. Eng. 37 (2008) 803–807.

[32] E. Akiba, H. Iba, Hydrogen absorption by Laves phase related BCC solid solution, Intermetallics 6 (1998) 461–470.

[33] H. Iba, E. Akiba, Hydrogen absorption and modulated structure in Ti–V–Mn alloys, J. Alloys Compd. 253–254 (1997) 21–24.

[34] S.D. Findlay, T. Saito, N. Shibata, Y. Sato, J. Matsuda, K. Asano, E. Akiba, T. Hirayama, Y. Ikuhara, Direct imaging of hydrogen within a crystalline environment, Appl. Phys. Express 3 (2010) 116603.

[35] G. Sicking, Isotope effects in metal-hydrogen systems, J. Less-Common Met. 101 (1984) 169–190.

Chapter 2

Theoretical Investigation of Solid Solution States of $Ti_{1-x}V_xH_2$ with the Cluster Expansion Method

2.1. Introduction

Titanium-vanadium (Ti-V) based alloys, which are promising hydrogen storage materials, can absorb at most 4 mass% H_2 via a two-step hydrogenation process, namely (1) from alloys to monohydrides and (2) from monohydrides to dihydrides [1–5]. One obstacle to practical application of Ti-V based compounds is the phenomenon known as "dead storage", where a part of the stored hydrogen cannot be released from the hydride. This happens even after a few hydrogen absorption-desorption cycles, resulting in lower storage capacities than the theoretical value [6,7]. Based on investigations of V-4Cr-4Ti alloys, Ohnuki *et al.* suggested that hydrogen can be trapped by lattice defects, dislocations, vacancies, and voids [8]. Characterization of atomic-scale structures such as extended defects, ordering of metal-atom configurations, and hydrogen sites in host materials, particularly after degradation, is thus an important step in understanding the mechanisms resulting in dead storage. Recently, transmission electron microscopy (TEM) has enabled direct observation of hydrogen atoms in metal hydrides [9], but this is limited to the case of fully hydrogenated crystalline samples. Because of the difficulty in determining H distributions of nanometer scale, little is known about the hydrogenated states of even simple Ti-V binary compounds.

In the Ti-V-H system, $Ti_{1-x}V_xH_y$, metal atoms form a bcc structure in the case of the non-hydrogenated alloy ($y = 0$), while dihydrides ($y = 2$) have a CaF_2-type (fluorite) structure in

which metal atoms and hydrogen atoms occupy fcc sites and interstitial tetrahedral sites, respectively [2,10]. During hydrogenation, the bcc unit cell of the alloy anisotropically expands along the *c* axis with increasing hydrogen content. Although monohydrides $Ti_{1-x}V_xH$ has been observed to form during hydrogen absorption possibly with a bct metal sublattice, the distribution of metal atoms and specific sites occupied by hydrogen have not been adequately determined [2,11,12].

The distribution of Ti and V atoms on the metal sublattices of other compositions are also not known on the atomic level, though it is possible that they affect trapping of hydrogen atoms. One of the reasons for this is that Ti and V are hard to distinguish by X-ray diffraction spectroscopy because, as neighboring elements of the periodic table, their diffraction patterns are very similar. Even when neutron diffraction is used, V positions are difficult to determine because of the small coherent scattering length. The previously obtained phase diagram of Ti-V binary alloys ($y = 0$) shows the existence of a bcc solid solution above 900 K and dissociation behavior to a Ti-rich hcp phase and V-rich bcc phase at lower temperatures [10]. Some X-ray diffraction and nuclear magnetic resonance (NMR) experiments have revealed nano-scale precipitation of a Ti-rich phase of Ti-V alloys and hydrides in various composition [13–18]. Combining theoretical cluster model analyses with measurements of diffusion constants, neutron diffraction, and NMR suggest local clustering of Ti and V occurs in Ti-V alloys and hydrides [12,19–22].

In order to examine the solution states of alloys and other crystalline systems theoretically, density functional theory (DFT) calculations combined with the cluster expansion (CE) method [23,24] have been widely used. This methodology provides a way to estimate energies for an enormous number of configurations with the accuracy similar to DFT by performing only a relatively small number of DFT calculations within error of few meV in an optimal case, and thereby to identify new ordered structures and calculate phase diagrams [25–29]. The solution states

of Ti-V binary alloys were studied by Chinnappan *et al.* [30] using the CE method to verify the experimental phase diagram. They showed no preference for the formation of ordered structures but the complete phase separation into hcp-Ti and bcc-V phases, consistent with experiments [10]. For the Ti-H system, Xu *et al.* [31] investigated the phase stabilities of TiH_y for $0 \leq y \leq 2$ using the CE method for various H-vacancy configurations. To the best of our knowledge, there are no previous CE works on the solution states in the V-H system or hydrated Ti-V. A systematic study of the Ti-V-H system, which should provide useful information for understanding the hydrogenation properties, requires an identification of configurations of metal and H atoms.

In this study, we investigate solid solution states of Ti-V binary dihydrides, $Ti_{1-x}V_xH_2$, using first-principles calculations together with the CE method, which are ideal models of fully hydrogenated state ($y = 2$) possibly different from experimental situation where y is slightly less than 2 [5,32,33]. The slight reduction of H atoms is considered to have negligible effects on the configuration of metal atoms when $y \sim 2$. Compounds of all compositions, including the end members, are assumed to form CaF_2-type structures with H atoms on tetrahedral sites, so that it is possible for ordered structures to form for each composition. Our results indicate that the ground states of these dihydrides have layer-type ordered structures over the entire composition range. We investigate various characteristics of these ordered structures, such as their lattice constants, short-range order, and order-disorder transitions. Since the configuration of the metal atoms may affect hydrogenation and dehydrogenation behavior, we also examine the effects of ordering on bonding strength of H atoms within the dihydrides.

2.2. Computational methodology

2.2.1. Cluster expansion (CE) method

In order to search ground-state structures of $Ti_{1-x}V_xH_2$, formation energies of possible configurations of Ti and V atoms on an fcc sublattice need to be calculated. The number of possible configurations in an arbitrary cell depends on the number of atoms within the cell. The total number of independent configurations of binary alloys increases rapidly as the number of atomic sites increases. For example, a total of 154,156 configurations are possible in our case for numbers of sites from two to sixteen. DFT calculations of such an enormous number of configurations are currently impractical.

The CE method is used to calculate the energy, *E*, in a configuration space based on summation of interactions according to the following polynomial representation [23,24]:

$$E = V_0 + \sum_i V_i \sigma_i + \sum_{i,j} V_{ij} \sigma_i \sigma_j + \sum_{i,j,k} V_{ijk} \sigma_i \sigma_j \sigma_k + \cdots , \quad (1)$$

where σ_i is an Ising-like configurational variable for a particular lattice site *i*, taking a value of +1 or -1 depending on the atom species, in this case, Ti or V. Polynomial coefficients such as V_{ijk} represent interaction energies between a given number of particles. Each term on the right hand side of Eq. (1) forms a figure composed of a combination of *n* interacting atoms on lattice points (vertices), called an *n*-body cluster (where $n = 0, 1, 2, \ldots$). For example, pair clusters ($n = 2$) are composed of atom pairs with arbitrary interatomic distances. Assigning each cluster type a cluster index α, Eq. (1) can be rewritten as

$$E = \sum_\alpha V_\alpha \cdot \varphi_\alpha, \quad (2)$$

where V_α is called the effective cluster interaction (ECI) and φ_α is the correlation function of cluster type α. ECIs of symmetrically equivalent clusters are the same for a given solid solution

composition. If the number of symmetrically equivalent clusters of cluster type α is N_α, the correlation function becomes

$$\varphi_\alpha = \frac{1}{N_\alpha} \sum_{i,j,\cdots \in \alpha} \sigma_i \sigma_j \cdots. \quad (3)$$

By optimizing a set of clusters and ECI values to represent a series of trial DFT energy data in a given configuration space, one can obtain energies for an enormous number of possible configurations using Eq. (2) with an accuracy close to that of DFT calculations when suitably optimized EICs are used.

The CLUPAN code [34] was used to search for all possible configurations of metal atoms in CaF_2-type $Ti_{1-x}V_xH_2$ structure models of a given periodic cell size. The primitive cell of the CaF_2-type structure contains one metal atom and two H atoms, and this was used as the basic cell from which derivative (supercell) structures were constructed. We selected 64 clusters with up to five-body interactions (6 pairs, 23 three-body, 16 four-body, and 17 five-body clusters) as candidate components. The ground-state structures were searched for from 154,156 structures, each of which contained between two and sixteen metal atoms in the unit cell. ECIs were determined by a least-squares fitting using Eq. (2) to the energies of sample structures obtained from DFT. The suite of clusters used to represent the total energies was optimized using a genetic algorithm (GA) [35,36] and the leave-one-out cross-validation (CV) score [26,37,38]. Ground-state structures were identified from the convex hull of formation energies calculated from CE energies plotted as a function of composition.

In general, ECIs depend on the number of sample structures used in the DFT calculations (N_{DFT}) and the total number of clusters (N_{clusters}) used to describe them. The CE error can be reduced by carefully selecting structures for trial DFT calculations. In this study, ECIs were determined using the following two steps, (i) initial optimization, and (ii) optimization combined with

ground-state searching. In step (i), ECIs were optimized using DFT-calculated energies of sample configurations selected from all possible configurations with relatively small unit cells. We selected structures from 2,279 non-equivalent configurations containing up to ten metal atoms in conjunction with the cluster analysis of structure populations (CASP) method [39]. According to this method, configuration space is divided into smaller spaces by using characteristics of pair correlation functions. The CASP method is of use in selection of structures for DFT calculations efficiently and properly. An example of the investigation of MgO/ZnO applying the CASP method was introduced in the article [27], and detailed information of the CASP method on the current system is described in the Appendix A. The dependencies of CV scores on N_{DFT} and N_{clusters} were calculated, and the optimized ECIs were obtained as ones with converged CV scores. We called these ECIs as "initial ECIs", because they were used as the starting point of the following procedure. In step (ii), CE energies of an extended set of 154,156 configurations were calculated using the initial ECIs, and ground-state structures were identified. To improve the accuracy of ECIs further, when new ground-state structures were identified, they were added to the DFT structure sets, and then the cluster sets and ECIs updated. This step was repeated until the predicted ground-state energies converged.

2.2.2. Computational details of DFT calculations

Electronic energy calculations were performed in the framework of DFT using the projector augmented-wave (PAW) method [40,41] and the generalized gradient approximation (GGA) [42,43] as implemented in the VASP code [44,45]. A cut-off energy for the plane-wave basis set was 400 eV for all calculations. Brillouin-zone integration was carried out based on the Monkhorst-Pack scheme [46] and *k*-point spacing was set at less than 0.15 Å^{-1}. In addition to atomic

positions, both cell shape and volume were fully relaxed until the residual forces became less than 0.02 eVÅ^{-1}.

Formation energies of Ti-V dihydrides were calculated using the formula

$$\Delta E_f(x) = E(\mathrm{Ti}_{1-x}\mathrm{V}_x\mathrm{H}_2) - (1-x)E(\mathrm{TiH}_2) - xE(\mathrm{VH}_2), \quad (4)$$

where $E(\mathrm{TiH}_2)$, $E(\mathrm{VH}_2)$, and $E(\mathrm{Ti}_{1-x}\mathrm{V}_x\mathrm{H}_2)$ are the calculated total energies of TiH_2, VH_2, and Ti-V binary dihydrides, respectively. Contributions from phonon vibrations were not taken into account. The calculated heat of formation of TiH_2 (x = 0) of -1.466 eV/f.u. is confirmed to be comparable to experimental one of -1.279 eV/f.u. [47], and close to the previously reported value [48].

2.3. Results and discussion

2.3.1. Initial optimization of ECIs

In order to determine initial ECIs in step (i), we checked the convergence of CV scores as a function of N_{DFT} and $N_{clusters}$, the results are shown in Fig. 2.1. The dependence of the scores on N_{DFT} for the case of $N_{clusters}$ = 25 in Fig. 2.1(a) shows that the CV score converges within about 1.8 meV/f.u. for $N_{DFT} \geq 150$. In addition to this analysis, we checked the convergence of CV scores for each group of the divided spaces (CV-CASPs) according to the methodology described in the Appendix A. Based on the CASP method, 2,279 independent configurations was divided into ten groups, and initial ECIs are determined in the region $N_{DFT} \geq 280$ from the convergence of values of CV-CASPs. Figure 2.1(b) shows the dependence on $N_{clusters}$ for the case of N_{DFT} = 280. Here, the CV score decreases with increasing $N_{clusters}$, and converges for $N_{clusters} \geq 25$. Based on this analysis, we used 280 configurations for DFT calculations and 25 clusters to determine the initial ECIs for configuration spaces spanning relatively small cells.

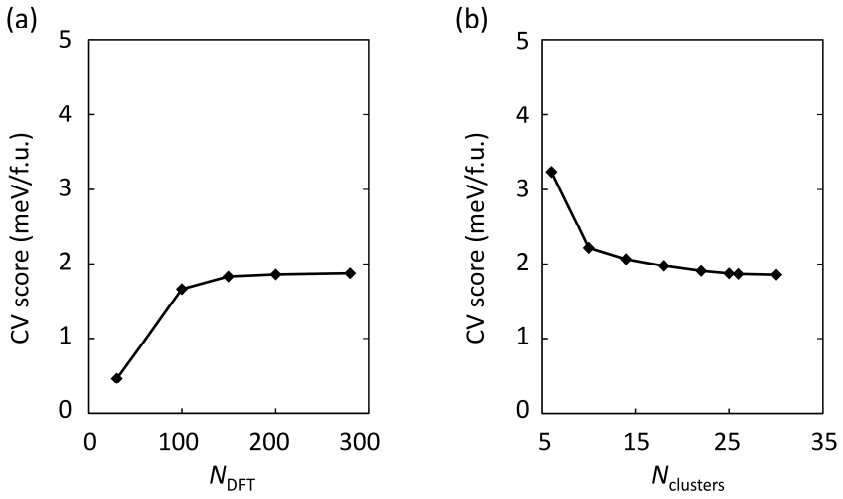

Fig. 2.1. Cross-validation (CV) scores as a function of (a) the number of DFT structures, N_{DFT}, when the number of clusters, $N_{clusters}$, is 25, and (b) $N_{clusters}$ when N_{DFT} = 280.

2.3.2. Ground-state searching

The configuration space was expanded from 2,279 configurations in the previous step to include 154,156 configurations with up to 16 metal atoms. Starting from the initial ECIs obtained using N_{DFT} = 280 and $N_{clusters}$ = 25 in the previous step, the sets of used clusters and configurations were optimized again until the predicted ground states converged. As a result, the optimized ECIs were constructed using N_{DFT} = 354 and $N_{clusters}$ = 46 (null, point, 6 pairs, 11 three-body, 14 four-body, and 13 five-body clusters). The obtained formation energies are plotted in Fig. 2.2(a).

Nine stable ground states were identified for compositions x = 1/16, 1/8, 2/7, 1/3, 2/5, 6/13, 1/2, 2/3, and 7/9 in the $Ti_{1-x}V_xH_2$ system. Unit cells of the 9 ground states are shown in Fig. 2.2(b) as supercells of the CaF_2-type conventional cell, which are transformed from the original supercells of the CaF_2-type primitive cell. They exhibit characteristic layered structures in which each layer is composed of a single component, i.e., Ti or V, only. In Fig. 2.2(b), the stacking direction is parallel to the c axis. These structures are labeled GS1, GS2,…, GS9 in ascending order of x. Details of the ground-state structures are listed in Table 2.I, where "Supercell size" indicates the number of CaF_2-type conventional unit cells, and "Stacking sequence" indicates the stacking pattern of Ti and V layers along the c axis. For example, Ti15-V1 means the repeating unit is composed of 15 Ti layers and one V layer. In addition, the supercell of GS3 is described as [Ti5-V2] × 2, meaning it contains a double stack of 5 Ti layers and a V bilayer.

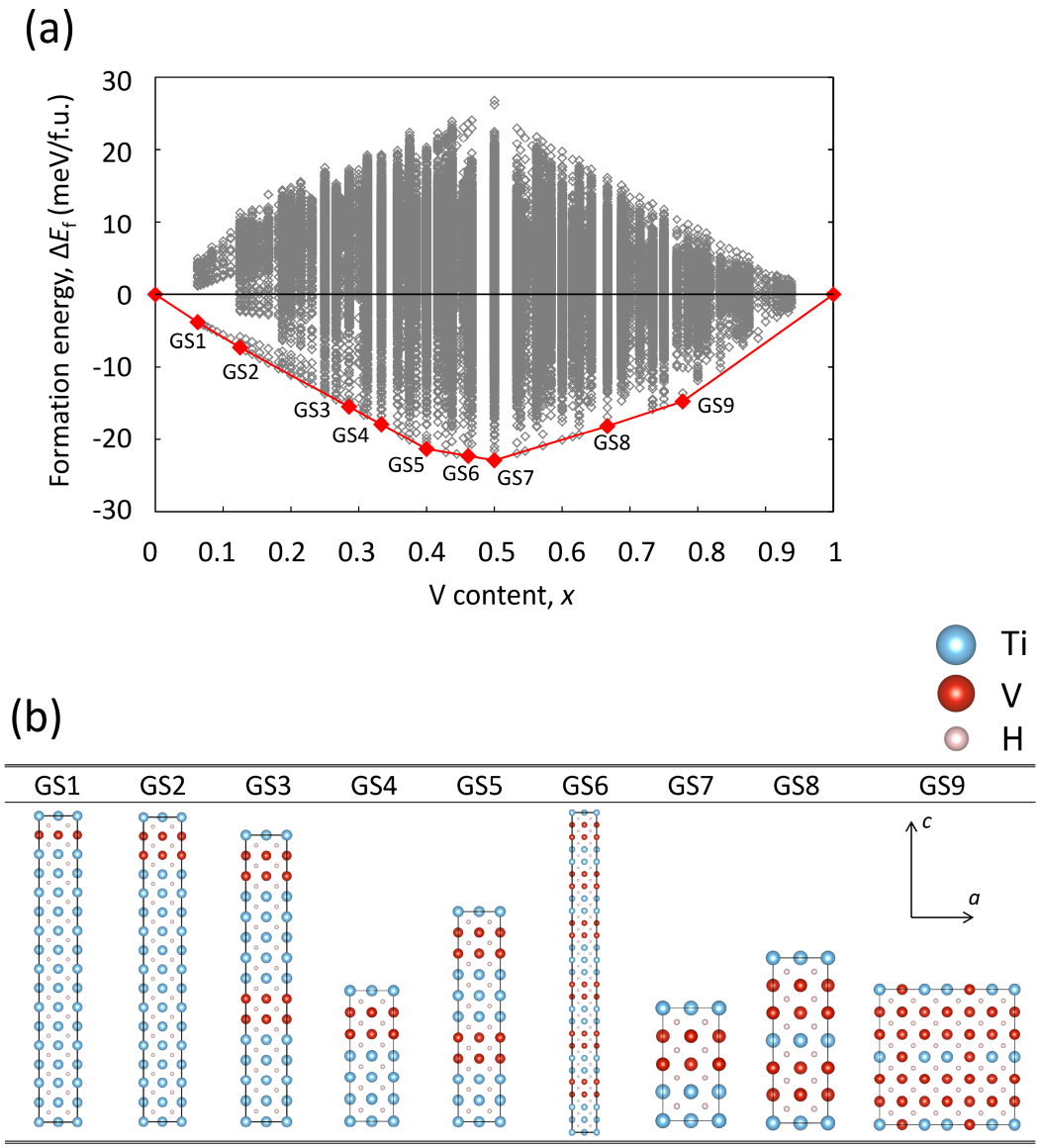

Fig. 2.2. (a) Formation energies of all symmetrically independent structures of $Ti_{1-x}V_xH_2$, calculated using the cluster expansion method, and (b) crystal structures of the ground states. Red filled rhombuses in (a) show the nine ground state structures labeled GS1-GS9, and the two end members, TiH_2 ($x = 0$) and VH_2 ($x = 1$).

Table 2.I. Structural parameters of the predicted 9 ground states (GSs). "Supercell size" indicates the size of the GS cell in terms of CaF_2-type conventional cells. Most GSs except for GS9 consist of Ti and V layers, where coordinates of V atoms are indicated by labels M1 = (0, 0, $2s/2S_z$), M2 = (1/2, 1/2, $2s/2S_z$), M3 = (0, 1/2, $(2s+1)/2S_z$) and M4 = (1/2, 0, $(2s+1)/2S_z$) for integer s. For GS9, coordinates of Ti atoms in the conventional cell are given explicitly because Ti-V-mixed layers exist between V bilayers.

Compound	x	Supercell size $S_x \times S_y \times S_z$	Positions of V atoms	Stacking sequence
GS1	1/16	1 × 1 × 8	M3, M4 with s = 7	Ti15-V1
GS2	1/8	1 × 1 × 8	M1, M2, M3, M4 with s = 7	Ti14-V2
GS3	2/7	1 × 1 × 7	M1, M2 with s = 3, 6 M3, M4 with s = 2, 6	[Ti5-V2]×2
GS4	1/3	1 × 1 × 3	M1, M2, M3, M4 with s = 2	Ti4-V2
GS5	2/5	1 × 1 × 5	M1, M2 with s = 2, 4 M3, M4 with s = 1, 4	[Ti3-V2]×2
GS6	6/13	1 × 1 × 13	M1, M2 with s = 2, 4, 6, 8, 10, 12 M3, M4 with s = 1, 3, 5, 8, 10, 12	[Ti3-V2-Ti2-V2-Ti2-V2]×2
GS7	1/2	1 × 1 × 2	M1, M2, M3, M4 with s = 1	Ti2-V2
GS8	2/3	1 × 1 × 3	M1, M2 with s = 1, 2 M3, M4 with s = 0, 2	[Ti1-V2]×2
GS9	7/9	3 × 1 × 3	Ti: (0, 0, 0), (0, 1/2, 1/2), (1/3, 0, 0), (1/3, 1/2, 1/2), (1/2, 1/2, 0), (1/2, 0, 1/2), (5/6, 1/2, 0), (5/6, 0, 1/2),	[Ti1'-V2]×2

All ground-state structures, except for GS1, contain bilayers of V. For example, the dihydride with $x = 1/2$, $Ti_{0.5}V_{0.5}H_2$, is most stable when it has a structure consisting of alternate Ti bilayers and V bilayers. This is known as a Z2-type structure. We also checked the lowest energy structures for all compositions considered, and found that most of these structures form similar layered structures including V-bilayers. The GS1 structure ($x = 1/16$) contains only a V monolayer due to the constraint imposed by the number of V atoms. Because the upper limit of the number of metal atoms is 16 in the present CE analysis, it is impossible for the 16-metal-atom cell with $x = 1/16$ to contain a V bilayer. In order to examine the preference for V bilayers, we calculated the DFT energy of the same composition using a 32-metal-atom cell composed of 30 Ti layers and a V bilayer. Difference between the energies of the 32- and 16-metal-atom cell was found to be less than 1 meV/f.u., indicating that monolayers and bilayers are essentially equally stable for this composition. For the purpose of better understanding of those long-range ordered structures, it would be interesting to apply reciprocal-space CE methods suitable for the analysis of long-range ordering. On the other hand, in the V-rich region of the composition space, while the GS8 structure with $x = 2/3$ also contains V bilayers, the GS9 structure has mixed Ti-V layers sandwiched by V bilayers, as shown in Fig. 2.2(a). These results indicate a preference for $Ti_{1-x}V_xH_2$ to form structures containing V bilayers over a wide range of composition, especially for Ti-rich compositions.

2.3.3. Analysis of ECIs

The characteristic layered structures evident in most of the 9 predicted ground-state structures are considered to reflect the used ECI sets derived from DFT computations with $N_{DFT} = 354$ and $N_{clusters} = 46$. Here, the maximum number of vertices in a cluster was five. Their cluster indices can be described using the notation $\alpha = (m, n)$, where n specifies the cluster among

clusters with the number of vertices, *m*; these are normally located in an order of increasing "size" or decreasing "compactness", which is the method used here. For example, (2,3) means a pair cluster with atoms on third-nearest neighbor sites. The smaller *n* is, the closer the pair atoms are to each other in the cluster. In the case of the cluster with no vertex (*m* = 0) or single vertex (*m* = 1), *n* is 1 for binary alloys. For clusters with $m \geq 3$, the correspondence between index *n* and cluster configuration are less clear, and *n* essentially serves as a label only.

Based on the CE energy expression in Eq. (2), clusters with relatively large absolute ECIs are expected to play a greater role in the stabilization of the ground-state structures. Among the 46 clusters used in descending order, the top 10 clusters in absolute ECI values are (0,1), (1,1), (2,3), (2,1), (3,4), (2,2), (2,5), (5,13), (4,3) and (2,4). The (0,1) and (1,1) clusters play a trivial role in stabilizing a specific metal atom configuration for a fixed composition because the ECI of (0,1) is the energy of a completely random distribution when $x = 1/2$, and the ECI of (1,1) depends only on the composition. For simplicity, we ignore these two terms in the rest of the discussion. The configurations and values of optimal ECIs of the selected clusters are shown in Fig. 2.3. In order to explore the relationship between those clusters with higher absolute ECI values and formation of layered structures with relatively low energies, we performed CE analyses using only the small number of clusters as follows.

(m, n)	(2,3)	(2,1)	(3,4)	(2,2)
$N_{(m, n)}$	24	12	48	6
ECI (meV/f.u.)	23.9	-15.6	-12.1	-10.9
	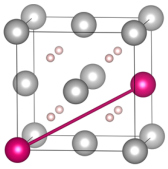	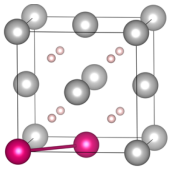	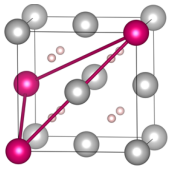	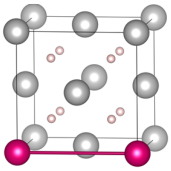
(m, n)	(2,5)	(5,13)	(4,3)	(2,4)
$N_{(m, n)}$	24	48	48	12
ECI (meV/f.u.)	-8.7	8.3	-8.2	8.1
	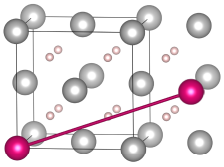	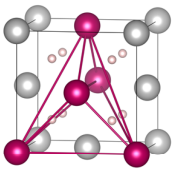	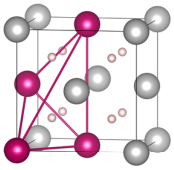	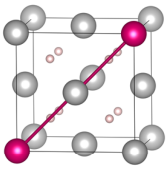

Fig. 2.3. Configurations of eight clusters with up to five-body interactions in descending order of their absolute values of effective cluster interactions (ECIs). "(m, n)" indicates the m-body n-th cluster, and "$N_{(m, n)}$" means the number of symmetrically equivalent (m, n) clusters in the system. Optimal ECI values are indicated by the rows of "ECI".

Figure 2.4(a) shows the formation energies of Ti1-V1, Ti2-V2 (GS7) and Ti4-V4 layered structures of $Ti_{0.5}V_{0.5}H_2$ calculated using the clusters shown on the horizontal axis. For example, the label +(2,3) means that the CE energies are calculated using (0,1), (1,1) and (2,3) clusters. In the figure, it is seen that the Ti2-V2 bilayer structures become stable compared to other Ti1-V1 and Ti4-V4 structures and have energies close to the DFT values when both (2,3) and (2,1) clusters are included. This demonstrates that pair clusters such as (2,3) and (2,1) enhance bilayer formation because of the following two effects: (1) the (2,1) cluster with its negative ECI value induces segregation of each metal species because the total energy decreases when the metal atoms of the same element occupy nearest-neighbor sites. This segregation leads to formation of layered structures; (2) the (2,3) cluster with its positive ECI value causes a decrease in energy when atoms of different elements occupy third-nearest-neighbor sites (as seen in Fig. 2.3), leading to a preference for bilayer formation.

Although the preference of bilayer formation can be explained by the pair interactions as shown above, those interactions are insufficient to describe the asymmetric feature about $x = 1/2$ in Fig. 2.2(a). For example, GS4 with $x = 1/3$ does not have symmetrical stacking structure with GS8, as shown in Fig. 2.2(b). This is because the correlation function of a pair cluster, given by

$$\varphi_{\mathrm{pair}} = \frac{1}{N_{\mathrm{pair}}} \sum_{i,j} \sigma_i \sigma_j \,, \tag{5}$$

is symmetrical, i.e., the same whether $\sigma_i = 1$ (Ti) and $\sigma_j = -1$ (V) or $\sigma_i = -1$ (V) and $\sigma_j = 1$ (Ti), so that a convex hull is fully symmetric about $x = 1/2$. The symmetric dependence on chemical composition is broken when odd-number-body clusters are added to ECI sets.

To elucidate the contribution of the three-body (3,4) cluster to the ground-state structures, formation energies of Ti4-V2 and [Ti2-V1] × 2 structures with Ti-rich composition $x = 1/3$ are plotted in Fig. 2.4(b). The former is ground-state GS4 of the full ECI set and the latter is the

structure made by alternation of Ti and V in GS8 (x = 2/3). The result shows the tendency of the GS4 structure to become stable compared to the [Ti2-V1] × 2 structure when the (3,4) cluster is included, as similar to the results obtained from full CE analyses using 46 clusters. This demonstrates the effects of higher-body clusters than three on the preference for V bilayer formation, resulting in asymmetric shape of the convex hull.

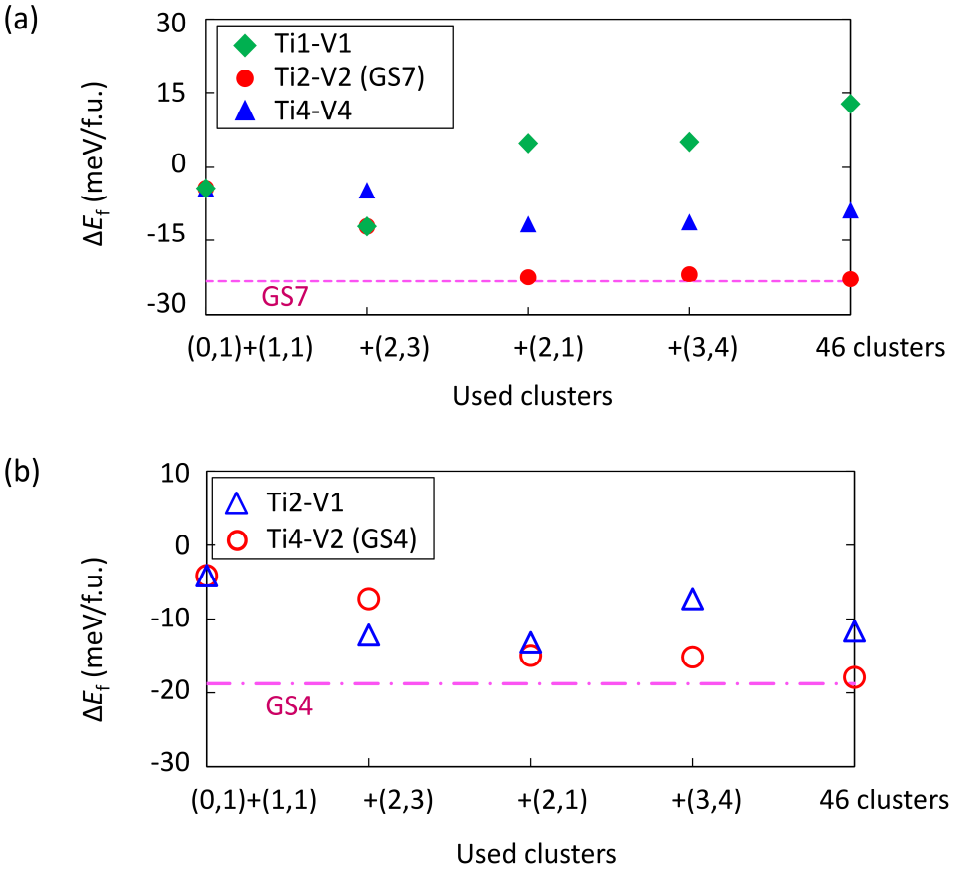

Fig. 2.4. Formation energies for layered structure models when (a) x = 1/2 and (b) x = 1/3, for different cluster sets. Red dotted line indicates the DFT energies of the ground-state structure, i.e., GS7 for x = 1/2 and GS4 for x = 1/3, respectively.

2.3.4. Short-range order

The short-range order (SRO) parameter, σ_{SRO}, is an index representing local ordering of metal atoms, and we use it here to probe atomic-level clustering in the $Ti_{1-x}V_xH_y$ system. For an alloy $A_{1-x}B_x$, σ_{SRO} is defined in terms of pair probabilities $P_{\mathrm{A}} = 1 - x$ and $P_{\mathrm{B}} = x$ [19]:

$$P_{\mathrm{AA}} = P_{\mathrm{A}} + (1 - P_{\mathrm{A}})\sigma_{\mathrm{SRO}}\,, \tag{6}$$

$$P_{\mathrm{AB}} = P_{\mathrm{B}} - P_{\mathrm{B}}\sigma_{\mathrm{SRO}}\,, \tag{7}$$

where P_{AA} is the probability of finding an A atom on a nearest-neighbor lattice site with respect to a site occupied by an A atom. These probabilities satisfy

$$P_{\mathrm{AA}} + P_{\mathrm{AB}} = 1\,. \tag{8}$$

Structures tend to phase separate when this parameter is positive, while A-B nearest-neighbor pairs are preferred in structures with negative values. When the structure is disordered, σ_{SRO} is zero. Brouwer *et al.* suggested from measurements of the diffusion constant of dilute Ti-V bcc hydrides ($y \sim 0$) that σ_{SRO} is positive and in the range of 0.36 to 0.51 [19]. Ueda *et al.* extended this to the study of Ti-V monohydrides ($y = 1$), and found that $\sigma_{\mathrm{SRO}} = 0.43 \pm 0.05$, indicating the tendency of metal atoms to phase separate [12].

In this study, we compared the SRO parameters of all possible configurations for $x = 1/2$, i.e., a total of 14,756 independent structures containing up to sixteen metal atoms in the unit cell. Figure 2.5 shows the relation between formation energy and σ_{SRO}. In this figure, we see that structures with energies less than -10 meV are distributed over the region of $\sigma_{\mathrm{SRO}} > 0$. On the other hand, structures with $\sigma_{\mathrm{SRO}} < 0$ tend to have higher energy. The most stable structure obtained from the ground-state search (GS7) has $\sigma_{\mathrm{SRO}} = 1/3$. These results suggest that phase separated structures on the atomic level, including layered structures, is energetically more favorable than mixed structures for Ti-V dihydrides.

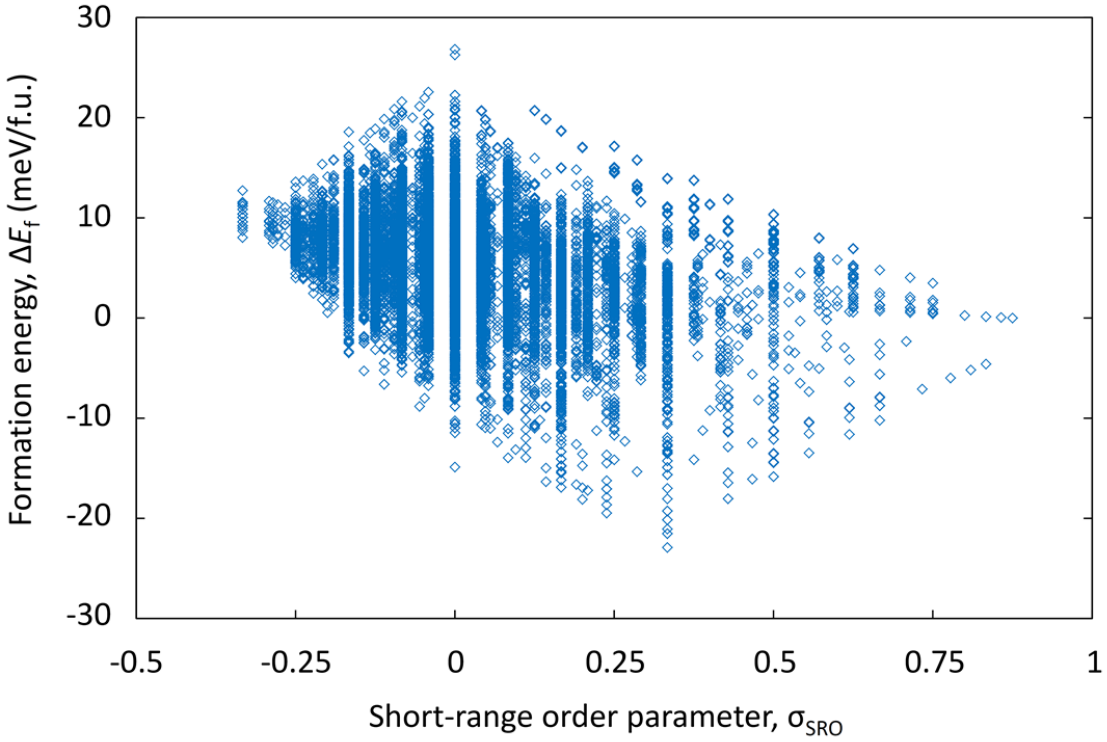

Fig. 2.5. Formation energies of all structures with $x = 1/2$ as a function of short-range order parameter, σ_{SRO}.

2.3.5. Order-disorder transitions

In order to estimate the order-disorder transition temperature, T_c, of the ordered ground-state structures identified by CE analysis, canonical Monte Carlo (MC) simulations were performed for the most stable structure of x = 1/2, i.e., GS7. A 16 × 16 × 16 supercell of the CaF_2-type primitive cell was used, and 2000 MC steps per metal atom were performed at temperatures between100 and 1000 K to calculate the thermodynamic average after first performing 2000 equilibration steps per metal atom. Figure 2.6 shows the temperature dependences of pair correlation functions of structures obtained by averaging in MC steps, which are calculated using Eq. (5) for the first to the sixth-nearest-pair clusters. The correlation functions in the low temperature region less than 300 K correspond to values of the ordered Ti2-V2 structure. The absolute values of correlation functions decrease with increasing temperature and its slopes change abruptly at around 460 K. They asymptotically approach zero in the higher temperature range. These behavior indicate the transition from the ordered to disordered phase and $T_c \sim 460$ K. Since the formation energies of the ground-state structures of other compositions are higher than that of GS7 (x = 1/2), their T_c should be lower than that of GS7, i.e., about 460 K. This indicates the tendency of $Ti_{1-x}V_xH_2$ to form random solution in contrast to phase separation behavior observed in the dehydrated case [30], suggesting that the fully hydrated states have a slight responsibility to macroscopic precipitation of Ti-V hydrides.

Alloying temperatures of Ti-V compounds using typical methods such as arc-melting are higher than 1300 K. Since the temperatures are significantly higher than the calculated order-disorder transition temperatures, samples quenched from those elevated temperatures are unlikely to form ordered structures. It is, however, possible that the predicted ground states will appear if samples are cooled slowly or annealed at a temperature below T_c for a sufficiently long time. Ordered structures may also form in the microscopic regions during hydrogen

absorption-desorption. The latter could be identified experimentally by direct observation on the atomic level using TEM or characterization of the short-range order parameter as described above.

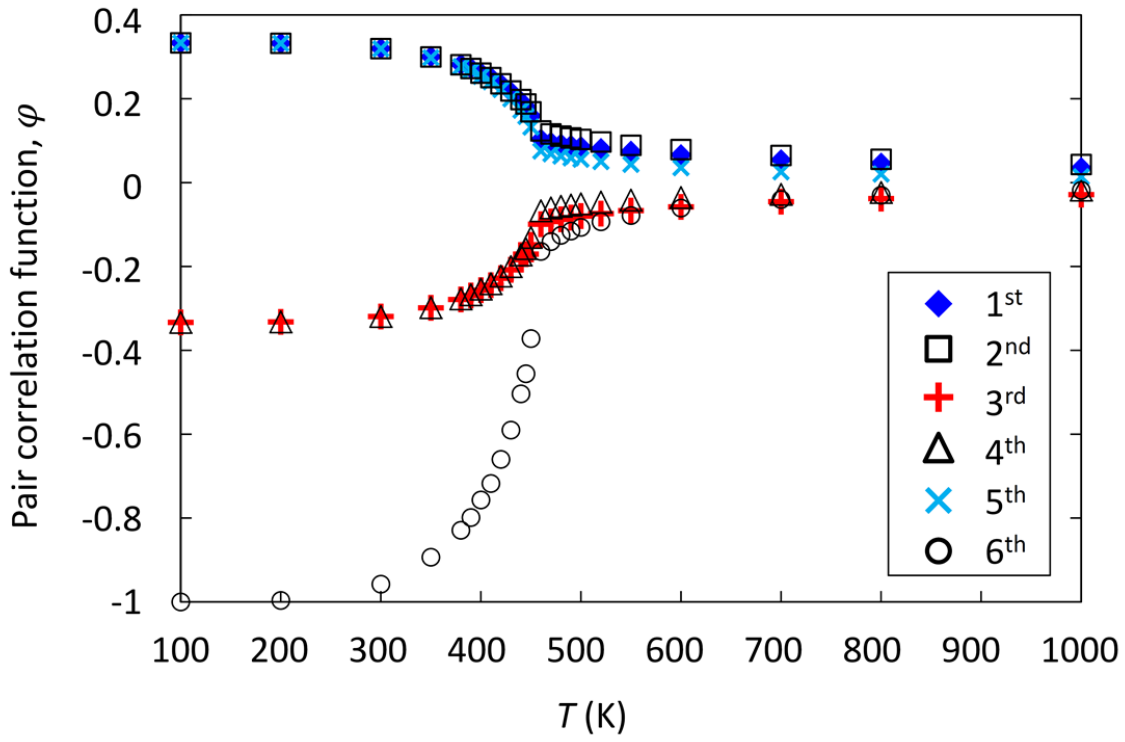

Fig. 2.6. Pair correlation functions of $Ti_{0.5}V_{0.5}H_2$ as a function of temperature, obtained by canonical Monte Carlo simulations for the first to sixth nearest pairs.

2.3.6. Comparison of lattice constants

Calculated lattice constants of ground-state structures expressed in terms of the CaF_2-type (pseudo-fluorite) conventional unit cell by dividing the *c* parameter by the number of stacking layers, S_z, in Table 2.I, are compared with experimental values [2–4,17,49,50] in Fig. 2.7. The lattice constants of disordered structures were examined by application of the CE method, where a cell volume was expanded in terms of correlation functions as in Eq. (2). We firstly obtained ECIs of volumes from the same set of structures and clusters as that used in the formation energy calculations in Fig. 2.2, and then the volumes of disordered structures were calculated using the ECIs and correlation functions of a disordered binary alloy, $(1-2x)^m$. The calculated lattice constants of disordered structures, obtained from the cubic root of the volume, are shown by the black line in Fig. 2.7, and decrease linearly as V content increases in accordance with Vegard's law. In contrast, the ground-state structures of Ti-rich compositions exhibit strong tetragonality: the *a* and *c* lattice constants are larger than and smaller than those of disordered models which are consistent with values reported from experiments. Experimental studies reported non-tetragonal structures and a similar linear decrease in lattice constants with increasing V content (denoted by the dashed line in Fig. 2.7) to the calculations of disordered models. It thus appears likely that disordered structures are formed rather than the ground-state structures when using conventional synthesis techniques.

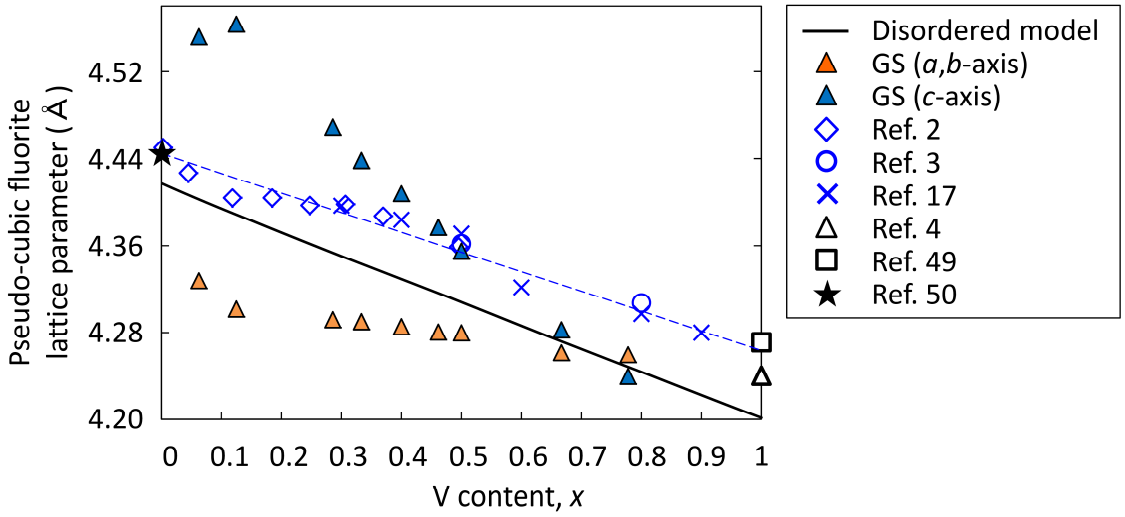

Fig. 2.7. Average pseudo-cubic lattice parameters obtained from DFT calculations of ordered ground-state and the cluster expansion of volumes for disordered structures, compared with experimental values.

2.3.7. Impact of ordering of metal atoms on hydrogen stability

It seems possible that ordered structures described in the previous sections may change trapping forces to hydrogen atoms compared to disordered phases. In order to assess the effects of the ordered structures on hydrogen storage behavior, we calculated the densities of states (DOSs) and bonding energies of H atoms in dihydrides for the ground-state structures and a random selection of disordered structures for $x = 1/2$.

Partial DOSs of each element of ordered structure GS7 and a disordered model constructed using the special quasirandom structure (SQS) [51] are compared in Fig. 2.8. Here we used the 2 × 2 × 2 SQS supercell in the unit of a CaF_2-type conventional cell. As seen in the figure, peaks at around -6 eV correspond to hybridization between metal and hydrogen atoms, with only a slight difference in the shapes of the peaks between ordered and disordered structures. Since shapes of other peaks are also similar, it is suggested that metal-hydrogen binding states in ordered and disordered configuration of metal atoms are analogous.

In addition to the partial DOS analysis above, bonding energies of a H atom in a crystal structure, ΔE, for both ordered and disordered models were calculated by taking the energy difference between $Ti_{16}V_{16}H_{64}$ and $Ti_{16}V_{16}H_{63}$ cells,

$$\Delta E = \mathrm{E}(\mathrm{Ti}_{16}\mathrm{V}_{16}\mathrm{H}_{63}) - \mathrm{E}(\mathrm{Ti}_{16}\mathrm{V}_{16}\mathrm{H}_{64}) + \frac{1}{2}E(\mathrm{H}_2)\,, \tag{9}$$

where $E(H_2)$ is the energy of an H_2 molecule. H atoms in dihydrides occupy interstitial tetrahedral sites, so there are four coordinating metal atoms around an H atom, namely, five possible tetrahedral environments: four Ti atoms, three Ti and one V atoms, two Ti and two V atoms, one Ti and three V atoms, and four V atoms, which are represented as 4Ti, 3Ti+1V, 2Ti+2V, 1Ti+3V, and 4V, respectively. Since ordered GS7 has the layered structure containing Ti and V bilayers, three types of tetrahedrons, 4Ti, 2Ti+2V, and 4V, are possible around an H atom. For the disordered case, we

examined two types of SQS model, having different coordination environments around H; three types of tetrahedrons in SQS model 1 and all five types in SQS model 2.

Figure 2.9 shows the relation between ΔE and the coordination environments around an extracted H atom. Differences in ΔE between H atom sites for a type of coordination environment are less than about 30 meV as independent of the degree of ordering. It is, therefore, considered that the stability of H atoms is not much affected by the long-range ordering of metal atoms but the local coordinating environments around the H atoms. We also find in the figure that the bonding energy decreases as the V content of the tetrahedron increases. Since lower bonding energy of an H atom means that stronger bonding is created around the atom, our results indicate that H atoms within the 4V nearest tetrahedra have stronger bonding than those within the 4 Ti tetrahedra. This is consistent with the experimental trend derived from diffusion model analyses based on NMR data [11].

Bonding energy defined in Eq. (9) is based on the assumption that both dihydride and $Ti_{16}V_{16}H_{63}$ (or hydride $Ti_{0.5}V_{0.5}H_y$ with y = 1.96875) have a CaF_2-type structure. Liang *et al.* reported heats of formation of the CaF_2-type TiH_y using first-principles calculations [52], and the value of bonding energy between $Ti_{32}H_{64}$ and $Ti_{32}H_{63}$ calculated from their results is 0.855 eV. The values of bonding energies at 4Ti in Fig. 2.9 are distributed over a range from 0.704 to 0.737 eV, which are in the same order of magnitude compared with previously reported value. Because bonding energy decreases as the V content increases, it seems plausible that bonding energies at 4Ti which are affected by the further-coordinated V atoms are lower than those of the Ti-H system.

In summary, our results show that in this system there is not much difference whether the alloy is ordered or disordered, in other words, formation of ordered structures instead of disordered structures does not alter the hydrogenation thermodynamics significantly for Ti-V hydrides with the H/M ratio close to 2.

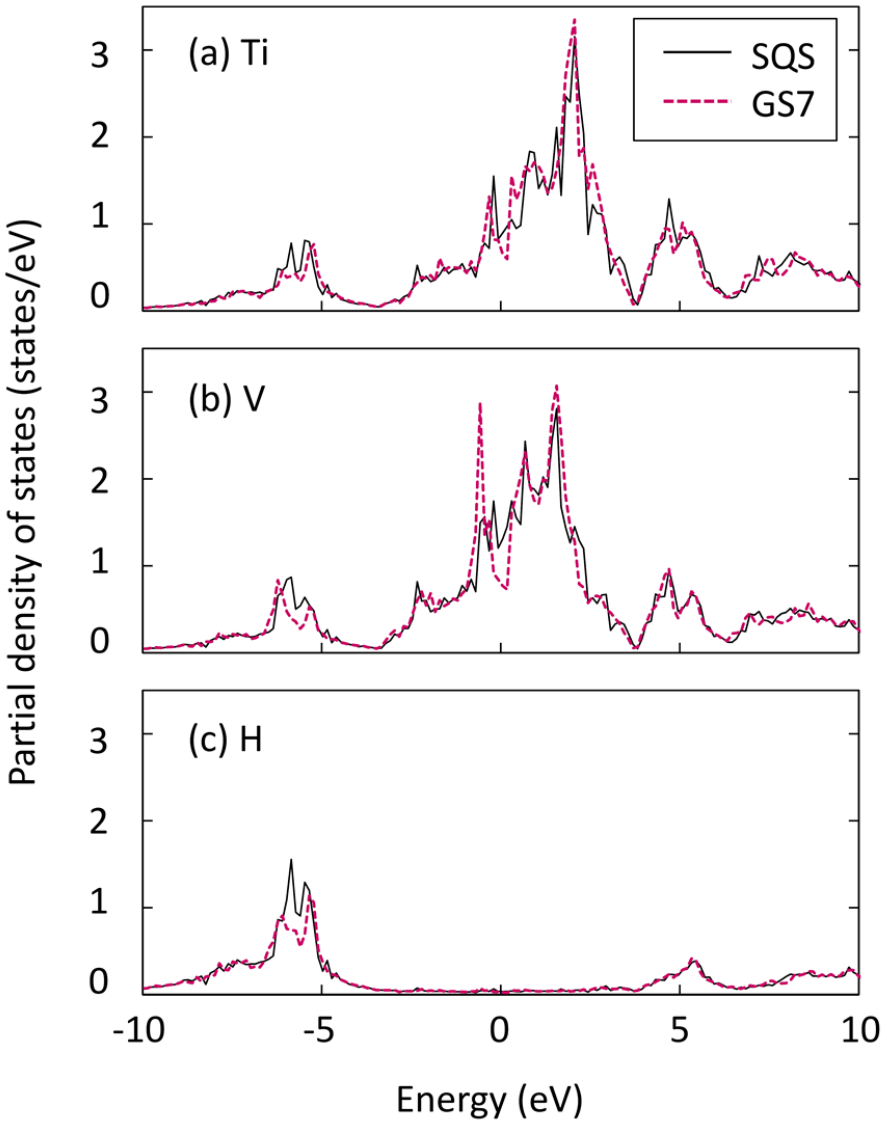

Fig. 2.8. Partial densities of states of (a) Ti, (b) V, and (c) H for ordered (GS7) and disordered (SQS) structures of $Ti_{0.5}V_{0.5}H_2$. Energies are measured from the Fermi level.

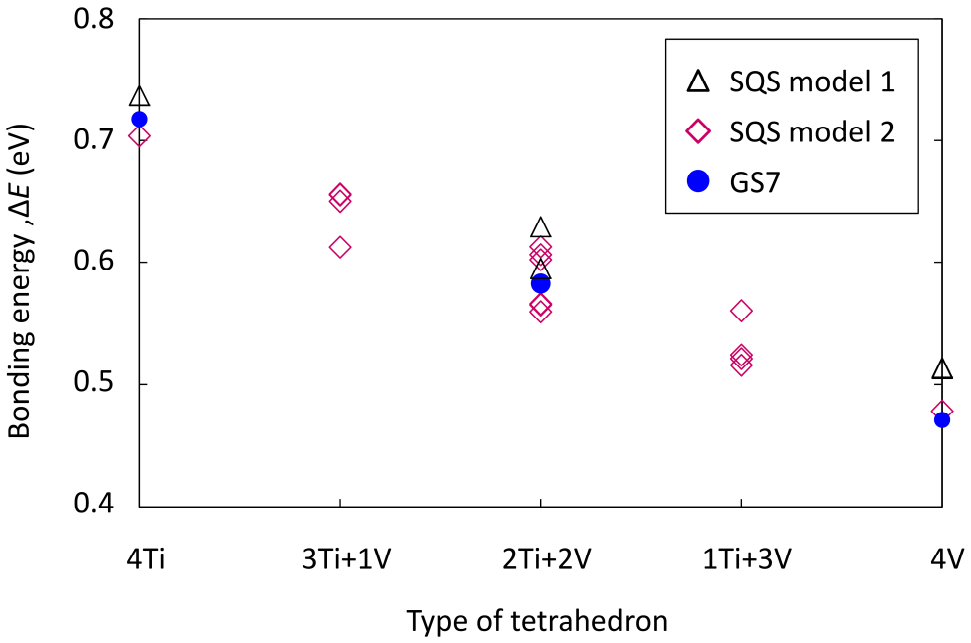

Fig. 2.9. Bonding energies, ΔE, between $Ti_{16}V_{16}H_{64}$ and $Ti_{16}V_{16}H_{63}$ for the ordered structure (GS7) and two disordered structures (SQS). The horizontal axis indicates the type of tetrahedron around an H atom.

2.4. Conclusions

Solid solution states of Ti-V dihydrides have been investigated using first-principles calculations and the cluster expansion method in order to clarify effects on hydrogen storage capacities. It is found that the dihydrides form stable solution with 9 ground-state structures identified from 154,156 candidate structures using 46 clusters with up to five atoms interactions. Most of the ground states have layered structures containing V bilayers, which are not known experimentally. Analysis of the effect of clusters on ground-state stability suggests that, while pair clusters contribute to the preference for layered structure formation, the higher-body clusters stabilize V bilayers over Ti bilayers. Those layered structures are found to have phase-separation tendency from analysis of short-range order parameters. It seems that disordered solutions will be formed under typical synthesis conditions from order-disorder transition temperatures of ordered ground-state structures, which are estimated from MC simulations to be less than 460 K, and comparison of lattice parameters with experimental values. The examination of the bonding energies of H atoms indicates that the bonding strength of hydrogen in Ti-V dihydrides is not greatly affected by the metal-atom ordering. Our results give an indication that trapping of stored hydrogen atoms hardly occur in grain interior of the dihydrides.

Appendix A: Cross-validation (CV) scores from cluster analysis of the structure populations (CASP)

In Sec. 2.3.1, we described the optimization procedure for deriving electronic effective cluster interactions (ECIs) based on least-square fitting to density functional theory (DFT) energies. Structures for DFT calculations were selected from all possible configurations with relatively small unit cells, which are 2,279 independent configurations containing up to 10 metal atoms in this study. CV scores measuring the difference between energies in the cluster expansion (CE) and DFT calculations were used as a measure of accuracy. If structures for DFT calculations are selected randomly from all possible configurations, they are possibly biased in terms of configurational characteristics. CV scores, however, are averaged indices of accuracy, so that they are not suitable to judge the bias in the selection of structures. In order to avoid biased selection, Seko *et al.* developed the cluster analysis of structure populations (CASP) method [39]. According to this method, configuration space is divided into smaller spaces by using characteristics of pair correlation functions, and the same number of DFT structures is extracted from each group. The CASP method is of use in selection of structures for DFT calculations efficiently and properly.

We used the CASP method with 2,279 CaF_2-type structures containing up to 10 metal atoms. Correlation functions of 12 independent clusters, namely the null cluster, point cluster, and 10 pair clusters were used for grouping. The structure population was divided into 10 groups containing 393, 547, 262, 425, 65, 105, 195, 231, 28, and 28 structures. Next, the convergence of the CV scores with the number of DFT structures (N_{DFT}) and clusters (N_{clusters}) was examined. The same number of structures was chosen randomly from each group. Figure A1 shows the dependence of CV scores for individual groups (CV-CASPs) on N_{DFT} when N_{clusters} is 25. While the total CV

score almost converges when N_{DFT} = 150 and $N_{clusters}$ = 25 (to within 1.8 meV/cation), CV-CASPs for each group do not converge. For example, the differences of values of CV-CASPs at N_{DFT} = 100 and 150 are more than 0.5 meV/f.u. in the case of Group 2, 4, 6 and 9. In order to improve convergence of CV-CASPs, more structures had to be added to the list of DFT calculations. In this study, we calculated CV-CASPs for $N_{DFT} \leq 280$ (the maximal value), and determined to use 280 structures to construct ECIs. Figure A2 shows the dependence of CV scores on $N_{clusters}$ for N_{DFT} = 280. The CV scores decrease as the number of clusters increases, and converge when $N_{clusters}$ = 25. We thus concluded that at least 280 DFT structures and 25 clusters are required to determine the initial ECIs in this step.

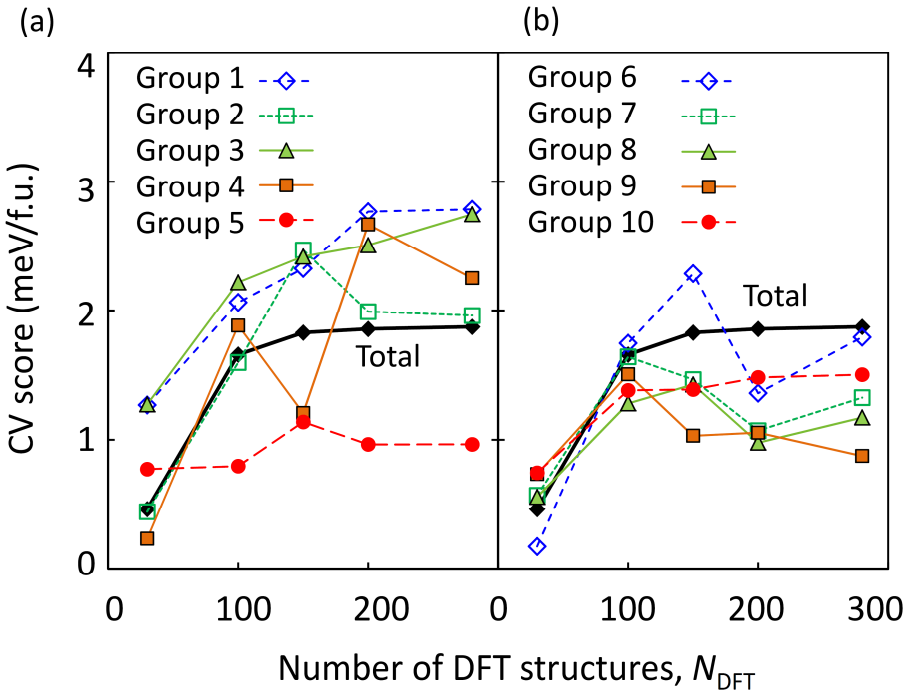

Fig. A1. Dependence of CV-CASPs on the number of input DFT structures, N_{DFT}, for (a) groups 1-5 and (b) groups 6-10 when 25 clusters are used. Total CV scores are also shown.

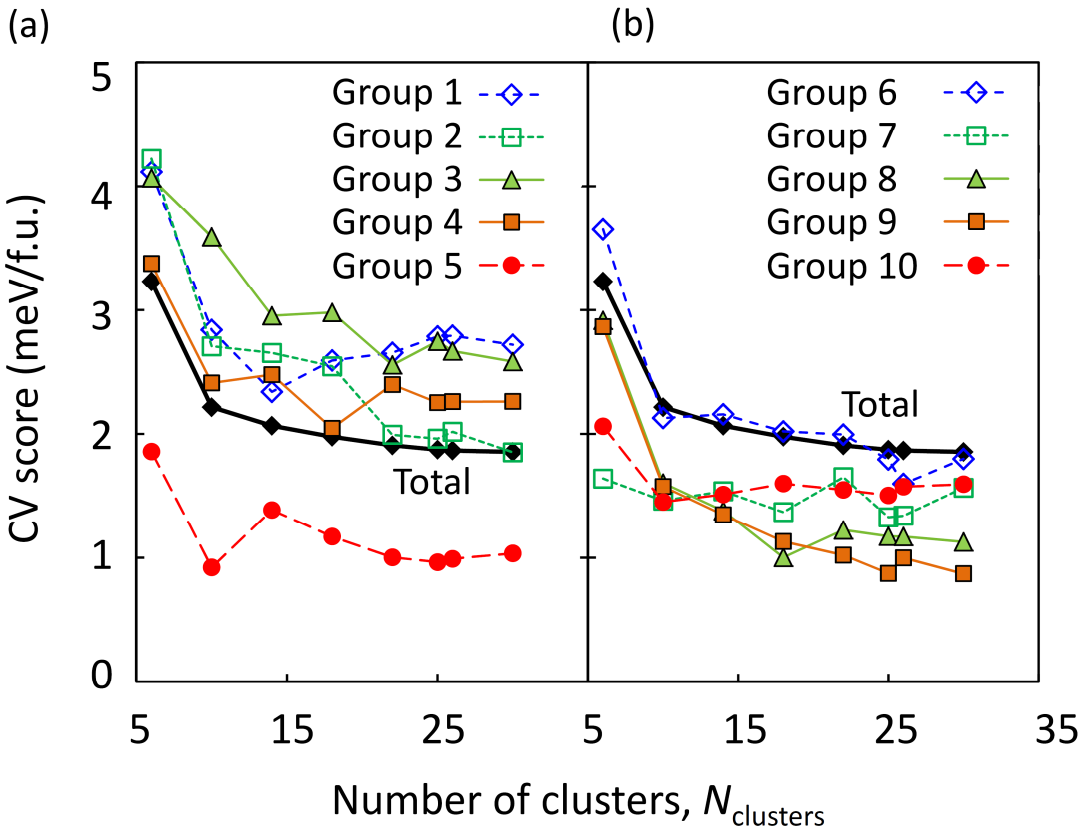

Fig. A2. Dependence of CV-CASPs on the number of clusters, $N_{clusters}$, for (a) groups 1-5 and (b) groups 6-10 when 280 DFT structures are used. Total CV scores are also shown.

Appendix B: A cluster expansion study of solid solution states of $Ti_{1-x}V_x$

B.1. Introduction

Unlike the dihydrides, structures of the end members of Ti-V binary alloys are different: Ti shows an hcp crystal structure, while V has a bcc lattice. The previously obtained phase diagram of Ti-V binary alloys shows the existence of a bcc solid solution above 900 K except in the Ti-rich region, and these alloys show dissociation behavior to a Ti-rich hcp phase and a V-rich bcc phase at lower temperatures [10]. There is, however, no experimental information on the phase diagram of Ti-V binary system below 500 K.

Theoretically, the solution states of Ti-V binary alloys have been studied by Chinnappan *et al.* [30] using the CE method to verify the experimental phase diagram via the CALPHAD method. They conclude that Ti-V binary alloys show the phase-separation tendency in the low temperature region. In this study, they selected ten clusters for the hcp system and six clusters for the bcc system from pair and three-body clusters to construct ECIs, and ground states were searched by comparing formation energies of about hundreds of possible configurations. In order to examine the effects of taking on higher-body clusters and much more configurations of metal atoms, we performed the CE analysis on $Ti_{1-x}V_x$ binary alloys based on the methods applied for $Ti_{1-x}V_xH_2$.

B.2. Methods

The solid solution states of Ti-V binary alloys were investigated using first-principles calculations together with the CE method based on the procedure applied to Ti-V dihydrides. Since structures of end members in the Ti-V system are different, the CE analysis was implemented for

two different systems, i.e. hcp-based or bcc-based cells. The ground-state structures were searched from 90,860 structures in hcp-based system and 154,156 bcc-based structures, each of which contained between two and sixteen metal atoms in the unit cell. In the case of the hcp system, we selected 107 clusters with up to five-body interactions (10 pairs, 33 three-body, 31 four-body, and 31 five-body clusters) as candidate components, while 97 clusters (6 pairs, 25 three-body, 27 four-body, and 37 five-body clusters) were selected for the bcc system. The CASP method was also applied to construct initial ECIs, and 948 hcp and 2,279 bcc non-equivalent configurations containing up to ten metal atoms were selected respectively. After the first optimizations of ECIs, CE energies of extended sets of configurations were calculated using the initial ECIs, and ground-state structures were identified. DFT calculations were performed using the same computational conditions mentioned in Sec. 2.2.2. Formation energies of Ti-V alloys were obtained using the calculated total energies of hcp-Ti, bcc-V, and Ti-V binary alloys.

B.3. Results

First, we compared lattice constants of the end structures in the system, hcp-Ti and bcc-V, calculated with geometry optimizations with experimental data. We obtained $a = 2.935$ and $c = 4.653$ for hcp-Ti, while $a = 2.950$ and $c = 4.681$ are known from X-ray diffraction measurements [53]. For bcc-V, values of parameter a obtained from DFT computations and X-ray measurements were 2.991 and 3.030 [54], respectively. The calculated lattice constants are within a range of 1.2 % from experimentally observed values, and are regarded to succeed in reproduce the experimental tendencies.

We determined initial ECIs of the hcp system with 144 configurations for DFT calculations and 30 clusters, and those of the bcc system with 369 configurations and 25 clusters.

Starting from the initial ECIs of each system, the configurational spaces were expanded to include 90,860 hcp-based configurations and 154,156 bcc-based configurations, respectively. The optimal ECIs of the hcp system were constructed using N_{DFT} = 398 and $N_{clusters}$ = 75, and using N_{DFT} = 511 and $N_{clusters}$ = 50 for the bcc system.

The obtained formation energies are plotted in Fig. B1 with overlaying plots of hcp-based (denoted by blue circles) and bcc-based configurations (denoted by black triangles). Contrary to the case of Ti-V dihydrides (Fig. 2.2.), all possible configurations have positive formation energies so that Ti-V alloys are suggested to exhibit phase separation behavior to hcp Ti-rich phase and bcc V-rich phase at 0 K. This tendency matches with what Chinnappan *et al.* have claimed in Ref. [30]. No preference of forming Ti and V stacking layers is observed in the Ti-V alloy system, which is contrasting to the Ti-V dihydrides exhibiting preference for layered structures containing V bilayers. This difference is seemed to be affected by the existence of interstitial H atoms, but further investigations are required to evaluate the relation between metal-atom ordering and H atoms within a hydride.

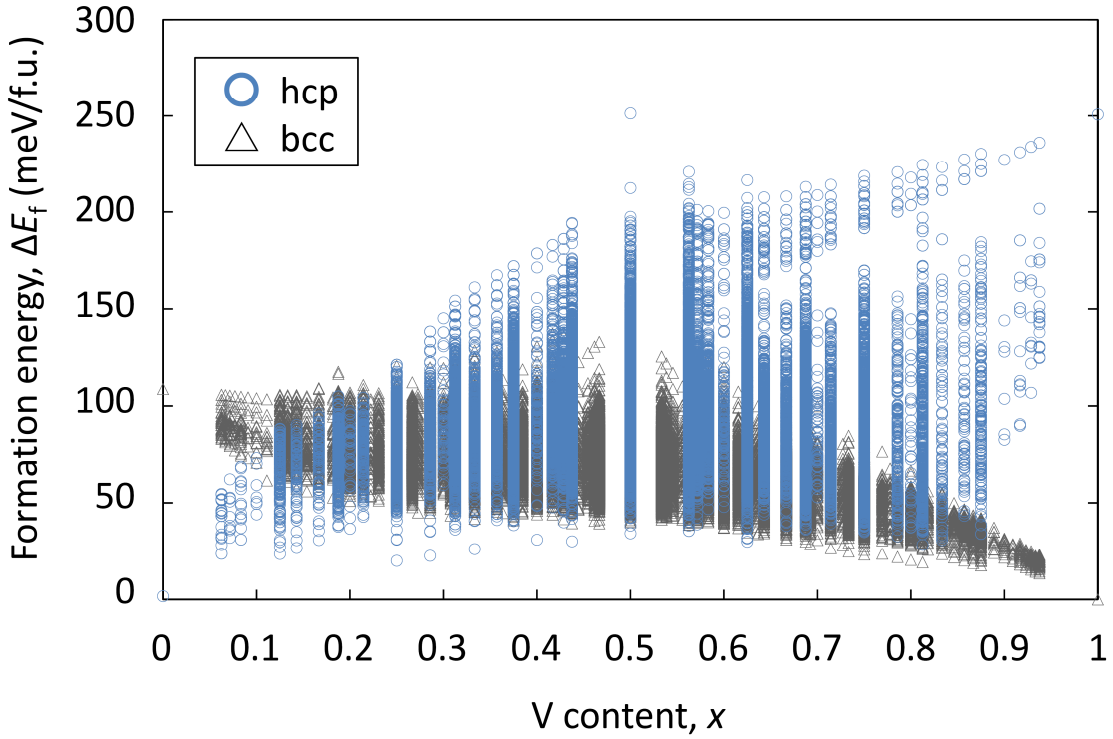

Fig. B1. Formation energies of all symmetrically independent structures of $Ti_{1-x}V_x$, calculated using the cluster expansion method. Blue circles and black triangles indicate the formation energies of configurations belong to the hcp-based system and the bcc-based system, respectively.

References

[1] H. Nagel, R.S. Perkins, Crystallographic investigation of ternary titanium vanadium hydrides, Z. Metallkd. 66 (1975) 362–366.

[2] T. Hagi, Y. Sato, M. Yasuda, K. Tanaka, Structure and phase diagram of Ti–V–H system at room temperature, Trans. Jpn. Inst. Met. 28 (1987) 198–204.

[3] H. Kim, K. Sakaki, I. Saita, H. Enoki, K. Noguchi, A. Machida, T. Watanuki, Y. Nakamura, Reduction and unusual recovery in the reversible hydrogen storage capacity of $V_{1-x}Ti_x$ during hydrogen cycling, Int. J. Hydrogen Energy 39 (2014) 10546–10551.

[4] J.J. Reilly, R.H. Wiswall, The higher hydrides of vanadium and niobium, Inorg. Chem. 9 (1970) 1678–1682.

[5] E. Akiba, H. Iba, Hydrogen absorption by Laves phase related BCC solid solution, Intermetallics 6 (1998) 461–470.

[6] H. Kim, K. Sakaki, H. Ogawa, Y. Nakamura, J. Nakamura, E. Akiba, A. Machida, T. Watanuki, T. Proffen, Origin of degradation in the reversible hydrogen storage capacity of $V_{1-x}Ti_x$ alloys from the atomic pair distribution function analysis, J. Phys. Chem. C 117 (2013) 26543–26550.

[7] K. Mori, K. Iwase, M. Sugiyama, M. Kofu, O. Yamamuro, Y. Onodera, T. Otomo, T. Fukunaga, Neutron scattering studies of Ti-Cr-V bcc alloy with the residual hydrogen and deuterium, J. Phys. Conf. Ser. 340 (2012) 12103.

[8] S. Ohnuki, T. Yasuda, T. Suda, S. Watanabe, B.M. Oliver, Effect of alloying elements and neutron-irradiation on hydrogen behavior in V alloys, J. Nucl. Mater. 329–333 (2004) 481–485.

[9] S.D. Findlay, T. Saito, N. Shibata, Y. Sato, J. Matsuda, K. Asano, E. Akiba, T. Hirayama, Y. Ikuhara, Direct imaging of hydrogen within a crystalline environment, Appl. Phys. Express 3 (2010) 116603.

[10] T.B. Massalski, Binary Alloy Phase Diagrams, 2nd ed., ASM International, Ohio, 1990.

[11] T. Ueda, S. Hayashi, K. Hayamizu, Hydrogen motion and local structure of metals in β-$Ti_{1-y}V_yH_x$ as studied by ^{1}H NMR, Phys. Rev. B 48 (1993) 5837–5843.

[12] T. Ueda, S. Hayashi, Y. Nakai, S. Ikeda, Local structure in β-$Ti_{1-y}V_yH_x$ studied by inelastic neutron scattering, Phys. Rev. B 51 (1995) 5725–5731.

[13] B. Nowak, S. Hayashi, K. Hayamizu, O. Yamamoto, X-ray diffraction and ^{1}H and ^{51}V NMR study of the structure of a Ti-V-H alloy in relation to preparation conditions, J. Less-Common Met. 123 (1986) 75–84.

[14] S. Hayashi, K. Hayamizu, O. Yamamoto, Structure of $Ti_{1-y}V_yH_x$ alloys studied by X-ray diffraction and by ^{1}H and ^{51}V NMR, J. Solid State Chem. 46 (1983) 306–312.

[15] S. Hayashi, K. Hayamizu, O. Yamamoto, ^{1}H and ^{51}V nuclear magnetic resonance study of the precipitation of a titanium hydride phase with a face-centred cubic structure in the Ti-V-H system, J. Less-Common Met. 113 (1985) 1–9.

[16] S. Hayashi, K. Hayamizu, X-ray diffraction and ^{1}H and ^{51}V NMR study of the Ti-V-H system, J. Less-Common Met. 161 (1990) 61–75.

[17] N. Skryabina, D. Fruchart, M.G. Shelyapina, S.K. Dolukhanyan, A. Aleksanyan, Phase transformations in Ti–V hydrides, J. Alloys Compd. 580 (2013) S94–S97.

[18] J. Matsuda, Y. Nakamura, E. Akiba, Microstructure of Ti–V–Mn BCC alloys before and after hydrogen absorption–desorption, J. Alloys Compd. 509 (2011) 4352–4356.

[19] R.C. Brouwer, J. Rector, N. Koeman, R. Griessen, Hydrogen as a local probe: Diffusion and short-range order in $Ti_{1-y}V_y$ alloys, Phys. Rev. B 40 (1989) 3546–3559.

[20] D.T. Peterson, S.O. Nelson, Isopiestic solubility of hydrogen in vanadium alloys at low temperatures, Metall. Trans. A 16 (1985) 367–374.

[21] D.J. Pine, R.M. Cotts, Diffusion and electrotransport of hydrogen and deuterium in vanadium-titanium and vanadium-chromium alloys, Phys. Rev. B 28 (1983) 641–647.

[22] S. Tanaka, H. Kimura, Solubility and diffusivity of hydrogen in vanadium and its alloys around room temperature, Trans. JIM 20 (1979) 647–658.

[23] J.M. Sanchez, F. Ducastelle, D. Gratias, Generalized cluster description of multicomponent systems, Physica A 128 (1984) 334–350.

[24] D. De Fontaine, Cluster approach to order-disorder transformations in alloys, Solid State Phys. 47 (1994) 33–176.

[25] V. Ozoliņš, C. Wolverton, A. Zunger, Cu-Au, Ag-Au, Cu-Ag, and Ni-Au intermetallics: First-principles study of temperature-composition phase diagrams and structures, Phys. Rev. B 57 (1998) 6427–6443.

[26] A. van de Walle, G. Ceder, Automating first-principles phase diagram calculations, J. Phase Equilibria 23 (2002) 348–359.

[27] B. Liu, A. Seko, I. Tanaka, Cluster expansion with controlled accuracy for the MgO/ZnO pseudobinary system via first-principles calculations, Phys. Rev. B 86 (2012) 245202.

[28] S. Müller, A. Zunger, First-principles predictions of yet-unobserved ordered structures in the Ag-Pd phase diagram, Phys. Rev. Lett. 87 (2001) 165502.

[29] Q. Wu, B. He, T. Song, J. Gao, S. Shi, Cluster expansion method and its application in computational materials science, Comput. Mater. Sci. 125 (2016) 243–254.

[30] R. Chinnappan, B.K. Panigrahi, A. van de Walle, First-principles study of phase equilibrium in Ti–V, Ti–Nb, and Ti–Ta alloys, Calphad 54 (2016) 125–133.

[31] Q. Xu, A. Van der Ven, First-principles investigation of metal-hydride phase stability: The Ti-H system, Phys. Rev. B 76 (2007) 64207.

[32] S. Suwarno, J.K. Solberg, J.P. Mæhlen, R.V. Denys, B. Krogh, E. Ochoa-Fernández, B.T. Børresen, E. Rytter, I.E. Gabis, V.A. Yartys, Non-isothermal kinetics and in situ SR XRD studies of hydrogen desorption from dihydrides of binary Ti–V alloys, Int. J. Hydrogen Energy 38 (2013) 14704–14714.

[33] J.-H. Kim, H. Lee, P.S. Lee, C.-Y. Seo, J.-Y. Lee, A study on the improvement of the cyclic durability by Cr substitution in V–Ti alloy and surface modification by the ball-milling process, J. Alloys Compd. 348 (2003) 293–300.

[34] A. Seko, Y. Koyama, I. Tanaka, Cluster expansion method for multicomponent systems based on optimal selection of structures for density-functional theory calculations, Phys. Rev. B 80 (2009) 165122.

[35] G.L.W. Hart, V. Blum, M.J. Walorski, A. Zunger, Evolutionary approach for determining first-principles hamiltonians, Nat. Mater. 4 (2005) 391–394.

[36] V. Blum, G.L.W. Hart, M.J. Walorski, A. Zunger, Using genetic algorithms to map first-principles results to model Hamiltonians: Application to the generalized Ising model for alloys, Phys. Rev. B 72 (2005) 165113.

[37] M. Stone, Cross-validatory choice and assessment of statistical predictions, J. R. Stat. Soc. Ser. B. Methodol. 36 (1974) 111–147.

[38] N.A. Zarkevich, D.D. Johnson, Reliable first-principles alloy thermodynamics via truncated cluster expansions, Phys. Rev. Lett. 92 (2004) 255702.

[39] A. Seko, I. Tanaka, Grouping of structures for cluster expansion of multicomponent systems with controlled accuracy, Phys. Rev. B 83 (2011) 224111.

[40] P.E. Blöchl, Projector augmented-wave method, Phys. Rev. B 50 (1994) 17953–17979.

[41] G. Kresse, D. Joubert, From ultrasoft pseudopotentials to the projector augmented-wave method, Phys. Rev. B 59 (1999) 1758–1775.

[42] J.P. Perdew, K. Burke, M. Ernzerhof, Generalized gradient approximation ade simple, Phys. Rev. Lett. 77 (1996) 3865–3868.

[43] J.P. Perdew, J. Chevary, S. Vosko, K. Jackson, M. Pederson, D. Singh, C. Fiolhais, Erratum: Atoms, molecules, solids, and surfaces: Applications of the generalized gradient approximation for exchange and correlation, Phys. Rev. B 48 (1993) 4978–4978.

[44] G. Kresse, J. Hafner, Ab initio molecular dynamics for liquid metals, Phys. Rev. B 47 (1993) 558–561.

[45] G. Kresse, J. Furthmüller, Efficient iterative schemes for ab initio total-energy calculations using a plane-wave basis set, Phys. Rev. B 54 (1996) 11169–11186.

[46] H.J. Monkhorst, J.D. Pack, Special points for Brillouin-zone integrations, Phys. Rev. B 13 (1976) 5188–5192.

[47] A. San-Martin, F.D. Manchester, The H−Ti (Hydrogen-Titanium) system, Bull. Alloy Phase Diagrams 8 (1987) 30–42.

[48] C.H. Hu, D.M. Chen, Y.M. Wang, K. Yang, First-principles investigations of isotope effects in thermodynamic properties of TiX_2 (X=H, D, and T) system, J. Alloys Compd. 450 (2008) 369–374.

[49] H. Müller, K. Weymann, Investigation of the ternary systems Nb-V-H and Ta-V-H, J. Less-Common Met. 119 (1986) 115–126.

[50] T. Wang, F. Eichhorn, D. Grambole, R. Groetzschel, F. Herrmann, U. Kreissig, W. Moeller, A new Ti/H phase transformation in the H^+_2 titanium alloy studied by x-ray diffraction, nuclear reaction analysis, elastic recoil detection analysis and scanning electron microscopy, J. Phys. Condens. Matter 14 (2002) 11605–11614.

[51] A. Zunger, S.-H. Wei, L.G. Ferreira, J.E. Bernard, Special quasirandom structures, Phys. Rev. Lett. 65 (1990) 353–356.

[52] C.P. Liang, H.R. Gong, Atomic structure, mechanical quality, and thermodynamic property of TiHx phases, J. Appl. Phys. 114 (2013) 43510.

[53] N. Schmitz-Pranghe, P. Duenner, Gitterstruktur und thermische Ausdehnung der Uebergangsmetalle Scandium, Titan, Vanadin und Mangan, Z. Metallkd. 59 (1968) 377–382.

[54] J.L. Jorda, J. Muller, The vanadium-rhenium system: Phase diagram and superconductivity, J. Less-Common Met. 119 (1986) 337–345.

Chapter 3

Equilibrium hydrogen pressures in the V-H system from first-principles calculations

3.1. Introduction

Vanadium-based alloys are considered to be promising hydrogen storage materials because their storage capacities can reach up to 4 mass% and they show good cyclic stability [1–3]. Equilibrium hydrogen pressures, $P_{H_2}^{eq}$, of these alloys strongly depend on the compositions [4–10]. Because V can be alloyed with various transition metals, it should be possible to identify compounds with suitable ranges of $P_{H_2}^{eq}$ for practical applications. Although many experimental studies have been devoted to elucidating the relation between pressure and composition in many cases, how $P_{H_2}^{eq}$ depends on the composition remains unclear. Theoretical evaluation of $P_{H_2}^{eq}$ of these hydrogen storage alloys represents a powerful tool for understanding and controlling the behavior of $P_{H_2}^{eq}$.

Two main theoretical approaches are commonly used to estimate $P_{H_2}^{eq}$, viz., semi-empirical approaches such as those based on the CALPHAD method, and first-principles approaches. With the CALPHAD method, thermodynamic calculations are performed based on experimental and first-principles thermodynamic data, (the latter substituting for otherwise unavailable experimental thermodynamic data), to generate pressure-composition-temperature (PCT) curves. With respect to V-based alloys, Ukita *et al.* reported a CALPHAD-type analysis of the V-H system [11], and Kim *et al.* expanded this work to V-M-H (M = Al, Co, Fe, Ni) systems

[12]. On the other hand, there are few reports of first-principles approaches being used to study V-based hydrides, although they have been applied to the study of metal alanates and borohydrides [13,14], and PuH_x where $2 \leq x \leq 3$ [15]. First-principles calculations require well-defined structural models of the compound in question before and after hydrogenation. If the crystal structure or lattice positions of metal and H atoms in such compounds are not known, it is very difficult to use first-principles calculations to estimate $P_{H_2}^{eq}$. In this study, we focus on the V-H system, which is the simplest of the V-based hydrides and has a long history of experimental measurements.

Pure vanadium metal has a bcc structure, while the dihydrides, VH_2, a CaF_2-type structure. Between these two end members are some intermediate phases as depicted in Fig. 3.1 [16], with at least two plateaus appearing in the PCT curve [4,5]. In the intermediate phases, H atoms typically occupy interstitial tetrahedral (T) and octahedral (O) sites in a bcc lattice as illustrated in Fig. 3.2 [17]. The lower $P_{H_2}^{eq}$ plateau corresponds to V-$VH_{0.5}$, where $VH_{0.5}$ is divanadium hydride (DVH). From X-ray diffraction data, the crystal structure of $VH_{0.5}$ is thought to be monoclinic similar to that of bct [18]. From neutron diffraction experiments, it is known that H atoms in monoclinic $VH_{0.5}$ occupy half the O_z sites, labelled O_{z1}, in an ordered arrangement as depicted in Fig. 3.3 [19–21] (using the VESTA code[22]).

Further hydrogenation of vanadium hydrides to form VH_2, corresponding to the higher $P_{H_2}^{eq}$ plateau, is not well characterized because the boundaries between intermediate phases are difficult to define. In analogy with many other V-based alloys, e.g., Ti-V and Ti-V-Mn, in which monohydrides (metal/hydrogen ratio close to 1) are known to form, the higher-plateau region of the PCT curve for the V-H system is likely VH-VH_2, as assumed previously [9,23]. Although the structure of VH has not been determined directly by experiment, vanadium hydrides with compositions near to VH are known to form a bct lattice with $c/a \sim 1.13$ [24]. With regard to H

positions in VH, while a neutron diffraction study of the V-H phases by Asano *et al.* suggested that hydrogen in VH occupies O_z sites [20], a neutron diffraction study by Kajitani *et al.* found that signals from H atoms indicate they are not only distributed over O_z sites but also over surrounding T sites [25]. Recently, Miwa *et al.* claimed, based on results of molecular dynamics simulations with machine-learning-derived potentials, that H atoms in VH sit on T sites for long periods of time, occasionally hopping between the T sites via intermediate O_z-site positions [26], resulting in a spread of H signals as observed by neutron diffraction. However, as suggested by Yagi *et al.* [27], there remains the possibility that the large vibrational amplitude of H atoms on O sites induces the broadened signal. In other words, there is still some uncertainty regarding the positions of H atoms in intermediate vanadium hydride phases.

In this study, we estimate the equilibrium hydrogen pressures, $P_{\mathrm{H_2}}^{\mathrm{eq}}$, of two reactions, namely (I)vanadium metal to $VH_{0.5}$ and (II)VH to VH_2, based on a structural search of all possible T- and O-site configurations of hydrogen atoms using first-principles calculations. This is done by first exploring the energetical landscape using a relatively large number of unique atom configurations without including vibrational contributions. Next, the ground-state energies of the low-energy configurations found in the first step are calculated by including vibrational free energies, from which $P_{\mathrm{H_2}}^{\mathrm{eq}}$ are derived.

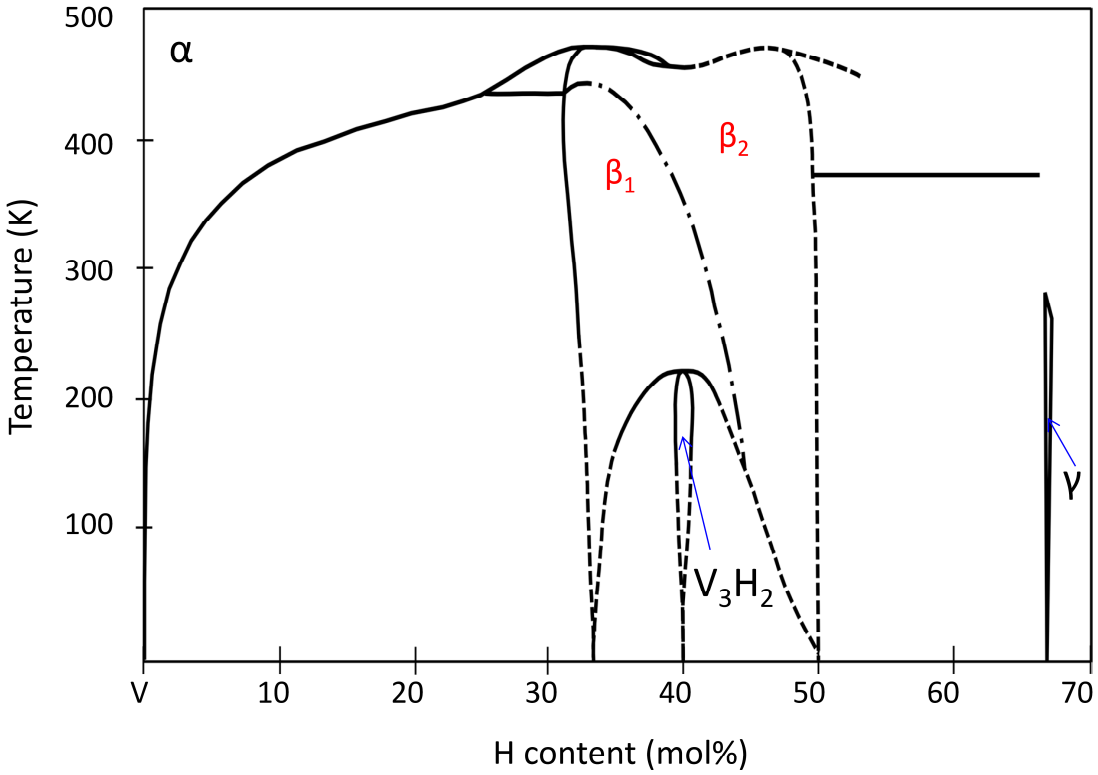

	α	β_1	β_2	γ
H/M	0	0.5	<1	2
Space group	$Im\bar{3}m$	$C2/m$	$I4_1/amd$	$Fm\bar{3}m$
Lattice	bcc	pseudo-bct	bct	fcc
H site	-	O_z	(O_z+T)	T

Fig. 3.1. Phase diagram of the V-H system (Ref. [16])

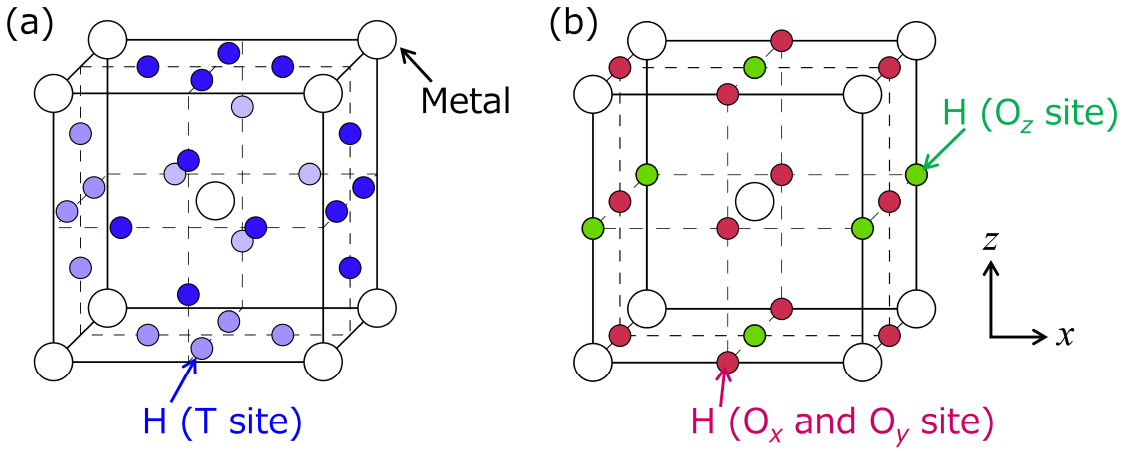

Fig. 3.2. (a) Tetrahedral (T) and (b) octahedral (O) interstitial hydrogen sites in a conventional bcc lattice of host metal V. O sites in (b) are classified as O_z (green filled circles), and O_x and O_y (red filled circles).

3.2. Calculation method

All possible symmetrically independent configurations of hydrogen atoms over interstitial T and O sites in $VH_{0.5}$ and VH are constructed using a 1 × 2 × 2 supercell of the bcc conventional unit cell (using the CLUPAN code [28]). This amounts to 2,111 T-site and 262 O-site configurations for $VH_{0.5}$, and 12,754 O-site configurations for VH. T-site configurations in VH were constructed using a 1 × 1 × 2 bcc supercell, producing 293 configurations. As a rule of thumb, hydrogen atoms in transition-metal hydrides are separated by at least 2.1 Å, which is known as Switendick criterion [29,30]. Taking the criterion into account, configurations with H atoms separated by more than 2.0 Å were excluded from the candidates. This reduced the number of configurations to be evaluated by first-principles calculations to 321 T-site and 109 O-site configurations for $VH_{0.5}$, and 10 T-site and 89 O-site configurations for VH. Structural relaxations were performed for these remaining initial structures. During relaxation, H atoms were able to move to different sites from their initial site, redistributing over both T and O sites.

Electronic energy calculations were performed in the framework of density functional theory (DFT) using the projector augmented-wave (PAW) method [31,32] and the generalized gradient approximation (GGA) [33,34] as implemented in the VASP code [35,36]. A cut-off energy for the plane-wave basis set of 400 eV was used for all calculations. Brillouin-zone integration was carried out based on the Monkhorst-Pack scheme [37] and *k*-point spacing was set at less than 0.15 $Å^{-1}$. In addition to atomic positions, both cell shape and volume were fully relaxed until the residual forces became less than 0.02 $eVÅ^{-1}$.

To take effects from lattice vibrations including zero-point vibrational contribution into consideration, we performed phonon calculations based on finite-difference method as implemented by the Phonopy code [38,39]. In the phonon calculations, supercells of the unit cell of target compounds with lattice constants longer than 9 Å were constructed. Vibrational free energies were

evaluated from calculated phonon. In this step, equilibrium structures were optimized until the residual forces became less than 0.0002 eVÅ^{-1}. Atomic displacement of 0.01 Å was used to construct the dynamical matrix.

We considered the following hydrogenation reactions of the V-H system:

$$\mathrm{V} + 1/4\mathrm{H_2} \Leftrightarrow \mathrm{VH_{0.5}}, \tag{1}$$

$$\mathrm{VH} + 1/2\mathrm{H_2} \Leftrightarrow \mathrm{VH_2}. \tag{2}$$

Equilibrium hydrogen pressures of these reactions were derived from Gibbs free energies of the constituent phases. The Gibbs free energy of hydrogen gas under equilibrium conditions, $G_{\mathrm{H_2}}\left(T, P_{\mathrm{H_2}}^{\mathrm{eq}}\right)$, is expressed as

$$G_{\mathrm{H_2}}\left(T, P_{\mathrm{H_2}}^{\mathrm{eq}}\right) = G_{\mathrm{H_2}}^{\mathrm{o}}(T) + k_B T \ln \frac{P_{\mathrm{H_2}}^{\mathrm{eq}}}{P_{\mathrm{H_2}}^{\mathrm{o}}}, \tag{3}$$

where $P_{\mathrm{H_2}}^{\mathrm{o}}$ indicates the standard hydrogen pressure and $G_{\mathrm{H_2}}^{\mathrm{o}}(T)$ is the Gibbs free energy at $P_{\mathrm{H_2}}^{\mathrm{o}}$. Using enthalpies ($H$) and entropy ($S$), $G_{\mathrm{H_2}}^{\mathrm{o}}(T)$ can be rewritten in the form

$$G_{\mathrm{H_2}}^{\mathrm{o}}(T) = H_{\mathrm{H_2}}^{\mathrm{o}}(0\ \mathrm{K}) + \Delta H_{\mathrm{H_2}}^{\mathrm{o}}(T) - TS_{\mathrm{H_2}}^{\mathrm{o}}(T), \tag{4}$$

where the quantities at finite temperatures are extracted from the NIST-JANAF database [40] and the enthalpy at 0 K is obtained by DFT calculations of H_2 molecules with ZPE. For the reaction $\alpha + x\mathrm{H_2} \Leftrightarrow \alpha'$, $P_{\mathrm{H_2}}^{\mathrm{eq}}$ is obtained from the following relation,

$$k_B T \ln \frac{P_{\mathrm{H_2}}^{\mathrm{eq}}}{P_{\mathrm{H_2}}^{\mathrm{o}}} = \frac{1}{x}(G_{\alpha'} - G_{\alpha}) - (H_{\mathrm{H_2}}^{\mathrm{o}}(0\ \mathrm{K}) + \Delta H_{\mathrm{H_2}}^{\mathrm{o}}(T) - TS_{\mathrm{H_2}}^{\mathrm{o}}(T)). \tag{5}$$

$G_{\alpha'}$ and G_{α} indicate Gibbs free energies of vanadium compounds after and before hydrogenation reaction, respectively. Each of the free energies consists of contributions from static ground-state energy and vibrational free energy.

3.3. Results and discussion

3.3.1. Configurations of $VH_{0.5}$ without vibrational contributions

We calculated electronic energies of all $VH_{0.5}$ (DVH) structures generated. The distribution of energies relative to the lowest energy, ΔE_{DVH}, is shown in Fig. 3.3(a). This plot includes data for 366 of the 430 configurations; we note that it is possible that the energy of the same structure is included more than once because different initial configurations can relax to the same optimized structure during structural relaxation. The structures are labelled DVH-1, DVH-2, DVH-3,..., in ascending order of ΔE_{DVH}. As seen in Fig. 3.3(a), although a few structures have ΔE_{DVH} values less than 10 meV/f.u., the majority are distributed over a range of values from 32 to 52 meV/f.u. Hydrogen sites and structural parameters of the 8 most stable structures, DVH-1 to DVH-8, are summarized in Table 3.I, together with experimental data [18]. In the table, lattice parameters a_0 and c_0 for the bct-like conventional cell are listed (see Fig. 3.3(b)). H-atom configuration in DVH-1 and DVH-2 are depicted in Fig. 3.3(b) and (c), respectively.

The sites occupied by H atoms listed in Table 3.I show that H atoms in the lowest-energy structures occupy T sites in all cases except for DVH-6, in which H atoms order on half of all O_z sites, labelled O_{z1} and shown in Fig. 3.3(b) and (c) as grey spheres. In the case of DVH-2, DVH-3, DVH-4, and DVH-7, H atoms occupy T_z sites, which are T sites next to O_z sites in the same *xy* plane, as illustrated in Fig. 3.3(c) for the case of DVH-2. In DVH-1, however, H atoms occupy T_{z1} sites, which are ordered T_z sites uniformly displaced in the same direction from neighboring O_{z1} sites, as illustrated in Fig. 3.3(b). The distribution of H atoms on T sites is similar to that of H in $Ti_{25}V_{20}Cr_{50}Mo_5$ hydrides determined from neutron diffraction by Kamazawa *et al.* [41], but in the case of $VH_{0.5}$, similar experiments indicate a broad distribution of H atoms over O_{z1} sites.

All structures in Table 3.I except for DVH-6 were deemed to have pseudo-bcc crystal lattices. Here “pseudo-bcc” means a bcc-like cell with c_0/a_0 ratio in the range 1.00 ± 0.05. In these

structures, H atoms only occupy T sites. DVH-6 has a monoclinic crystal lattice with a monoclinic angle of $\alpha_0 = 90.19$, close to a bct crystal structure. The ratio of the lattice constants c_0/a_0 of DVH-6 is about 1.13, which is very different from the pseudo-bcc structures in Table 3.I. This difference in lattice constants and symmetry is considered to originate from H atoms occupying O_z site in DVH-6, where the H atoms locate on the middle of the V atoms aligned in the *c*-axis direction, extending the lattice constant along the *c* axis.

According to experiment, the structure of $VH_{0.5}$ has a bct-like monoclinic lattice with a monoclinic angle of $\alpha_0 = 90.25$ with H atoms occupying O_{z1} sites [18]. The ratio of the lattice constants c_0/a_0 is about 1.10, and no bcc-like crystal structure has been detected in X-ray diffraction patterns of vanadium hydrides. These experimental results are in good agreement with model DVH-6 in Table 3.I. Although the electronic energy of DVH-6 without ZPE is higher than DVH-1 by 12.8 meV/f.u., DVH-6 becomes more stable when vibrational effects are included, as described in Sec. 3.3.3.

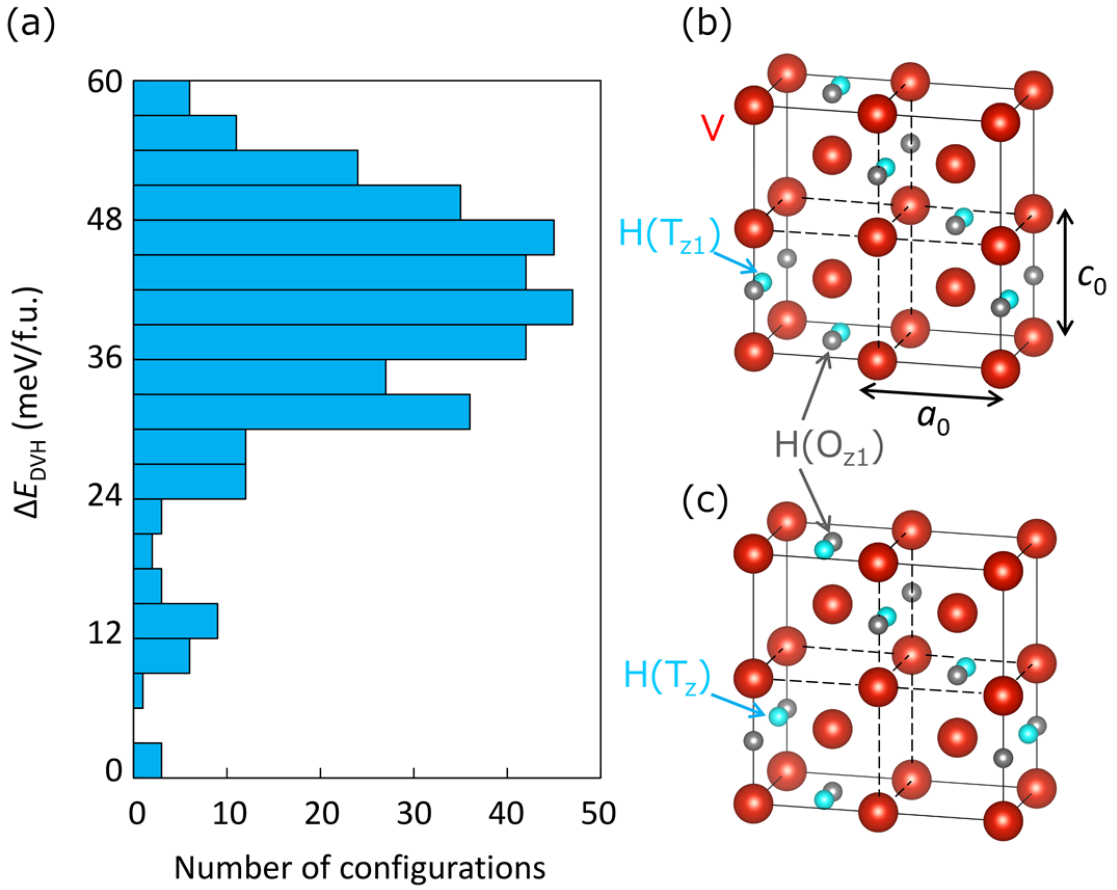

Fig. 3.3. (a) Histogram of electronic energies of configurations of $VH_{0.5}$ measured from the lowest energy, ΔE_{DVH}. (b) Positions of H atoms in the most stable structure (DVH-1) and (c) in the second most stable structure (DVH-2), where H atoms on O_{z1} sites are also shown as small grey spheres.

TABLE 3.I. H sites, lattice type of V atoms, lattice constants, and electronic energies for the 8 stable configurations of $VH_{0.5}$ (DVH). The bottom row contains experimental values. A crystal lattice is considered "pseudo-bcc" when the ratio of the lattice constants is in the range 1.00 ± 0.05. DVH-6 and the experimentally observed structure have monoclinic cells with monoclinic angles of $\alpha_0 = 90.19$ and 90.25, respectively. H site labels T_z, T_{z1}, and O_{z1} correspond to particular (or ordered) configurations of interstitial H atoms in Fig. 3.3.

Configuration	H sites	Structure	a_0 (Å)	c_0 (Å)	c_0/a_0	ΔE_{DVH} (meV/f.u.)
DVH-1	T_{z1}	pseudo-bcc	3.092	3.065	0.99	-
DVH-2	T_z	pseudo-bcc	3.077	3.084	1.00	0.7
DVH-3	T_z	pseudo-bcc	3.086	3.073	1.00	2.8
DVH-4	T_z	pseudo-bcc	3.088	3.070	0.99	8.6
DVH-5	T	pseudo-bcc	3.085	3.067	0.99	11.8
DVH-6	O_{z1}	monoclinic	2.947 2.934	3.328	1.13	12.8
DVH-7	T_z	pseudo-bcc	3.058 3.082	3.102	1.01	13.0
DVH-8	T	pseudo-bcc	3.048 3.046	3.147	1.03	13.3
exp. (Ref. [18])	O_{z1}	monoclinic	3.001	3.309	1.10	-

3.3.2. Configurations of VH without vibrational contributions

Calculated energies of 70 of the 99 VH configurations with energies below 200 meV/f.u. relative to the lowest energy, ΔE_{VH}, are plotted in Fig. 3.4(a). Results for duplicate structures may be included for the reasons given in the previous section. As with $VH_{0.5}$, the 9 lowest-energy structures are labelled VH-1 to VH-9 in ascending order of ΔE_{VH}. Compared with Fig. 3.3(a), the distribution of energies for VH configurations is wider. There are a small number of structures with $\Delta E_{\mathrm{VH}} < 50\ \mathrm{meV/f.u.}$ Hydrogen sites and structural parameters of the 9 lowest-energy structures are summarized in Table 3.II. Atomic configurations including H sites in models VH-1 and VH-2 are depicted in Fig. 3.4(b) and (c), respectively.

As in the case of DVH, H atoms occupy T sites in all cases except for VH-8, in which H occupies O_z sites. In VH-1, H atoms occupy T_z sites, with half of these sites displaced in one direction within the *xy* plane from O_z sites, and the other half displaced in the opposite direction, as depicted in Fig. 3.4(b). In VH-2, depicted in Fig. 3.4(c), all H atoms occupy T_z sites displaced from O_z sites in the same direction, labelled T_{zo}.

All structures in Table 3.II except for VH-7 and VH-8 have a pseudo-bcc crystal lattice in which H atoms only occupy T sites. VH-8 has a bct lattice with H atoms on O_z sites, and an electronic energy higher than that of VH-1 by 53.4 meV/f.u. As in the case of DVH-6, VH-8 becomes more stable than VH-1 when vibrational effects are included. Although no direct observation of the structure of VH has been reported, $VH_{0.90}$ is known to have a tetragonal structure with $c_0/a_0 \sim 1.13$ [24]. The only bct model in Table 3.II, VH-8, has a lattice constant ratio of $c_0/a_0 \sim 1.30$, which is not close to the experimental value. A similar c_0/a_0 ratio was known for VH from static DFT calculations [26]. The lack of agreement between theoretical and experimental results may be related to the difficulty of precise determination of H sites in monohydrides from neutron diffraction measurements.

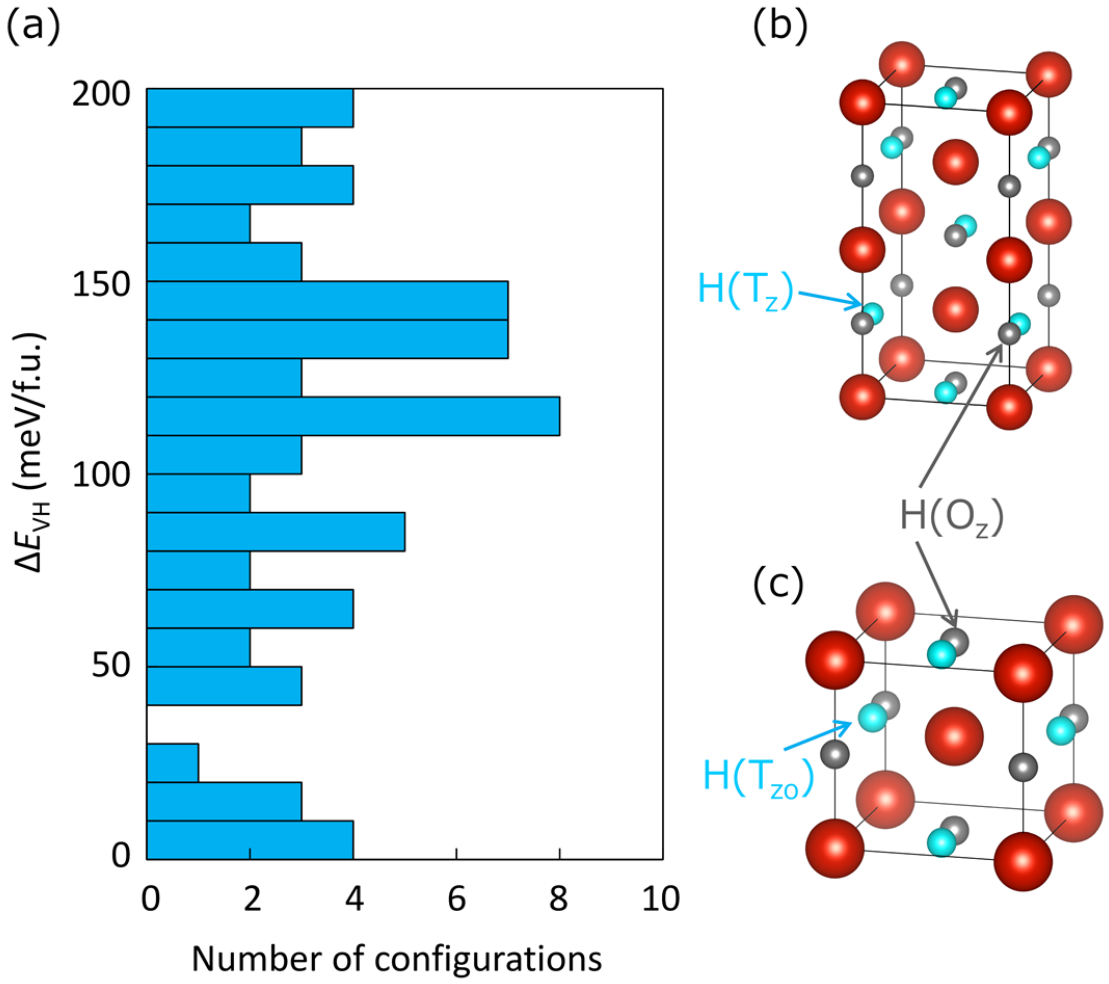

Fig. 3.4. (a) Histogram of electronic energies of configurations of VH measured from the lowest energy, ΔE_{VH}. (b), (c) Positions of H atoms in the most stable structure (VH-1) and second most stable structure (VH-2), respectively. H atoms on O_z sites are also shown as grey spheres.

TABLE 3.II. H sites, lattice type of V atoms, lattice constants, and electronic energies for 9 stable configurations of VH. VH-7 has a monoclinic-like cell with a monoclinic angle of $\gamma_0 = 86.0$. H site labels T_z, T_{zo}, and O_z correspond to particular (or ordered) configurations of H atoms in Fig. 3.4.

Configuration	H sites	Structure	a_0 (Å)	c_0 (Å)	c_0/a_0	ΔE_{VH} (meV/f.u.)
VH-1	T_z	pseudo-bcc	3.164	3.143	0.99	-
VH-2	T_{zo}	pseudo-bcc	3.173	3.154	0.99	2.6
VH-3	T_z	pseudo-bcc	3.156	3.160	1.00	3.8
VH-4	T_z	pseudo-bcc	3.149	3.165	1.01	11.6
VH-5	T_z	pseudo-bcc	3.159	3.149	1.00	18.5
VH-6	T_z	pseudo-bcc	3.156	3.175	1.01	20.4
VH-7	(T)	monoclinic	(3.314)	(2.792)	(0.84)	42.8
VH-8	O_z	bct	2.867	3.719	1.30	53.4
VH-9	T	pseudo-bcc	3.143 3.129	3.208	1.02 1.03	62.2

3.3.3. Ground states with vibrational contributions

In order to examine the effect of vibrational contributions on stabilities of different configurations, we calculated zero-point energies, E_{ZPE}, for V, $VH_{0.5}$, VH and VH_2 using first-principles phonon calculation methods. The structure models used for calculations were V, DVH-1, DVH-2, DVH-6, VH-1, VH-2, VH-8, and VH_2. In VH_2, all H atoms occupy all T sites in a fcc lattice. The plot of E_{ZPE} as a function of hydrogen/vanadium ratio in Fig. 3.5 shows that E_{ZPE} increases linearly as the amount of hydrogen increases, indicating that contributions of ZPE from H atoms are not negligible. E_{ZPE} of V and VH_2 are 33 meV/f.u. and 527 meV/f.u., respectively. The ZPE of hydrogen gas was estimated to be 270 meV by calculating the energy of an H_2 molecule in vacuum. These values are in good agreement with previous calculations [42]. The differences in E_{ZPE} between VH-1 and VH-2, and DVH-1 and DVH-2 are less than 2 meV/f.u. This indicates that the vibrational contributions from H atoms on T_z sites are similar regardless of the exact positions of the H atoms. The stability sequence of T-site configurations in Tables 3.I and 3.II is thus unlikely to be affected much by including lattice vibrations. On the other hand, the difference in E_{ZPE} between T-site and O-site structures is large. Values of E_{ZPE} of T-site structures are higher than those of O-site structures by 40 meV/f.u. for $VH_{0.5}$ and 70 meV/f.u. for VH. This indicates that E_{ZPE} values strongly depend on the coordination environment of H atoms. This trend is consistent with experimentally-derived magnitudes of ZPE contributions of T- and O-site hydrogen [43].

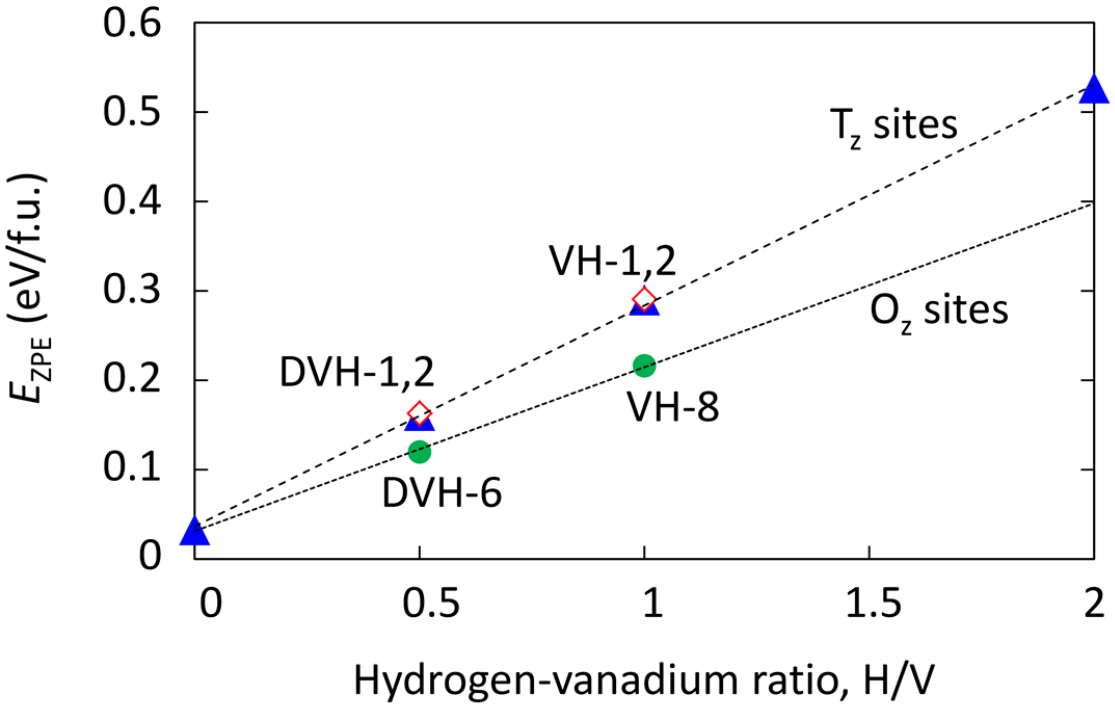

Fig. 3.5. Calculated zero-point energies, E_{ZPE}, for different configurations of H atoms as a function of H/V ratio.

Figure 3.6 shows plots of total free energies, ΔF_{tot}, obtained from the summation of electronic and vibrational free energies, as a function of temperature for $VH_{0.5}$ and VH. The zero of the energy axis was set at the lowest electronic energy for each composition. The plots show that O_z-site structures DVH-6 and VH-8 are the most stable over the temperature range 0 - 1000 K in contrast to when vibrational contributions are not included in which case T_z-site structures are most stable. For the other low-energy structures in Tables 3.I and 3.II, vibrational contributions were assumed to be the same as those for DVH-1 and VH-2, respectively. According to the first-principles calculations of the V-H system by Kim *et al.*, a T-site configuration is more favorable than an O-site configuration even after including ZPE [23]. Moreover, the models used in their calculations were small and only a limited number of configurations could be searched. Based on results for our larger supercell and wider configuration search, we find that DVH-6 with H on O_{z1} sites is more stable than O-site models with a smaller cell. These observations highlight the importance of searching configurations over a relatively wide phase space and including effects of lattice vibrations when assessing the relative stabilities of atomic configurations of V-based hydrides.

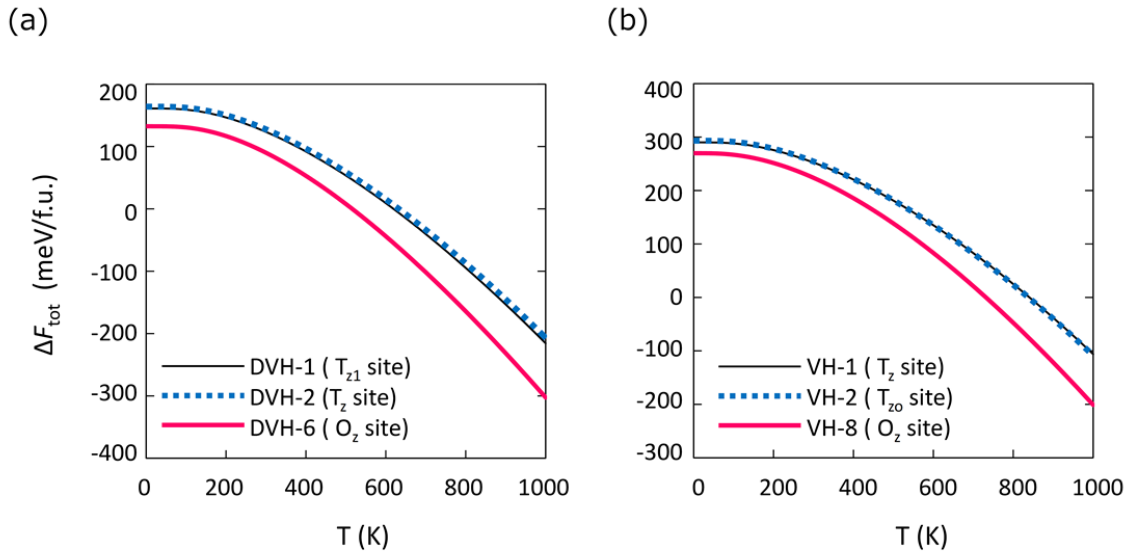

Fig. 3.6. Total free energies, ΔF_{tot}, of (a) $VH_{0.5}$ and (b) VH as a function of temperature. Energies are taken relative to the lowest electronic energy of DVH-1 and VH-1 in (a) and (b), respectively.

3.3.4. Equilibrium hydrogen pressures in the V-H system

In Fig. 3.7, calculated $P_{H_2}^{eq}$ values for the two hydrogenation reactions of the V-H system (Eq. (1) and (2)) are plotted as a function of inverse temperature. Lines indicate calculated $P_{H_2}^{eq}$ values while the open symbols show the experimentally measured plateau pressures [4,5]. The lower and higher equilibrium pressures are shown as blue and red lines, respectively. The most stable structure of $VH_{0.5}$, DVH-6, was used to calculate the lower $P_{H_2}^{eq}$. To calculate the higher $P_{H_2}^{eq}$, both the lowest energy O- and T-site structures were used. The theoretical estimates of $P_{H_2}^{eq}$ reproduce the experimental values for the lower plateau particularly well.

Calculated $P_{H_2}^{eq}$ values for the hydrogenation reaction Eq. (2) using the VH-8 structure with H on O_z sites are larger than the experimental values by an order of magnitude. The reason for this difference may be the assumption that the higher $P_{H_2}^{eq}$ corresponds to the reaction from VH to VH_2. In Ref. [5], the reaction corresponding to the plateau region was assumed to be the conversion of $VH_{0.95}$ to VH_2. In addition, some of the H atoms in VH were suggested to be on T sites, while in VH-8, H atoms only occupy O_z sites. To evaluate the effect of different site occupancies on $P_{H_2}^{eq}$, values for model VH-1, in which H atom occupies T_z sites, reaching to form VH_2 were calculated. The results in Fig. 3.7 show that the values of $P_{H_2}^{eq}$ are reduced by an order of magnitude compared with VH-8. The good agreement between the results of VH-1 model, which is higher in energy than VH-8, and experimental values suggests that H atoms in VH_x ($0.9 < x < 1$) occupy a mixture of O and T sites, at elevated temperatures.

The procedure described in this paper can be extended to the study of equilibrium hydrogen pressures in more complex systems such as V-based alloys like Ti-V and Ti-V-Mn. One of the difficulties of this method, however, is that it is not easy to model disordered solid solutions with the small model sizes typically used in first-principles calculations. Since vibrational

contributions have a non-negligible impact on the calculated partial pressures, it is also important to use some approximations to simplify the handling of vibrational contributions. This methodology is expected to facilitate systematic and reliable investigation of $P_{H_2}^{eq}$ values for a wide range of V-based alloys.

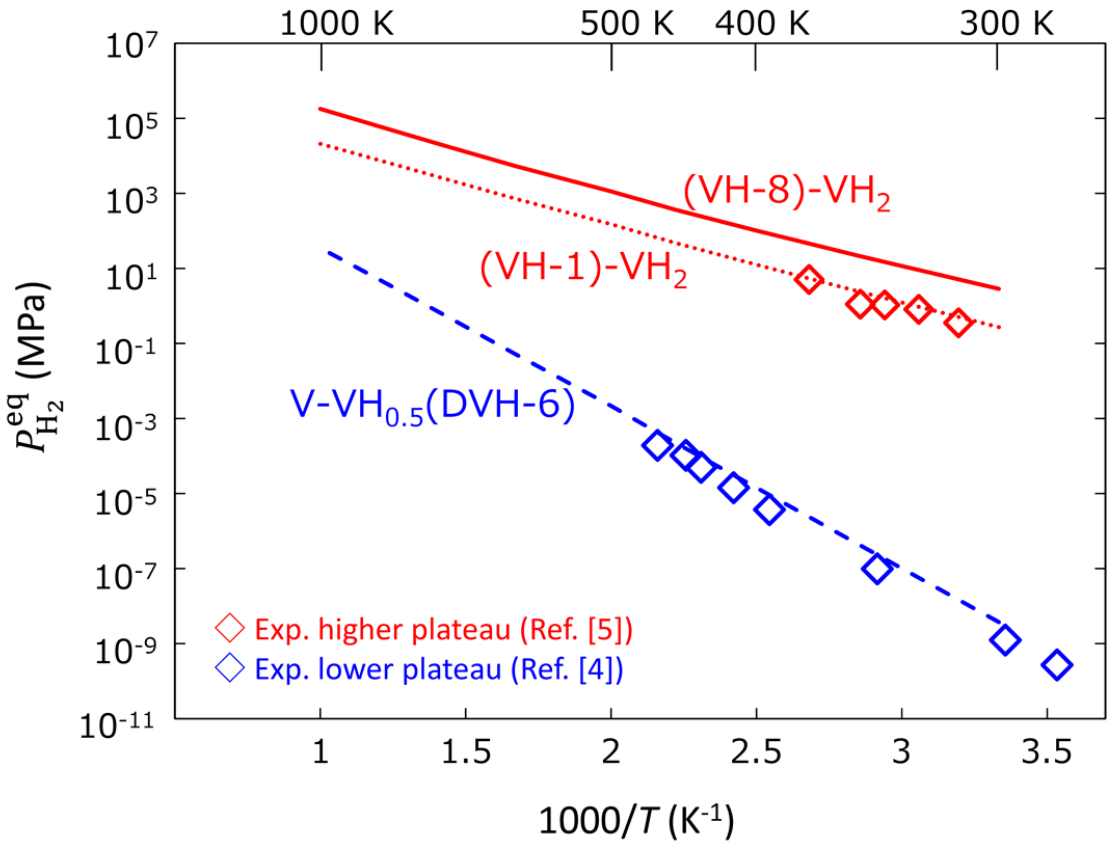

Fig. 3.7. Temperature dependence of equilibrium hydrogen pressures, $P_{H_2}^{eq}$, for V-VH$_{0.5}$ and VH-VH$_2$ reactions, corresponding to the lower and higher pressures, respectively. Lines indicate calculated values and open symbols indicate experimental values.

3.4. Conclusions

Equilibrium hydrogen pressures, $P_{H_2}^{eq}$, in the V-H system were estimated using first-principles calculations by first searching for low-energy structures among candidate configurations of intermediate hydrides $VH_{0.5}$ and VH excluding vibrational contributions. The lowest-energy configurations were found to have H atoms distributed over T_z sites for both H contents. When vibrational contributions were included, the ground-state configurations were bct-like structures with hydrogen atoms on O_z sites. Zero-point energy, ZPE, has a particularly strong effect on the ground-state configuration. Theoretical $P_{H_2}^{eq}$ values calculated using these models reproduce experimental values well, although the results for high H contents suggest a mixture of O and T sites are occupied. Our results demonstrate how equilibrium hydrogen pressures of V-based compounds can be estimated from DFT calculations by combining configurational searches with inclusion of lattice vibrations, which should provide useful insights into how to optimize the hydrogenation behavior of V-based compounds.

References

[1] E. Akiba, H. Iba, Hydrogen absorption by Laves phase related BCC solid solution, Intermetallics 6 (1998) 461–470.

[2] H. Kim, K. Sakaki, H. Ogawa, Y. Nakamura, J. Nakamura, E. Akiba, A. Machida, T. Watanuki, T. Proffen, Origin of degradation in the reversible hydrogen storage capacity of $V_{1-x}Ti_x$ alloys from the atomic pair distribution function analysis, J. Phys. Chem. C 117 (2013) 26543–26550.

[3] H. Kim, K. Sakaki, I. Saita, H. Enoki, K. Noguchi, A. Machida, T. Watanuki, Y. Nakamura, Reduction and unusual recovery in the reversible hydrogen storage capacity of $V_{1-x}Ti_x$ during hydrogen cycling, Int. J. Hydrogen Energy 39 (2014) 10546–10551.

[4] R. Griffiths, J.A. Pryde, A. Righini-Brand, Phase diagram and thermodynamic data for the hydrogen/vanadium system, J. Chem. Soc., Faraday Trans. 1 68 (1972) 2344–2349.

[5] J.J. Reilly, R.H. Wiswall, The higher hydrides of vanadium and niobium, Inorg. Chem. 9 (1970) 1678–1682.

[6] Y. Nakamura, E. Akiba, Hydriding properties and crystal structure of NaCl-type mono-hydrides formed from Ti–V–Mn BCC solid solutions, J. Alloys Compd. 345 (2002) 175–182.

[7] Y. Nakamura, J. Nakamura, K. Sakaki, K. Asano, E. Akiba, Hydrogenation properties of Ti–V–Mn alloys with a BCC structure containing high and low oxygen concentrations, J. Alloys Compd. 509 (2011) 1841–1847.

[8] K. Asano, S. Hayashi, Y. Nakamura, Enhancement of hydrogen diffusion in the body-centered tetragonal monohydride phase of the V–H system by substitutional Al studied by proton nuclear magnetic resonance, Acta Mater. 83 (2015) 479–487.

[9] H. Yukawa, D. Yamashita, S. Ito, M. Morinaga, S. Yamaguchi, Alloying effects on the phase stability of hydrides formed in vanadium alloys, Mater. Trans. 43 (2002) 2757–2762.

[10] T. Matumura, H. Yukawa, M. Morinaga, Alloying effects on the electronic structures of VH_2 and V_2H, J. Alloys Compd. 284 (1999) 82–88.

[11] S. Ukita, H. Ohtani, M. Hasebe, Thermodynamic analysis of the V–H binary phase diagram, Mater. Trans. 49 (2008) 2528–2533.

[12] K.-H. Kim, J.-H. Shim, B.-J. Lee, Effect of alloying elements (Al, Co, Fe, Ni) on the solubility of

hydrogen in vanadium: A thermodynamic calculation, Int. J. Hydrogen Energy 37 (2012) 7836–7847.

[13] C. Li, P. Peng, D.W. Zhou, L. Wan, Research progress in $LiBH_4$ for hydrogen storage: A review, Int. J. Hydrogen Energy 36 (2011) 14512–14526.

[14] C. Wolverton, D.J. Siegel, A.R. Akbarzadeh, V. Ozoliņš, Discovery of novel hydrogen storage materials: an atomic scale computational approach, J. Phys. Condens. Matter 20 (2008) 64228.

[15] Y. Yang, P. Zhang, Hydriding and dehydriding energies of PuH_x from ab initio calculations, Phys. Lett. A 379 (2015) 1649–1653.

[16] T.B. Massalski, Binary Alloy Phase Diagrams, 2nd ed., ASM International, Ohio, 1990.

[17] Y. Fukai, The Metal-Hydrogen System, Springer-Verlag, Berlin/Heidelberg, 2005.

[18] Y. Noda, K. Masumoto, S. Koike, T. Suzuki, S. Sato, X-ray crystallographic study of tetragonal and monoclinic β_1 -V_2H, Acta Cryst. B 42 (1986) 529–533.

[19] H. Asano, L. Abe, M. Hirabayashi, A calorimetric study of the phase transformation of vanadium hydrides $VH_{0.06}$–$VH_{0.77}$, Acta Metall. 24 (1976) 95–99.

[20] H. Asano, Y. Abe, M. Hirabayashi, A neutron diffraction study of V_2H, J. Phys. Soc. Jpn. 41 (1976) 974–976.

[21] Y. Noda, T. Kajitani, M. Hirabayashi, S. Sato, X-ray structure determination of divanadium hydride, β_1-V_2H, and divanadium deuteride, β-V_2D, Acta Cryst. C 41 (1985) 1566–1571.

[22] K. Momma, F. Izumi, VESTA 3 for three-dimensional visualization of crystal, volumetric and morphology data, J. Appl. Cryst. 44 (2011) 1272–1276.

[23] J. Kim, J.-H. Yoo, S.-W. Cho, Energy and diffusion of hydrogen atoms in titanium substituted vanadium hydrides from ab initio calculations, Mater. Chem. Phys. 148 (2014) 533–539.

[24] A.J. Maeland, Investigation of the vanadium-hydrogen system by X-ray diffraction techniques, J. Phys. Chem. 68 (1964) 2197–2200.

[25] T. Kajitani, M. Hirabayashi, Neutron diffraction study of β_1-V_2H and β-V_2D, Z. Phys. Chem. NF 145 (1985) 27–42.

[26] K. Miwa, H. Ohno, Molecular dynamics study on β-phase vanadium monohydride with machine learning potential, Phys. Rev. B 94 (2016) 184109.

[27] E. Yagi, T. Hayashi, T. Yoshida, S. Koike, N. Higami, K. Hirabayashi, A. Takebayashi, H. Matsuba,

K. Ogiwara, Lattice location and density distribution of hydrogen in β_1-V_2H, J. Phys. Soc. Jpn. 81 (2012) 44602.

[28] A. Seko, Y. Koyama, I. Tanaka, Cluster expansion method for multicomponent systems based on optimal selection of structures for density-functional theory calculations, Phys. Rev. B 80 (2009) 165122.

[29] B.K. Rao, P. Jena, Switendick criterion for stable hydrides, Phys. Rev. B 31 (1985) 6726–6730.

[30] A.C. Switendick, Band structure calculations for metal hydrogen systems, Z. Phys. Chem. NF 117 (1979) 89–112.

[31] P.E. Blöchl, Projector augmented-wave method, Phys. Rev. B 50 (1994) 17953–17979.

[32] G. Kresse, D. Joubert, From ultrasoft pseudopotentials to the projector augmented-wave method, Phys. Rev. B 59 (1999) 1758–1775.

[33] J.P. Perdew, K. Burke, M. Ernzerhof, Generalized gradient approximation ade simple, Phys. Rev. Lett. 77 (1996) 3865–3868.

[34] J.P. Perdew, J. Chevary, S. Vosko, K. Jackson, M. Pederson, D. Singh, C. Fiolhais, Erratum: Atoms, molecules, solids, and surfaces: Applications of the generalized gradient approximation for exchange and correlation, Phys. Rev. B 48 (1993) 4978–4978.

[35] G. Kresse, J. Hafner, Ab initio molecular dynamics for liquid metals, Phys. Rev. B 47 (1993) 558–561.

[36] G. Kresse, J. Furthmüller, Efficient iterative schemes for ab initio total-energy calculations using a plane-wave basis set, Phys. Rev. B 54 (1996) 11169–11186.

[37] H.J. Monkhorst, J.D. Pack, Special points for Brillouin-zone integrations, Phys. Rev. B 13 (1976) 5188–5192.

[38] A. Togo, F. Oba, I. Tanaka, First-principles calculations of the ferroelastic transition between rutile-type and $CaCl_2$-type SiO_2 at high pressures, Phys. Rev. B 78 (2008) 134106.

[39] A. Togo, I. Tanaka, First principles phonon calculations in materials science, Scripta Mater. 108 (2015) 1–5.

[40] M.W. Chase Jr., NIST-JANAF Thermochemical Tables, 4th ed., The American Chemical Society and the American Institute of Physics for the National Institute of Standards and Technology, New York,

1998.

[41] K. Kamazawa, M. Aoki, T. Noritake, K. Miwa, J. Sugiyama, S. Towata, M. Ishikiriyama, S.K. Callear, M.O. Jones, W.I.F. David, In-operando neutron diffraction studies of transition metal hydrogen storage materials, Adv. Energy Mater. 3 (2013) 39–42.

[42] K. Miwa, A. Fukumoto, First-principles study on 3d transition-metal dihydrides, Phys. Rev. B 65 (2002) 155114.

[43] G. Sicking, Isotope effects in metal-hydrogen systems, J. Less-Common Met. 101 (1984) 169–190.

Chapter 4

Equilibrium hydrogen pressures in the Ti-V-Mn systems from first-principles calculations

4.1. Introduction

Fuel cell vehicles (FCVs) are being developed as new generation environmentally friendly vehicles, where fuel cells produce electricity by electrochemically combining hydrogen fuel with atmospheric oxygen. As a hydrogen source, 70 MPa high-pressure hydrogen tanks are mounted on recent commercial FCVs. There are still difficulties in handling and transporting high-pressure hydrogen gas, being the obstacles of the wide use of FCVs. Many researchers have investigated hydrogen storage alloys for use in FCVs [1,2], because these hydrides occupy far less volumes than compressed hydrogen gas, and most hydrogen storage materials absorb hydrogen gas at lower hydrogen pressures. Hydrogen storage materials for FCVs have to satisfy many requirements: at least 3 mass% hydrogen storage capacity under near-standard conditions, favorable initial kinetics, cyclic stabilities of absorption and desorption, and economical production costs.

Vanadium has been considered to be one of the promising materials, because its storage capacity reaches at most 4 mass% with fine cyclic stability [3–5]. In spite of these good properties, there are basically two obstacles in application of V to FCVs. One problem appears in extremely low equilibrium hydrogen pressures, $P_{\mathrm{H_2}}^{\mathrm{eq}}$, of dehydrogenation from monohydride to metal [6,7]. Griffiths *et al.* reported the value of the first-plateau at 300 K was about 0.1 Pa. The other is the high cost of pure V which hinders the practical use of V in FCVs. Because V is alloyed with various metals, hydrogenation of V-based alloys has also been investigated. Among them, Ti and V form bcc

solid solution alloys in a broad range of V content [8]. Properties such as $P_{H_2}^{eq}$ and hydrogenation temperature are known to strongly depend on compositions and additional elements [9–16], and Ti-V-Mn-based alloys are regarded as ones of the promising alloys to apply FCV technologies. In this study, we mainly focus on $Ti_{1.0}V_{1.1}Mn_{0.9}$ alloy, whose structures and hydrogenation properties have been investigated in detail [17–24].

From experimental studies by Nakamura *et al.*, $Ti_{1.0}V_{1.1}Mn_{0.9}$ alloy is known to form disordered bcc solid solution and to show clear two plateau regions in the pressure-composition (PC) isotherm. As hydrogenation proceeds, bcc crystal lattice of metal atoms expands along the *c*-axis, and changes into CaF_2-type (fluorite) dihydride, $Ti_{1.0}V_{1.1}Mn_{0.9}H_6$, via interstitial face-centered-tetragonal (fct) monohydride, $Ti_{1.0}V_{1.1}Mn_{0.9}H_3$. Structures of each compound are depicted in Fig. 4.1 as fcc- or fct-type cells. From the different point of view, the structures are also regarded as deformed-bct-type cells depicted in Fig. 4.1(a) by green lines. The characteristic point of this material is that H sites in the monohydride have been determined by neutron diffraction measurements as shown in Fig. 4.1(b). H atoms in the monohydride occupy interstitial octahedral (O) sites of fct crystal lattice, which equal to O_z sites of the corresponding bct lattice. H atoms in the dihydrides occupy interstitial tetrahedral (T) sites. Therefore, the monohydride and the dihydride have NaCl-type and CaF_2-type structures, respectively. Storage capacities of $Ti_{1.0}V_{1.1}Mn_{0.9}$ alloy reach more than 2 mass%, and efforts to develop capacities and to optimize plateau pressures have been performed. Despite of many experimental efforts, how properties change depending on compositions is still unclear. Theoretical evaluations are of help in understanding and controlling the hydrogenation behavior of Ti-V-Mn-based compounds.

The purpose of this study is to investigate the effects of composition on $P_{H_2}^{eq}$ in Ti-V-Mn-based systems, mainly focusing on $Ti_{1.0}V_{1.1}Mn_{0.9}$ alloy, using first-principles calculations. Here we employed the procedure introduced in Chapter 3, with additional techniques to treat

disordered solid solutions. Because the structure of the monohydride is determined, low-energy structures were no need to be searched in the system. Note that in this chapter, composition of alloys are indicated in the style containing more than one formula unit for descriptive convenience, such as $Ti_{1.0}V_{1.1}Mn_{0.9}$ of three f.u.. Energy in the unit of eV/f.u. is obtained by dividing calculated energy by the number of metal atoms in the computational cell, as same as the other chapter.

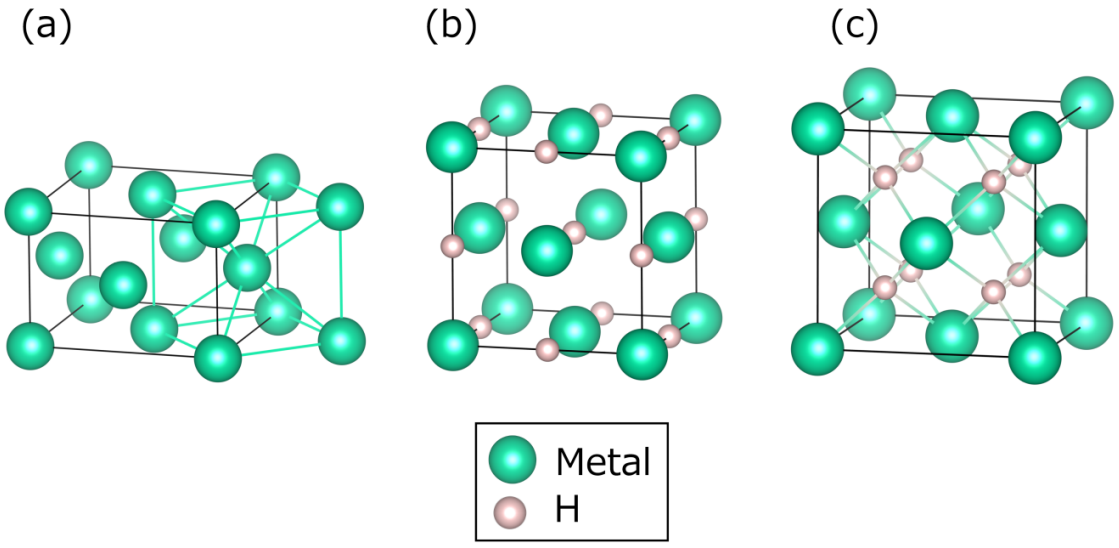

Fig. 4.1. Crystal structures and H sites of (a) $Ti_{1.0}V_{1.1}Mn_{0.9}$ alloy, (b) $Ti_{1.0}V_{1.1}Mn_{0.9}H_3$, and (c) $Ti_{1.0}V_{1.1}Mn_{0.9}H_6$, depicted as fct-type cells.

4.2. Computational methodology

4.2.1. Estimation of equilibrium hydrogen pressures

Equilibrium hydrogen pressures of hydrogenation reactions of Ti-V-Mn-based alloys were estimated thermochemically using Gibbs free energies under equilibrium conditions. The formulation employed here was basically the procedures introduced in Chapter 3, Sec. 3.2. We considered the following two hydrogenation reactions of the $Ti_{1.0}V_{1.1}Mn_{0.9}$-H system:

$$1/3(\mathrm{Ti_{1.0}V_{1.1}Mn_{0.9}}) + 1/2\mathrm{H_2} \Leftrightarrow 1/3(\mathrm{Ti_{1.0}V_{1.1}Mn_{0.9}H_3}), \quad (1)$$

$$1/3(\mathrm{Ti_{1.0}V_{1.1}Mn_{0.9}H_3}) + 1/2\mathrm{H_2} \Leftrightarrow 1/3(\mathrm{Ti_{1.0}V_{1.1}Mn_{0.9}H_6}). \quad (2)$$

$P_{H_2}^{\mathrm{eq}}$ is obtained from the relation,

$$k_B T \ln \frac{P_{\mathrm{H_2}}^{\mathrm{eq}}}{P_{\mathrm{H_2}}^{\mathrm{o}}} = 2(G_{\alpha'} - G_{\alpha}) - \left(H_{\mathrm{H_2}}^{\mathrm{o}}(0\ \mathrm{K}) + \Delta H_{\mathrm{H_2}}^{\mathrm{o}}(T) - TS_{\mathrm{H_2}}^{\mathrm{o}}(T)\right), \quad (3)$$

where $P_{\mathrm{H_2}}^{o}$ indicates the standard hydrogen pressure. $G_{\alpha'}$ and G_{α} indicate Gibbs free energies of Ti-V-Mn-based compounds after and before hydrogenation reaction, respectively. Enthalpies (*H*) and entropy (*S*) at $P_{\mathrm{H_2}}^{\mathrm{o}}$ are introduced to express contributions of hydrogen gas. These free energies are decomposed into contributions from electronic energy and vibrational free energy. The third term in Eq. (3) indicates the suite of thermodynamic quantities of hydrogen gas, and these values were extracted from NIST-JANAF database [25]. Since zero-point energy (ZPE) of hydrogen gas is not included in these values, the value of ZPE was estimated by DFT calculations of H_2 molecules.

Electronic energy calculations were performed in the framework of DFT using the projector augmented-wave (PAW) method [26,27] and the generalized gradient approximation (GGA) [28,29] as implemented in the VASP code [30,31]. In order to take into the effects of magnetism of Mn, spin-polarized calculations were implemented. A cut-off energy for the plane-wave basis set was 400 eV for all calculations. Brillouin-zone integration was carried out

based on the Monkhorst-Pack scheme [32] and *k*-point spacing was set at less than 0.15 $Å^{-1}$. In addition to atomic positions, both cell shape and volume were fully relaxed until the residual forces became less than 0.02 $eVÅ^{-1}$.

To include vibrational free energies including zero-point energies (ZPE), we performed phonon calculations based on the finite-difference method as implemented in the Phonopy code [33]. In the phonon calculations, supercells of the unit cell of target compounds with lattice constants longer than 9 Å were constructed. Vibrational free energies were evaluated from calculated phonon. In this step, equilibrium structures were optimized until the residual forces became less than 0.0002 $eVÅ^{-1}$. Atomic displacement of 0.01 Å was used to construct the dynamical matrix.

4.2.2. Special quasirandom structure (SQS)

In order to model disordered configuration of metal atoms in Ti-V-Mn-based alloys and hydrides, special quasirandom structure (SQS) models developed by Zunger *et al.* [34,35] are introduced. The SQSs are specially designed periodic cells, which are small enough to implement DFT calculations, to imitate the average pair correlation functions of completely random models. The correlation function of a cluster α, which indicates a figure composed of a combination of interacting atoms on lattice points, is defined as

$$\varphi_\alpha = \frac{1}{N_\alpha} \sum_{i,j,\cdots \in \alpha} \sigma_i \sigma_j \cdots, \tag{4}$$

where N_α means the number of symmetrically equivalent clusters of cluster type α. σ_i is an Ising-like configurational variable for a particular lattice site *i*. In the case of a binary alloy, σ_i customary takes a value of +1 or -1 depending on the atom species, +1, 0, or -1 in the case of a ternary alloy, +2, +1, -1, or -2 in the case of a quaternary alloy. The average pair correlation functions of a completely random model, $\overline{\Pi}^2$, can be expressed in analytical forms. For a ternary

alloy A-B-C with compositions x_{A}, x_{B}, and x_{C}, $\overline{\Pi}^2$ is expressed as

$$\overline{\Pi}^2[n,m] = \left(\sqrt{\frac{3}{2}}(x_A - x_C)\right)^n \left(\sqrt{\frac{1}{2}}(1 - 3x_B)\right)^m \tag{5}$$

where *n* and *m* take a value of 1 or 2. Contrary to the binary system, plural correlation functions exist for one cluster in multicomponent system. As indicated in Eq. (5), four types of average pair correlation functions for a pair cluster can be obtained in a ternary system with combinations of values of *n* and *m*. SQS models are constructed to reproduce values of pair correlation functions to those of a completely random model as possible. Formulations of $\overline{\Pi}^2$ of binary and quaternary systems are available in Appendix C.

In this study, the CLUPAN code [36] was used to generate SQS models. Since the SQS model with exact composition of $Ti_{1.0}V_{1.1}Mn_{0.9}$ requires more than hundreds of metal atoms in a cell, it is not practical to handle such a big model in the DFT scheme. Therefore, we constructed SQS models with metal atoms less than 108, whose compositions were close but not exactly the same with the compositions of target materials. Pair correlation functions for up to the fourth pairs of the fcc sublattice were taken into account to reproduce values of $\overline{\Pi}^2$. At least three SQS models were produced for one target composition in order to compare effects from metal-atom configurations. Examples of computational models of $Ti_{1.0}V_{1.1}Mn_{0.9}$-H system constructed by the SQS technique are depicted in Fig. 4.2. Each model contains 48 metal atoms and is represented as the 2 × 2 × 3 supercell in the unit of an fct conventional cell.

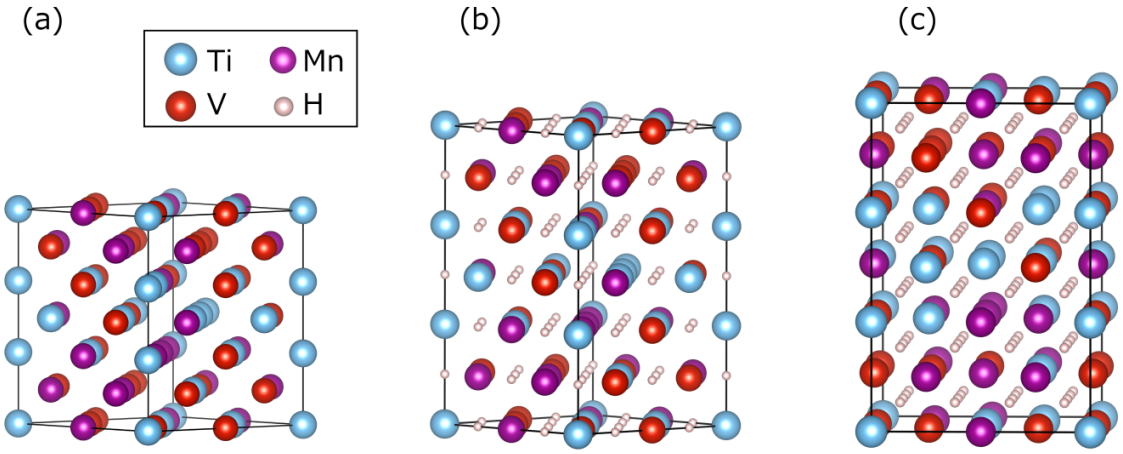

Fig. 4.2. Computational SQS models containing 48 metal atoms of (a) $Ti_{1.0}V_{1.1}Mn_{0.9}$ alloy, (b) $Ti_{1.0}V_{1.1}Mn_{0.9}H_3$, and (c) $Ti_{1.0}V_{1.1}Mn_{0.9}H_6$.

4.3. Results and discussion

4.3.1. Comparison of lattice constants

Calculated lattice constants obtained with geometry optimizations of SQS models of $Ti_{1.0}V_{1.1}Mn_{0.9}$ alloys and hydrides expressed in terms of the fcc-type conventional unit cell are compared with experimental values [20] as listed in Table 4.I. In order to decrease an error caused from differences in configurations of metal atoms, at least three SQS models were generated for each compound, and calculated values were averaged over these SQS models. As shown in the table, calculated lattice constants and a crystal shape of the alloy are in good agreement with experimental data. Although the values of hydrogen/metal ratios in a compound denoted as "H/M" are not the same, the calculated lattice constant takes a close value with experimental data in dihydrides. In the case of the monohydride, the difference of H/M values is smaller than that of dihydrides. The ratio of lattice constants, however, is 0.96 for calculated models, while measurements claim that it is about 0.92. A *c*/*a* ratio of a hydride with H/M of about 1 is suggested to be affected by H sites in V-based alloys [37]. Although H atoms in $Ti_{1.0}V_{1.1}Mn_{0.9}H_3$ are claimed to occupy O sites in a fcc lattice from neutron diffraction measurements, there still remains a possibility of H atoms partially locate not only O sites but also surrounding T sites as suggested in V or Ti-V-Cr-Mo systems [38,39]. T-site occupation of H atoms results in decrease of a *c*/*a* ratio. We compared electronic energies of $Ti_{1.0}V_{1.1}Mn_{0.9}H_3$ with O-site and T-site occupation of H atoms, revealed that T-site occupation models have higher energies than O-site occupation models by more than 50 meV/f.u.. Therefore, in order to examine this effect, further experimental investigations on H sites in $Ti_{1.0}V_{1.1}Mn_{0.9}H_3$ are required.

SQS models reproduce the lattice constants of disordered $Ti_{1.0}V_{1.1}Mn_{0.9}$ alloys and hydrides within the error of three percent from experimental values. We, therefore, employ the SQS methodology to deal with $Ti_{1.0}V_{1.1}Mn_{0.9}$-based compounds in the following discussions.

Table 4.I. Structural parameters of $Ti_{1.0}V_{1.1}Mn_{0.9}$ alloy and hydrides. "H/M" indicates the hydrogen/metal ratio in a compound. Lattice constants are expressed in terms of the fcc-type conventional unit cell.

Compound	H/M	*a* (Å)	*c* (Å)	*c*/*a*	
Alloy	0	4.254	2.985	0.70	Calc.
	0	4.297	3.039	0.71	Ref. [20]
Monohydride	1	4.020	3.863	0.96	Calc.
	0.90	4.143	3.793	0.92	Ref. [20]
Dihydride	2	4.247	-	1.00	Calc.
	1.73	4.356		1.00	Ref. [20]

4.3.2. Estimation of ZPE in the Ti-V-Mn-H system

As described in Chapter 3, contributions of lattice vibrations play an important role in quantitative evaluation of $P_{H_2}^{eq}$. E_{ZPE} were estimated using first-principles phonon calculations in the V-H system in Chapter 3, Sec. 3.3.3. On the other hand, it is more intensive tasks to calculate E_{ZPE} in the Ti-V-Mn-H system, because distributions of metal atoms on the sublattices are claimed to be disordered, so that SQS models are employed to represent models of Ti-V-Mn compounds. So, in order to practically evaluate contributions of lattice vibrations in the Ti-V-Mn-H system, we introduced approximations as follows.

We calculated E_{ZPE} of $Ti_{1.0}V_{1.1}Mn_{0.9}H_6$ using the 2 × 2 × 3 SQS supercell in the unit of a CaF_2-type conventional cell and ground-state metal Mn with the space group $I\bar{4}3m$. Figure 4.3 shows E_{ZPE} as a function of hydrogen/metal ratio for Mn, Ti-V-Mn-H, and V-H systems. E_{ZPE} of metal Mn and metal V are 41 meV/f.u. and 33 meV/f.u., respectively. From the previous DFT study on the Ti-H and the V-H systems, E_{ZPE} of hcp-Ti is given by the value of about 30 meV/f.u. [40]. Because differences in these values are relatively small, we consider E_{ZPE} of metals can be represented by that of metal V. E_{ZPE} of $Ti_{1.0}V_{1.1}Mn_{0.9}H_6$ is 496 meV/f.u., which is lower than that of VH_2 by 20 meV/f.u.. This value is not large compared to the absolute values of E_{ZPE}. From these results, we consider the hydrogen/metal ratio has much effect on E_{ZPE} than which type of metal atoms locates on the metal sublattices, i.e., Ti, V, or Mn. As discussed in Chapter 3, E_{ZPE} increases linearly as the ratio of hydrogen increases in the V-H system. Therefore, we use values of contributions of lattice vibrations of metal V and VH, instead of those of $Ti_{1.0}V_{1.1}Mn_{0.9}$ alloy and $Ti_{1.0}V_{1.1}Mn_{0.9}H_3$.

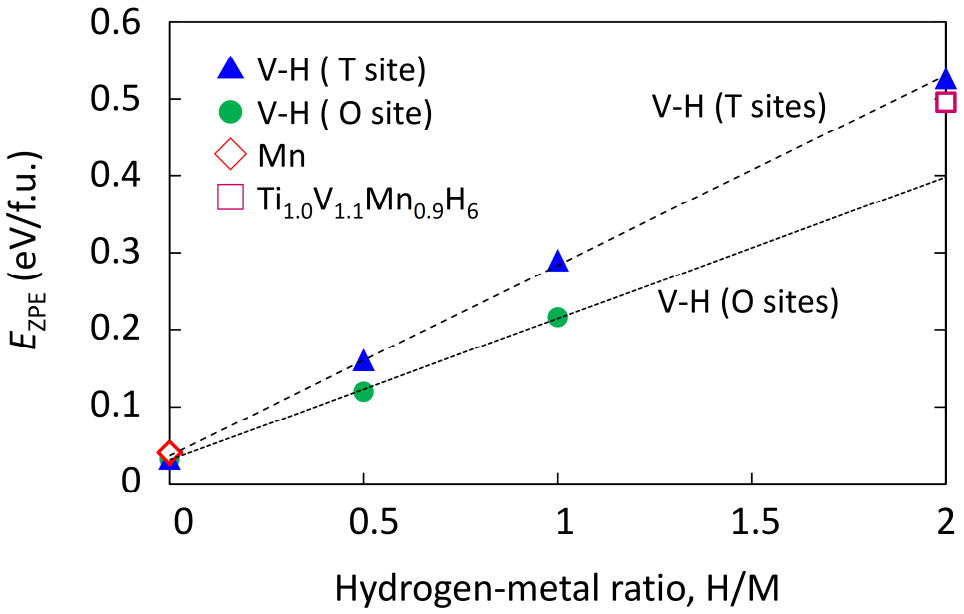

Fig. 4.3. Calculated zero-point energies, E_{ZPE}, for different configurations of H atoms as a function of hydrogen/metal ratio.

4.3.3. Equilibrium hydrogen pressures in the $Ti_{1.0}V_{1.1}Mn_{0.9}$ system

In Fig. 4.4, Calculated $P_{H_2}^{eq}$ of the two hydrogenation reactions of the $Ti_{1.0}V_{1.1}Mn_{0.9}$-H system were depicted as a function of inverse of temperature. Filled symbols indicate calculated $P_{H_2}^{eq}$ values while open symbols show experimentally observed plateau pressures [20]. The lower (first) and the higher (second) plateau pressures are indicated by blue and red plots, respectively. Two open plots depicted at the same temperatures indicate $P_{H_2}^{eq}$ of absorption process (higher one) and desorption process (lower one). In general, the plateau pressures of desorption process are regarded to be better indicator than those of absorption process, because changes in volumes are little during desorption. In this system, however, desorption plateaus are tend to be sloped and vague, so we used $P_{H_2}^{eq}$ of both process as references. In comparison with experimental data, theoretically estimated $P_{H_2}^{eq}$ reproduces the experimental values with difference by about an order of magnitude in both plateaus. Therefore, we conclude that the calculated $P_{H_2}^{eq}$ reproduce the tendencies of those obtained from experiments, in spite of approximations employed to evaluate contributions of lattice vibrations.

As an extension to this estimation, we also calculated $P_{H_2}^{eq}$ of the hydrogenation reactions of other Ti-V-Mn-H systems: $Ti_{0.8}V_{1.2}Mn_{1.0}$-H, $Ti_{1.0}V_{1.0}Mn_{1.0}$-H, and $Ti_{1.1}V_{1.1}Mn_{0.8}$-H. From the experimental report, structures of these monohydrides are known to be the fct lattice with O-sites occupation of H atoms [19]. SQS models were generated for each compound, and contributions of lattice vibrations were included by using those of V and VH for alloys and monohydrides, and $Ti_{1.0}V_{1.1}Mn_{0.9}H_6$ for dihydrides. The calculated $P_{H_2}^{eq}$ of those compounds will be discussed in the next section.

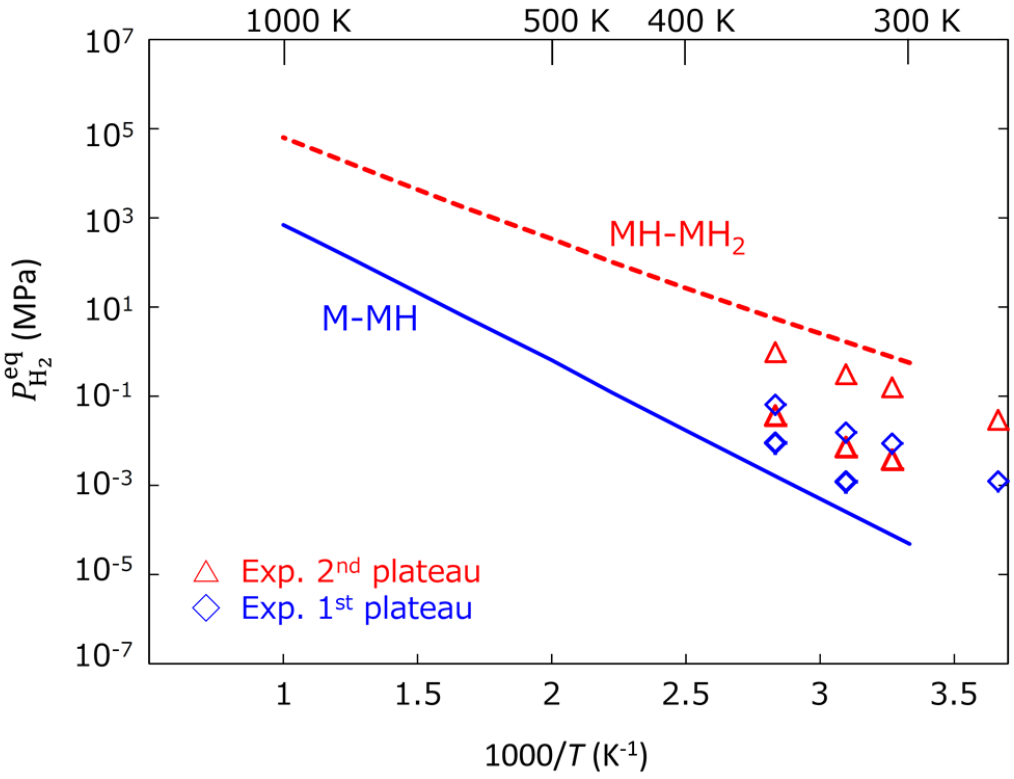

Fig. 4.4. Temperature dependence of equilibrium hydrogen pressures, $P_{H_2}^{eq}$, for M-MH and MH-MH$_2$ reactions of the $Ti_{1.0}V_{1.1}Mn_{0.9}$-H system, compared with experimental values.

4.3.4. Equilibrium hydrogen pressures in the Ga-doped $Ti_{1.0}V_{1.1}Mn_{0.9}$ systems compared with the Ti-V-Mn systems

For the purpose of decreasing production cost of V-based alloys, adding Al to Ti-V-based alloys has been attracting interest. The effects of Al-substitution on crystal structures and hydrogenation were investigated for materials such as metal V [37], Ti-V [41], and Ti-V-Cr alloys [42,43], and revealed that Al-doping has strong effects on properties of Ti-V-based alloys. Asano *et al.* suggests that Al-substitution in metal V increases $P_{H_2}^{eq}$, destabilizes hydrides, and changes the lattice of $VH_{0.5}$ from bct to bcc structure by shifting H atoms around Al from O_z sites to T sites [37]. In general, increasing lattice constants of Ti-V-based alloys leads a decrease of $P_{H_2}^{eq}$. In the case of Al-substitution, however, the opposite results were observed [41–43]. Yoo *et al.* proposed this originates from the difference of types of bonding between metal atoms and H atoms [42]: transition metals in Ti-V- based alloys usually make metallic bonds with H atoms, while an Al atom tends to bind covalently with H atoms.

In order to evaluate the effect of doping of other metal element to $Ti_{1.0}V_{1.1}Mn_{0.9}$, we focused on Ga-doping $Ti_{1.0}V_{1.1}Mn_{0.9}$ in this study, since Ga is the same family element of Al. Because there are three candidate elements for substitution in $Ti_{1.0}V_{1.1}Mn_{0.9}$, SQS models containing 48 metal atoms were generated for three compounds, namely $Ti_{0.9}V_{1.1}Mn_{0.9}Ga_{0.1}$, $Ti_{1.0}V_{1.0}Mn_{0.9}Ga_{0.1}$ and $Ti_{1.0}V_{1.1}Mn_{0.8}Ga_{0.1}$. Although these alloys and compounds have not synthesized in experiments yet, we assumed the structures were the same as those of $Ti_{1.0}V_{1.1}Mn_{0.9}$, because dopant Ga was small in amount. The structures of generated SQS models are shown in Fig. 4.5. $P_{H_2}^{eq}$ of the two hydrogenation reaction were calculated for each Ga-substitutional system, and the second $P_{H_2}^{eq}$ at 350 K are shown in Fig. 4.6. as a function of volumes of dihydrides. These values of Ti-V-Mn

systems and VH_2 are also depicted in the figure for comparison.

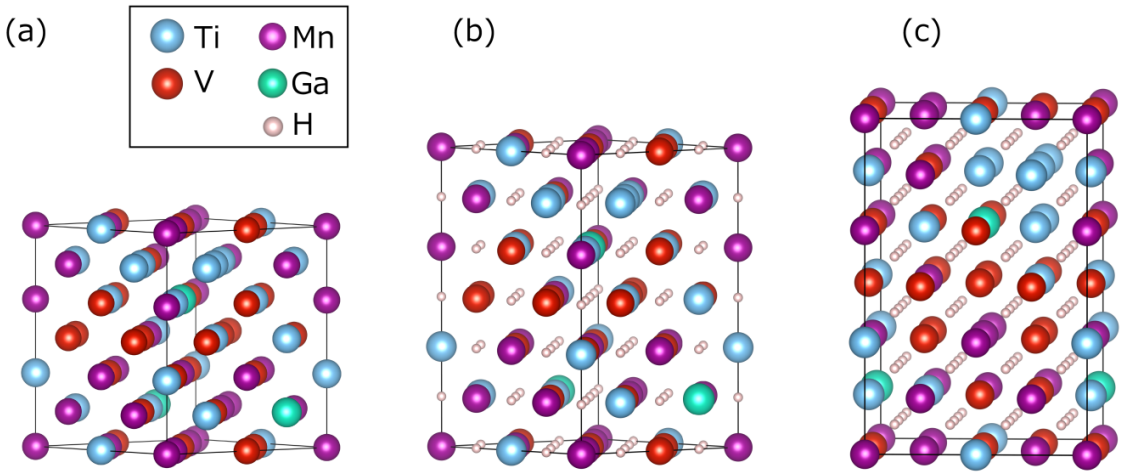

Fig. 4.5. Computational SQS models containing 48 metal atoms of (a) $Ti_{0.9}V_{1.1}Mn_{0.9}Ga_{0.1}$ alloy, (b) $Ti_{0.9}V_{1.1}Mn_{0.9}Ga_{0.1}H_3$, and (c) $Ti_{0.9}V_{1.1}Mn_{0.9}Ga_{0.1}H_6$.

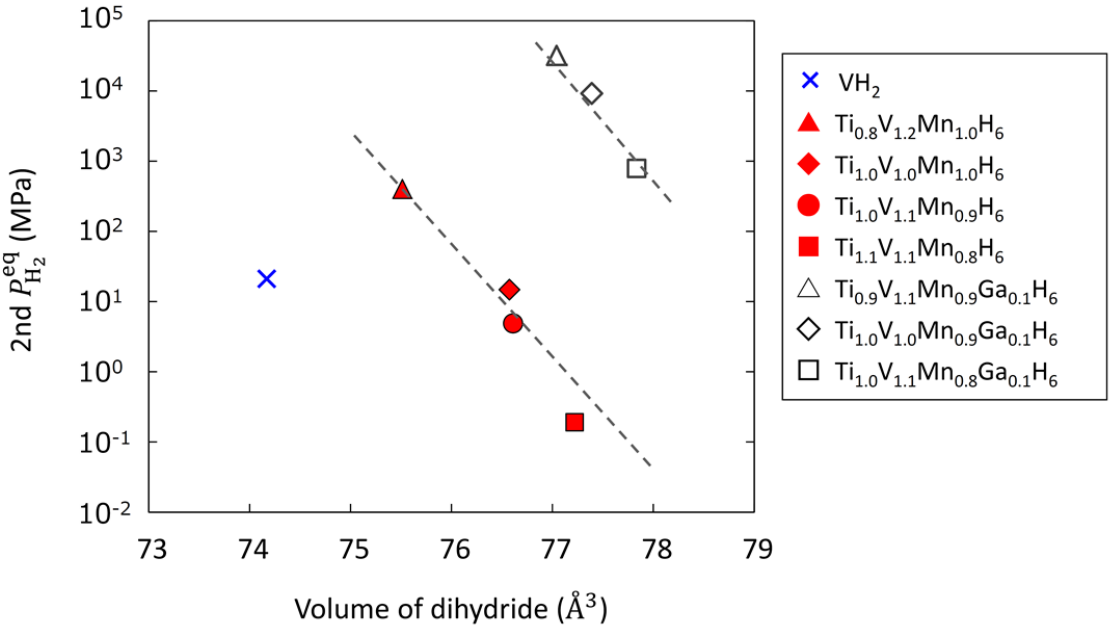

Fig. 4.6. Dependence of the second equilibrium hydrogen pressures, $P_{H_2}^{eq}$, at 350 K on volumes of dihydrides for V-H, Ti-V-Mn, and Ti-V-Mn-Ga systems.

In general, interstitial hydrogen storage alloys including Ti-V-based systems show linear relations between $P_{H_2}^{eq}$ and volumes of compounds, when H sites and structures are close in these compounds [3]. As seen in Fig. 4.6, the linear relations are observed in each set of Ti-V-Mn compounds denoted by red filled plots and Ti-V-Mn-Ga compounds denoted by open plots. The plot of VH_2 locates away from those two linear lines. This seems to originate from the different hydrogenation reaction of V, whose higher plateau reaction has still not clearly determined and lower plateau reaction is expressed as M-$MH_{0.5}$, not M-MH as in Ti-V-Mn systems. On the other hand, although we constructed Ti-V-Mn-Ga models having the same structures with $Ti_{1.0}V_{1.1}Mn_{0.9}$-H models and apparent structural changes did not observed before/after structural optimization process, the calculated second plateau pressures are higher than Ti-V-Mn-H systems by about four orders of magnitude. In spite of the amount of Ga in the compounds, $P_{H_2}^{eq}$ changed drastically by doping.

To investigate this discrepancy, we analyzed local structures in a cell of $Ti_{1.0}V_{1.1}Mn_{0.9}H_6$ and Ga-doped Ti-V-Mn dihydrides. We focused on the coordination of H atoms around metal atoms, and depicted the coordination numbers of H atoms around each metal atoms as a function of metal-hydrogen distance in Figure 4.7. Though the lower figure shows only the case of $Ti_{1.0}V_{1.1}Mn_{0.8}Ga_{0.1}H_6$, other Ga-doped systems show the same tendency. As seen in the figure, the first-nearest-neighbor distances of transition metals and hydrogen are not affected by the Ga-substitution. Among these elements, Mn makes the shortest bonding with H, then V and Ti in order. These bond lengths, however, are smaller compared with the first-nearest-neighbor distance of Ga and H, whose value is about 2.0 Å. The second-nearest-neighbor distances of each element are about 3.4 Å, and the difference of metal-hydrogen distances in transition metals and Ga is smaller than that of the first-nearest-neighbor. Therefore, it is suggested that the bonding state of Ga with hydrogen is different from those of transition metals, as supposed in the case of Al-doping.

Because the amount of Ga element is small in the compounds, most H atoms locate on T sites with almost the same distance from transition metal atoms, while H atoms around Ga are pushed away from the center of T sites. This introduces the local distortion around Ga atoms, and the Ga-doped Ti-V-Mn dihydrides are thought to be destabilized. As a result of these phenomena, $P_{H_2}^{eq}$ of Ti-V-Mn-Ga systems are suggested to increase apparently compared with $Ti_{1.0}V_{1.1}Mn_{0.9}$.

In summary, we calculated $P_{H_2}^{eq}$ of yet-synthesized Ga-doped Ti-V-Mn systems based on the assumption that the structures are the same with those of $Ti_{1.0}V_{1.1}Mn_{0.9}$-H system. Calculated $P_{H_2}^{eq}$ show drastic increases compared with Ti-V-Mn-H systems. These changes are thought to be caused by the different bonding mechanism with H atoms of Ga and transition metals.

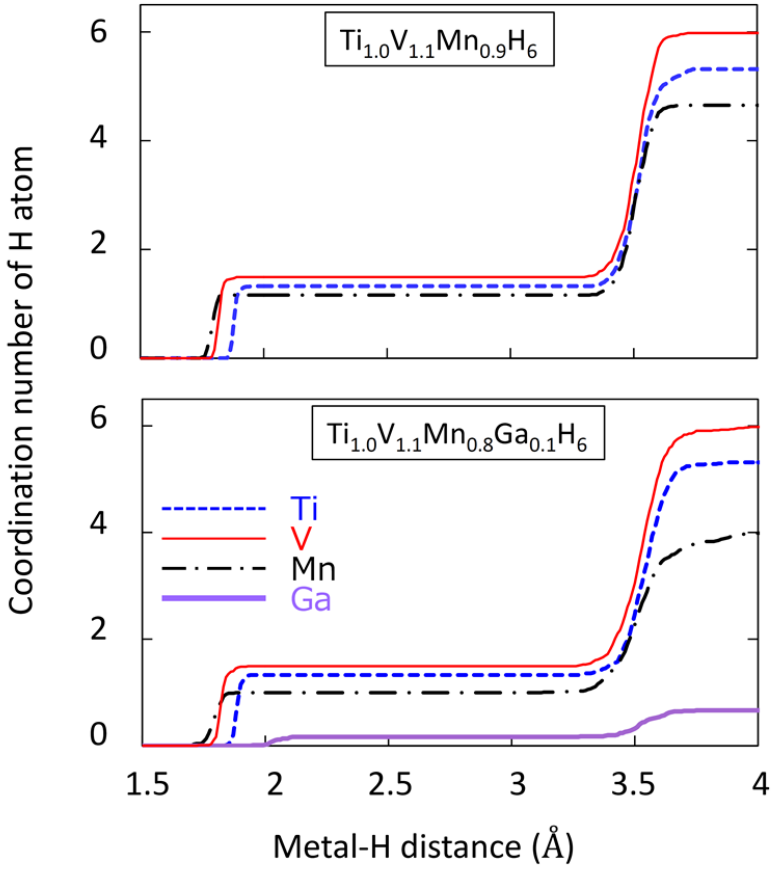

Fig. 4.7. Coordination numbers of H atom around each metal atom as a function of metal-hydrogen distance.

4.4. Conclusions

Based on the procedures introduced in Chapter 3, we evaluated $P_{H_2}^{eq}$ of Ti-V-Mn-H systems using first-principles calculations, mainly focusing on $Ti_{1.0}V_{1.1}Mn_{0.9}$ alloy. We used the crystal structures of hydrides obtained from experiments to generate computational models. Vibrational contributions were calculated for $Ti_{1.0}V_{1.1}Mn_{0.9}H_6$. E_{ZPE} of $Ti_{1.0}V_{1.1}Mn_{0.9}$ and $Ti_{1.0}V_{1.1}Mn_{0.9}H_3$ were represented by those of metal V and VH, based on the assumption that E_{ZPE} of Ti-V-Mn-H systems increase linearly, and the difference of E_{ZPE} values between V-H and Ti-V-Mn-H systems are small enough. Predicted $P_{H_2}^{eq}$ from theoretical calculations reproduce the tendencies of those obtained from experiments in the semi-quantitative way. As an extension, we calculated $P_{H_2}^{eq}$ of yet-synthesized Ga-doped Ti-V-Mn systems based on the assumption that the structures are the same with those of $Ti_{1.0}V_{1.1}Mn_{0.9}$-H system. Calculated $P_{H_2}^{eq}$ show drastic increases compared with Ti-V-Mn-H systems. These changes are thought to be caused by the different bonding mechanism with H atoms of Ga and transition metals.

Appendix C: Formulations of average pair correlation functions of disordered binary and disordered quaternary systems

The average pair correlation function of completely random models, $\overline{\Pi}^2$, can be expressed in analytical forms. For a ternary alloy A-B-C with compositions x_{A}, x_{B}, and x_{C}, $\overline{\Pi}^2$ is expressed as Eq. (5) in Sec. 4.2.2. In this appendix, $\overline{\Pi}^2$ of binary and quaternary systems are shown as a reference.

According to the formulation in Ref. [44], when the number of elements included in the system is *k*, $\overline{\Pi}^2$ can be expressed in the form

$$\overline{\Pi}^2[n,m] = \overline{\Pi}_n^1 \cdot \overline{\Pi}_m^1 , \tag{6}$$

where *n* and *m* take values of $1, 2, \ldots, k-1$. For example, there are four types of $\overline{\Pi}^2$ for a pair cluster in a ternary system (*k* = 3): $\overline{\Pi}^2[1,1]$, $\overline{\Pi}^2[1,2]$, $\overline{\Pi}^2[2,1]$, and $\overline{\Pi}^2[2,2]$. $\overline{\Pi}_n^1$ indicates the average point correlation function of a completely random model with index *n*. Because *n* takes integer values up to $k-1$, there are $k-1$ types of point correlation functions, e.g., one type in binary systems (*k* = 2), two types in ternary systems (*k* = 3), and three types in quaternary systems (*k* = 4). $\overline{\Pi}_n^1$ can be expressed by means of Chebyshev polynomials. We would not discuss details of mathematical derivation of $\overline{\Pi}_n^1$ here, but show the formulae of these correlation functions for reference. In the binary system $\mathrm{A}_{x_A}\mathrm{B}_{x_B}$, there is only one type of point correlation function expressed as

$$\overline{\Pi}_1^1 = x_{\mathrm{A}} - x_{\mathrm{B}}. \tag{7}$$

Therefore, $\overline{\Pi}^2$ can be written as

$$\overline{\Pi}^2[1,1] = (x_{\mathrm{A}} - x_{\mathrm{B}})^2. \tag{8}$$

In the case of the quaternary system A-B-C-D with compositions x_{A}, x_{B}, x_{C} and x_{D}, there are three types of $\overline{\Pi}_n^1$, namely

$$\overline{\Pi}_1^1 = \sqrt{\frac{2}{5}}\left(4x_A + 3x_B + x_C - 2\right), \tag{9}$$

$$\overline{\Pi}_2^1 = -2x_B - 2x_C + 1, \tag{10}$$

$$\overline{\Pi}_3^1 = \frac{-1}{3}\left(\frac{17}{\sqrt{10}}\left(4x_A + 3x_B + x_C - 2\right) + \sqrt{\frac{5}{2}}\left(16x_A + 9x_B + 7x_C - 8\right)\right). \tag{11}$$

As a result, totally nine types of $\overline{\Pi}^2$ are constructed from the combinations of Eq. (9) - (11).

References

[1] D. Mori, K. Hirose, Recent challenges of hydrogen storage technologies for fuel cell vehicles, Int. J. Hydrogen Energy 34 (2009) 4569–4574.

[2] D.K. Ross, Hydrogen storage: The major technological barrier to the development of hydrogen fuel cell cars, Vacuum 80 (2006) 1084–1089.

[3] Y. Fukai, The Metal-Hydrogen System, Springer-Verlag, Berlin/Heidelberg, 2005.

[4] H. Kim, K. Sakaki, H. Ogawa, Y. Nakamura, J. Nakamura, E. Akiba, A. Machida, T. Watanuki, T. Proffen, Origin of degradation in the reversible hydrogen storage capacity of $V_{1-x}Ti_x$ alloys from the atomic pair distribution function analysis, J. Phys. Chem. C 117 (2013) 26543–26550.

[5] T.B. Massalski, Binary Alloy Phase Diagrams, 2nd ed., ASM International, Ohio, 1990.

[6] R. Griffiths, J.A. Pryde, A. Righini-Brand, Phase diagram and thermodynamic data for the hydrogen/vanadium system, J. Chem. Soc., Faraday Trans. 1 68 (1972) 2344–2349.

[7] H. Yukawa, D. Yamashita, S. Ito, M. Morinaga, S. Yamaguchi, Alloying effects on the phase stability of hydrides formed in vanadium alloys, Mater. Trans. 43 (2002) 2757–2762.

[8] T. Hagi, Y. Sato, M. Yasuda, K. Tanaka, Structure and phase diagram of Ti–V–H system at room temperature, Trans. Jpn. Inst. Met. 28 (1987) 198–204.

[9] E. Akiba, H. Iba, Hydrogen absorption by Laves phase related BCC solid solution, Intermetallics 6 (1998) 461–470.

[10] S. Ono, K. Nomura, Y. Ikeda, The reaction of hydrogen with alloys of vanadium and titanium, J. Less-Common Met. 72 (1980) 159–165.

[11] H. Kim, K. Sakaki, I. Saita, H. Enoki, K. Noguchi, A. Machida, T. Watanuki, Y. Nakamura, Reduction and unusual recovery in the reversible hydrogen storage capacity of $V_{1-x}Ti_x$ during hydrogen cycling, Int. J. Hydrogen Energy 39 (2014) 10546–10551.

[12] J.F. Lynch, G.G. Libowitz, A.J. Maeland, Hysteresis in the Nb-V-H system, J. Less-Common Met. 103 (1984) 117–122.

[13] J.-H. Kim, H. Lee, P.S. Lee, C.-Y. Seo, J.-Y. Lee, A study on the improvement of the cyclic durability by Cr substitution in V–Ti alloy and surface modification by the ball-milling process, J. Alloys Compd. 348 (2003) 293–300.

[14] S.-W. Cho, C.-S. Han, C.-N. Park, E. Akiba, The hydrogen storage characteristics of Ti–Cr–V alloys, J. Alloys Compd. 288 (1999) 294–298.

[15] S.-W. Cho, C.-N. Park, J.-H. Yoo, J. Choi, J.-S. Park, C.-Y. Suh, G. Shim, Hydrogen absorption–desorption characteristics of $Ti_{(0.22+X)}Cr_{(0.28+1.5X)}V_{(0.5-2.5X)}$ ($0 \leq X \leq 0.12$) alloys, J. Alloys Compd. 403 (2005) 262–266.

[16] H. Iba, E. Akiba, Hydrogen absorption and modulated structure in Ti–V–Mn alloys, J. Alloys Compd. 253–254 (1997) 21–24.

[17] Y. Nakamura, E. Akiba, New hydride phase with a deformed FCC structure in the Ti–V–Mn solid solution–hydrogen system, J. Alloys Compd. 311 (2000) 317–321.

[18] Y. Nakamura, K. Oikawa, T. Kamiyama, E. Akiba, Crystal structure of two hydrides formed from a Ti–V–Mn BCC solid solution alloy studied by time-of-flight neutron powder diffraction — a NaCl structure and a CaF_2 structure, J. Alloys Compd. 316 (2001) 284–289.

[19] Y. Nakamura, E. Akiba, Hydriding properties and crystal structure of NaCl-type mono-hydrides formed from Ti–V–Mn BCC solid solutions, J. Alloys Compd. 345 (2002) 175–182.

[20] Y. Nakamura, J. Nakamura, K. Sakaki, K. Asano, E. Akiba, Hydrogenation properties of Ti–V–Mn alloys with a BCC structure containing high and low oxygen concentrations, J. Alloys Compd. 509 (2011) 1841–1847.

[21] S. Yamazaki, J. Nakamura, K. Sakaki, Y. Nakamura, E. Akiba, Phase transformation and lattice-strain formation in $Ti_{1.0}V_{1.1}Mn_{0.9}$ during first absorption and desorption, Mater. Trans. 52 (2011) 586–590.

[22] S.-W. Cho, E. Akiba, Y. Nakamura, H. Enoki, Hydrogen isotope effects in $Ti_{1.0}Mn_{0.9}V_{1.1}$ and $Ti_{1.0}Cr_{1.5}V_{1.7}$ alloys, J. Alloys Compd. 297 (2000) 253–260.

[23] S.-W. Cho, H. Enoki, T. Kabutomori, C.-N. Park, E. Akiba, Isotope effect on structural transitions of $Ti_{1.0}Mn_{0.9}V_{1.1}H_X(D_X)$ and $Ti_{1.0}Cr_{1.5}V_{1.7}H_X(D_X)$ with hydrogenation, J. Alloys Compd. 319 (2001) 196–203.

[24] J. Matsuda, Y. Nakamura, E. Akiba, Microstructure of Ti–V–Mn BCC alloys before and after hydrogen absorption–desorption, J. Alloys Compd. 509 (2011) 4352–4356.

[25] M.W. Chase Jr., NIST-JANAF Thermochemical Tables, 4th ed., The American Chemical Society and the American Institute of Physics for the National Institute of Standards and Technology, New York, 1998.

[26] P.E. Blöchl, Projector augmented-wave method, Phys. Rev. B 50 (1994) 17953–17979.

[27] G. Kresse, D. Joubert, From ultrasoft pseudopotentials to the projector augmented-wave method, Phys. Rev. B 59 (1999) 1758–1775.

[28] J.P. Perdew, K. Burke, M. Ernzerhof, Generalized gradient approximation ade simple, Phys. Rev. Lett. 77 (1996) 3865–3868.

[29] J.P. Perdew, J. Chevary, S. Vosko, K. Jackson, M. Pederson, D. Singh, C. Fiolhais, Erratum: Atoms, molecules, solids, and surfaces: Applications of the generalized gradient approximation for exchange and correlation, Phys. Rev. B 48 (1993) 4978–4978.

[30] G. Kresse, J. Hafner, Ab initio molecular dynamics for liquid metals, Phys. Rev. B 47 (1993) 558–561.

[31] G. Kresse, J. Furthmüller, Efficient iterative schemes for ab initio total-energy calculations using a plane-wave basis set, Phys. Rev. B 54 (1996) 11169–11186.

[32] H.J. Monkhorst, J.D. Pack, Special points for Brillouin-zone integrations, Phys. Rev. B 13 (1976) 5188–5192.

[33] A. Togo, I. Tanaka, First principles phonon calculations in materials science, Scripta Mater. 108 (2015) 1–5.

[34] A. Zunger, S.-H. Wei, L.G. Ferreira, J.E. Bernard, Special quasirandom structures, Phys. Rev. Lett. 65 (1990) 353–356.

[35] S.H. Wei, L.G. Ferreira, J.E. Bernard, A. Zunger, Electronic properties of random alloys: Special quasirandom structures, Phys. Rev. B 42 (1990) 9622–9649.

[36] A. Seko, Y. Koyama, I. Tanaka, Cluster expansion method for multicomponent systems based on optimal selection of structures for density-functional theory calculations, Phys. Rev. B 80 (2009) 165122.

[37] K. Asano, S. Hayashi, Y. Nakamura, Enhancement of hydrogen diffusion in the body-centered tetragonal monohydride phase of the V–H system by substitutional Al studied by proton nuclear magnetic resonance, Acta Mater. 83 (2015) 479–487.

[38] T. Kajitani, M. Hirabayashi, Neutron diffraction study of β_1-V_2H and β-V_2D, Z. Phys. Chem. NF 145 (1985) 27–42.

[39] K. Kamazawa, M. Aoki, T. Noritake, K. Miwa, J. Sugiyama, S. Towata, M. Ishikiriyama, S.K. Callear, M.O. Jones, W.I.F. David, In-operando neutron diffraction studies of transition metal hydrogen storage materials, Adv. Energy Mater. 3 (2013) 39–42.

[40] K. Miwa, A. Fukumoto, First-principles study on 3d transition-metal dihydrides, Phys. Rev. B 65 (2002) 155114.

[41] A. Kagawa, E. Ono, T. Kusakabe, Y. Sakamoto, Absorption of hydrogen by vanadium-rich V-Ti-based alloys, J. Less-Common Met. 172–174 (1991) 64–70.

[42] J. Yoo, G. Shim, J. Yoon, S. Cho, Effects of substituting Al for Cr in the $Ti_{0.32}Cr_{0.43}V_{0.25}$ alloy on its microstructure and hydrogen storage properties, Int. J. Hydrogen Energy 34 (2009) 1463–1467.

[43] J. Hangjun, Z. Jinlong, M. Xianghai, L. Genwen, G. Jianshen, Hydrogen storage properties and structure of $TiV_{0.8-x}Cr_{1.2}Al_x$ alloys, Rare Met. Mater. Eng. 37 (2008) 803–807.

[44] D. De Fontaine, Cluster approach to order-disorder transformations in alloys, Solid State Phys. 47 (1994) 33–176.

Chapter 5

General Conclusion

In this study, we implemented first-principles calculations to investigate properties of Ti-V-based hydrogen storage materials.

In Chapter 2, solid solution states of Ti-V dihydrides have been investigated using first-principles calculations and the cluster expansion method in order to clarify effects on hydrogen storage capacities. It is found that the dihydrides form stable solution with 9 ground-state structures identified from 154,156 candidate structures using 46 clusters with up to five atoms interactions. Most of the ground states have layered structures containing V bilayers, which are not known experimentally. Analysis of the effect of clusters on ground-state stability suggests that, while pair clusters contribute to the preference for layered structure formation, the higher-body clusters stabilize V bilayers over Ti bilayers. Those layered structures are found to have phase-separation tendency from analysis of short-range order parameters. It seems that disordered solutions will be formed under typical synthesis conditions from order-disorder transition temperatures of ordered ground-state structures, which are estimated from MC simulations to be less than 460 K, and comparison of lattice parameters with experimental values. The examination of the bonding energies of H atoms indicates that the bonding strength of hydrogen in Ti-V dihydrides is not greatly affected by the metal-atom ordering. Our results give an indication that trapping of stored hydrogen atoms hardly occur in grain interior of the dihydrides.

In Chapter 3, Equilibrium hydrogen pressures, $P_{\mathrm{H_2}}^{\mathrm{eq}}$, in the V-H system were estimated using first-principles calculations by first searching for low-energy structures among candidate configurations of intermediate hydrides $VH_{0.5}$ and VH excluding vibrational contributions. The

lowest-energy configurations were found to have H atoms distributed over T_z sites for both H contents. When vibrational contributions were included, the ground-state configurations were bct-like structures with hydrogen atoms on O_z sites. Zero-point energy, ZPE, has a particularly strong effect on the ground-state configuration. Theoretical $P_{H_2}^{eq}$ values calculated using these models reproduce experimental values well, although the results for high H contents suggest a mixture of O and T sites are occupied. Our results demonstrate how equilibrium hydrogen pressures of V-based compounds can be estimated from DFT calculations by combining configurational searches with inclusion of lattice vibrations, which should provide useful insights into how to optimize the hydrogenation behavior of V-based compounds.

In Chapter 4, $P_{H_2}^{eq}$ in the Ti-V-Mn-based alloys were estimated as an extension of procedures introduced in Chapter 3. In this study, we mainly focused on $Ti_{1.0}V_{1.1}Mn_{0.9}$ hydrides, whose metal sublattice and H sites are determined from experimental measurements. Because the difference of zero-point energies between $Ti_{1.0}V_{1.1}Mn_{0.9}H_6$ and VH_2 is small, contributions of vibrational effects on the Ti-V-Mn-H system are considered to be the same as those of the V-H system. Predicted $P_{H_2}^{eq}$ reproduce the tendencies of experiments. Moreover, we examined $P_{H_2}^{eq}$ in the Ga-doped Ti-V-Mn alloys in order to evaluate the effects of doping non-transition metals. The values of $P_{H_2}^{eq}$ changes considerably by Ga-doping, which seems to be originated from the longer distance of Ga-H bonding compared to transition-metal-hydrogen bonding.

This study reveals that first-principles calculations are of help in the estimation of $P_{H_2}^{eq}$ or structural determination of Ti-V-based alloys and hydrides. The methodologies employed in this study, however, are not limited to this kind of compounds. It would contribute to the investigations on searching adequate compositions of hydrogen storage materials for practical applications. Moreover, the atomic-scale structures such as H sites or local distributions of metal atoms, which

are difficult to measure by experimental methods, are estimated by means of first-principles calculations. We believe that this study helps to illuminate the essential properties of Ti-V-based compounds, and to develop the practical hydrogen storage materials utilized in the hydrogen economy.

Acknowledgement

The author would like to express her deepest gratitude to the supervisor, Professor Isao Tanaka at Kyoto University for constant guidance, extensive discussions and encouragement through this study. The author also would like to express her gratitude to Associate Professor Atsuto Seko at Kyoto University for detailed advice on the cluster expansion method, and useful discussions and comments.

The author would like to express her gratitude to Doctor Akihide Kuwabara and Doctor Takafumi Ogawa of Japan Fine Ceramics Center for guidance on first-principles calculations and valuable discussions through this work. Special thanks to Doctor C. A. J. Fisher for useful advice on molecular dynamics simulations, Doctor Kazuki Shitara for advice on the cluster expansion method and machine-learning techniques, and Doctor Hiroki Moriwake and Ms. Akiko Konishi for valuable comments. The author would also like to express her gratitude to Professor Etsuo Akiba at Kyushu University for practical advice on the properties of hydrogen storage materials.

The author would like to offer her special thanks to the members of Nanostructures Research Laboratory at Japan Fine Ceramics Center, and staffs and colleagues of Professor Isao Tanaka's Laboratory at Kyoto University for constructive discussion and long-term support.

Finally, the author wants to express her gratitude to her family for their endurance, support and encouragement.

Noriko Otani

2017